Behavior and functional imaging of zebrafish larvae

R. Candelier

Université Pierre et Marie Curie

HABILITATION À DIRIGER LES RECHERCHES
-
HABILITATION FOR RESEARCH SUPERVISION

Raphaël CANDELIER

Behavior and functional imaging of zebrafish larvae

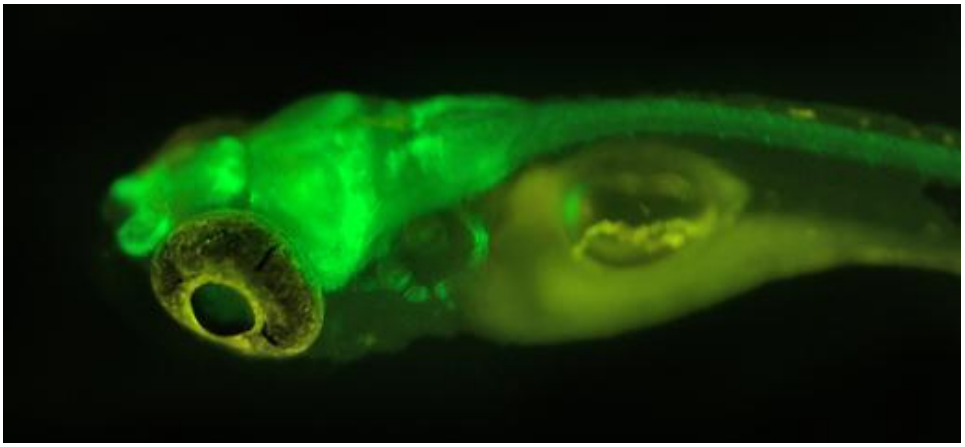

Laboratoire Jean Perrin - UMR 8237

Résumé

Mon activité au sein du Laboratoire Jean Perrin est centrée autour du développement de nouvelles techniques expérimentales autour de la larve de poisson zèbre. C'est un système modèle dont les propriétés de transparence et la taille réduite du cerveau à l'état larvaire (environ 10^5 neurones) en font un système parfaitement adapté à l'imagerie calcique en général, et en particulier à la microscopie par nappe de lumière, ou *Single Plane Illumination Microscopy* (SPIM). Pendant ces quelques années d'intense travail collectif, nous avons développé des dispositifs pour étudier le comportement et l'activité neuronale. Nous avons démontré dès 2013 qu'il est possible d'enregistrer simultanément et sans limite de temps l'activité de plus de 25 000 neurones répartis dans plusieures aires cérébrales à une vitesse d'acquisition de 4Hz, ce qui représente un gain d'un facteur 30 par rapport aux microscopes point-à-point. La technique SPIM permet aussi d'avoir un meilleur rapport signal sur bruit et élimine quasi-totalement le photoblanchiement et la phototoxicité. Nous avons par la suite développé un SPIM avec illumination infrarouge, se basant sur l'effet à deux photons. Afin de répondre à des problématiques de neuroscience nous diversifions aussi nos activités de recherche, et nous avons mené des études de comportement en nage libre et en réalité virtuelle.

Abstract

My research activities at the *Laboratoire Jean Perrin* have been centered around the development of new experimental techniques for studying the larval zebrafish brain. This small animal is a model system, whose transparency and brain size (approx. 10^5 neurons) properties make it perfectly well-suited for calcium imaging in general and Single Plane Illumination Microscopy (SPIM) in particular. During the last few years of intense collective work, we have developped in the lab many setups to explore the behavior and neural mechanisms at play in this tiny vertebrate. We have demonstrated in 2013 that it is possible to record simultaneously and without time limit some 25,000 neurons at 4 Hz, which represents an approximately 30-fold gain with respect to classical point-scanning microscopes. The SPIM technique also improves the signal to noise ratio and greatly mitigates photobleaching and photo-toxicity. We have then developed a SPIM setup with infrared illumination and using 2-photon fluorescence. In order to answer general questions of neuroscience we diversify our research activities, and we have led behavioral studies on free-swimming animals or in a virtual reality setup.

Contents

Chapter 1

Introduction

Contents

Research track

Since my first steps in a lab in 2003, my research work have followed two thematic foci. The first one is about the statistical physics of condensed matter, as during my Ph.D. I have worked on dense packings of grains (experiments) and particles in soft interactions (simulations). More specifically, I have studied their dynamics and structure close to the Glass and Jamming transitions [1]. The second – *a priori* unrelated – thematic focus is about perception: I spent 6 months at the Inteligent Mechanism Lab in Doshisha University (Kyoto) to study the precedence effect on virtual tones in humans (psychoacoustics) and 6 months at the *Département d'Étude Cognitives* of the *École Normale Supérieure* (ENS - Paris) to study the perception of subliminal words by humans (psycholinguistics). I have then worked for a year in the team of Giorgio Parisi (Rome) as a member of the STARFLAG European project on the perception of mates in collective behaviors of starlings. Then, as a point of convergence I have worked at the *Laboratoire Jean Perrin* (LJP) on mecano-transduction of tactile perception during a two-year post-doc.

My more recent work and short-term research projects are about the neural coding of sensory perception in a model vertebrate, zebrafish larvae. In continuation with my previous studies, this work is experimentally in between physics and biology and requires for the analyses several tools that

I have learnt to manipulate when I was working in statistical physics.

For the purpose of brevity, and coherently with the scientific orientation I chose for the rest of my career, this manuscript will only cover the research topics related to zebrafish larvae. Note also that I will use the plural "we" instead of "I" in the sequel, as most of what is presented here is the work of many people including Georges Debrégeas (Research Director), with whom we started this activity at the LJP in 2011, Volker Bormuth (Assistant Professor) who joined us in 2014, Carounagarane Doré (Mecanician) and many contributing students and postdoc, especially Thomas Panier, Raphäel Olive and Sébastien Wolf.

Organization of the manuscript

In the rest of the introduction I will present briefly the model system – zebrafish larvae – and the momentum it has recently gained in the functional imaging community.

Then I will present in three chapters the different experimental approaches we have developped. There is a certain logic to start by presenting the behavioral studies since they are closer to "natural conditions" for the animal and limit some important experimental biases (immobility, illumination, etc.). Then I will present the technical developments we have done in functional light sheet microscopy and finally the main results we have obtained.

Scientific context: calcium imaging and zebrafish

One of the most exciting scientific challenge of our times is to understand how cognitive functions emerge from the collective dynamics of the massive amount of neurons in interaction in the vertebrate brain. More precisely, the functional ensembles range from micro-networks including only a few neurons to large-scale networks encompassing millions of neurons located in distinct cerebral areas. This intrinsically multi-scale organization of the brain poses many challenges both conceptually and experimentally, calling for new approaches.

As an exemple, the zebrafish brain comprises approximately 10^5 neurons at the larval stage [2], 10^7 for the adults [3] and, by analogy with other species, one can estimate that there are between 100 and 10 000 times more synaptic connections. From an experimental point of view, until recently the recordings with single-cell resolution were limited to rather small neural

populations, often located in a single cerebral area. This sparse sampling gave only very few information on the large-scale organization of the brain. The development of calcium imaging has radically changed this perspective: it is henceforth possible to follow the activity of large neural populations by monitoring the fluctuations of calcium probes whose fluorescence is coupled to the amount of action potentials. However, when applied to the mammal brain the functional calcium imaging stays confined to the most superficial layers of the brain (typically 500 microns) due to light scattering.

This limitation explains for a large part why zebrafish has gained a growing popularity in neuroscience. This vertebrate indeed offers a unique combination of transparency, relatively reduce brain dimensions and genetical modification amenability and the larva's brain can be now used in brain-wide *in vivo* functional imaging with genetically encoded calcium reporters [4, 5].

Comparatively to fMRI (that allows for brain-wide recordings but with poor spatial and temporal resolutions) and electrophysiology (that captures the full action potential dynamics but only on a very limited number of neurons, which are often difficult to select), the calcium imaging technique is a good compromise. It offers cellular resolution over large volumes and has a temporal resolution that keeps on getting better and better with the development of calcium probes and microscopy setups.

Since 2012, non-simultaneous brain-wide recordings have systematically mapped neural population which activity correlates with some visual stimuli or with the animal's motor activity [6, 7, 8]. However, this approach offers only few information of the dynamical processes at play during sensori-motor integration: the transition from this topological description to the network's effective connectivity requires a supplementary effort. In other words, instead of looking at the activity/responses of many neurons independently, there is a real gain to analyse the inter-neurons correlations as it reflects their synaptic connections.

This latter approach requires simultaneous brain-wide recordings. Light sheet microscopy – elected "method of the year" in 2014 by Nature Methods – allows for the fast imaging of relativelty transparent samples. In 2013, a group in Janelia Farm [2] and the Laboratoire Jean Perrin [9] have independently demonstrated that light sheet microscopy or SPIM (Single-Plane Illumination Microscopy) could provide simultaneous recordings of large portions of the larval zebrafish brain at a few Hertz, yet with quasi-cellular resolution. I do believe that this technique has a whopping potential in neuroscience, as it offers the unique opportunity to study the functional organization of a vertebrate brain at all scales.

Chapter 2

Behavior

Contents

Rheotaxis in radial flow geometry

Raphaël Olive has been my first Ph.D. sudent, and he worked on mechanoreception in larval zebrafish [10]. The first part of his thesis reports results of a *rheotaxis* experiment, a term describing the spontaneous behavior shared by all aquatic species to align in a flow and swim counterflow to stabilize their position in the terrestrian reference frame. We have developed a simple setup in which the motion of free-swimming larvae was recorded by a camera while a radial aspiration flow was imposed. After processing the images, more than 4,000 trajectories containing approximately 18,000 counterflow swim bouts have been extracted and characterized.

A priori, the sensory modalities at play here are vision, acceleration perception *via* the inner ear and flow perception mediated by the lateral line. By suppressing visual inputs (plunging the animals in darkness) and/or lateral line inputs (chemical ablation of the neuromasts), we could compare the relative contributions of each sensory modality. It appeared first that when both vision and the lateral line are suppressed the animals are passively driven to the succion point, suggesting that the sole vestibular system cannot trigger an escape move. Then, we could determine a dominant modality for the different behavioral phases: the initiation of the counterflow sequence, marking the transition with free-swim, is dominated by the lateral line while the bouts during the counterflow swim phase are dominated by the visual

system. The fact that a sensory modality supplants the other rules out any information sharing mecanism neither in the decision making nor in the regulation of the counterflow swim. We don't know if sensory inputs are indeed merged in older animals, but in the framework of this experiment we couldn't test for integrative models like Bayesian inference (see [11] for a review).

This experiment has also led to some non-trivial results:

— First, we observed that passive reorientation – the fact that any elongated object in a flow has a tendency to align slowly towards current lines – is completetly abolished in both the free-swim and counterflow phases, suggesting that there is always an active process of orientation control. During free swim the larvae search for diversifying their orientations with random and frequent turns, while during the counterflow sequence they lock on the local flow direction. Our recordings couldn't state if, during the free-swim phase, the larvae reorient more often with or without the flow. This aspect would probably desserve new experiments with long recordings of the free-swim phase.

— Then, we have shown that the first swim event occurs at a constant average radial position, independantly of the flow rate and for all sensory condditions. As all instantaneous kinetic quantities vary with the flow rate (if q is the volumic flow rate, speed scales in q/r, acceleration in q/r^3, etc.), so none can explain the counterswim sequence initiation. We thus propose that these sequences are triggered by temporal integration of some kind, but our data couldn't lead to more on this.

— By analyzing in detail the swim patterns we have observed some differences between the sensorimotor control relying on the visual system only or by the lateral line only. For the lateral line, an attraction/repulsion process around an operating point (physically a circle arc ≈9 mm around the succion point) whereas for the visual system we observed repulsion close to the succion point (below 5 mm) and an immediate efficient compensation at any further distance.

— Finally, by comparing the larvaes at different ages we observed that, despite the average distance between two successive swim bouts stays at zero (indicating that the animal performs the rheotaxic task) the average number of tail beats decreases from 5 to 9 dpf. this is directly compensated by an increase in the average bending when the visual system is active, and by a diminution of the period between two successive swim bouts when the sole lateral line is active.

These results call for new experiments at the neural level. Our initial project was to reproduce this experiment in a partially tethered animal while recording the evoked neural activity. Despite many attempts (that actually took one year of Ph.D. to Raphaël Olive), we couldn't obtain recordings showing neural activity correlated with the flow stimuli. We hypo-

thesized that either *i*) the vestibular systems acts as a "global switch" that remains off when the animal is immobile, or that *ii*) the HuC:GCaMP5 and HuC:GCaMP6f strains used for these studies do not express fluorescence in the lateral line ganglions, though the promoter is *a priori* pan-neuronal.

frontiers in Systems Neuroscience

ORIGINAL RESEARCH
published: 23 February 2016
doi: 10.3389/fnsys.2016.00014

Rheotaxis of Larval Zebrafish: Behavioral Study of a Multi-Sensory Process

*Raphaël Olive, Sébastien Wolf, Alexis Dubreuil, Volker Bormuth, Georges Debrégeas and Raphaël Candelier**

Laboratoire Jean Perrin, Université Pierre et Marie Curie, Sorbonne Universités, Centre National de la Recherche Scientifique 8237, Paris, France

Awake animals unceasingly perceive sensory inputs with great variability of nature and intensity, and understanding how the nervous system manages this continuous flow of diverse information to get a coherent representation of the environment is arguably a central question in systems neuroscience. Rheotaxis, the ability shared by most aquatic species to orient toward a current and swim to hold position, is an innate and robust multi-sensory behavior that is known to involve the lateral line and visual systems. To facilitate the neuroethological study of rheotaxic behavior in larval zebrafish we developed an assay for freely swimming larvae that allows for high experimental throughtput, large statistic and a fine description of the behavior. We show that there exist a clear transition from exploration to counterflow swim, and by changing the sensory modalities accessible to the fishes (visual only, lateral line only or both) and comparing the swim patterns at different ages we were able to detect and characterize two different mechanisms for position holding, one mediated by the lateral line and one mediated by the visual system. We also found that when both sensory modalities are accessible the visual system overshadows the lateral line, suggesting that at the larval stage the sensory inputs are not merged to finely tune the behavior but that redundant information pathways may be used as functional fallbacks.

Keywords: zebrafish, rheotaxis, behavior, vision, lateral line, multi-sensory integration

OPEN ACCESS

Edited by:
Mikhail Lebedev, Duke University, USA

Reviewed by:
Hernan Lopez-Schier, Helmholtz Zentrum Munchen, Germany
Logan Ganzen, Purdue University, USA

****Correspondence:***
Raphaël Candelier
raphael.candelier@upmc.fr

Received: *24 December 2015*
Accepted: *08 February 2016*
Published: *23 February 2016*

Citation:
Olive R, Wolf S, Dubreuil A, Bormuth V, Debrégeas G and Candelier R (2016) Rheotaxis of Larval Zebrafish: Behavioral Study of a Multi-Sensory Process. Front. Syst. Neurosci. 10:14. doi: 10.3389/fnsys.2016.00014

1. INTRODUCTION

Positive rheotaxis is the innate behavior shared by most fishes and amphibians to turn to face into an oncoming current, and hold position with minimum expenditure of energy (Arnold and Weihs, 1977). Its widespread nature and the fact that it imposes to manage many sensory cues of different nature (visual, vestibular, hydromechanical, proprioceptive) that are available to the animal makes the generic neuronal processes at play of great interest from a fundamental perspective.

The term *rheotaxis* actually encompasses two distinct behavioral phases, namely orientation of the body along stream lines and counterflow swim to hold position. Position holding is often considered to rely on the sole visual system and in particular on the so-called optomotor reflex (Orger et al., 2000, 2008; Portugues and Engert, 2009). Regarding body orientation, it has been considered for a long time that it could not originate from hydromechanical cues based on the false assumption that when a fish is carried away in a stream there is no relative motion between the fish and its surrounding medium (Lyon, 1904; Arnold, 1974). In real situations there are always

velocity gradients created by walls, obstacles, sheared flows, or turbulence which can be captured by the lateral line, and it has been shown that superficial neuromasts mediate the body reorientation behavior (Montgomery et al., 1997) even in the absence of visual cues (Baker and Montgomery, 1999). Most subsequent studies then considered that the lateral line is the dominant sensory system in controlling body orientation (Chagnaud et al., 2007; Olszewski et al., 2012; Suli et al., 2012).

This categorization—the lateral line mediates body orientation and the optomotor response mediates counterflow swim—is however too simplistic to explain the rich behavior of aquatic species. For instance there are evidences that visual (Suli et al., 2012) or olfactory (Baker and Montgomery, 1999) cues help fishes to orient themselves and that some fishes deprived of both visual and hydomechanical cues can still perform rheotaxis (Van Trump and McHenry, 2013), supposedly by means of tactile perception. The whole rheotaxis process should thus be regarded as a multisensory task (Bak-Coleman and Coombs, 2014) and it remains to elucidate, for an animal that is able to perform body orientation and position holding when deprived of any of the lateral line or the visual system, what are the relative contributions of each sensory input during each of the two rheotaxic phases. For each phase, two main hypotheses can be drawn up: (i) there is a dominant modality that inhibits the inputs from the other modality or (ii) there is a weighted integration of both inputs, such as Bayesian inference (Pouget et al., 2013) for instance, that would result in a intermediary behavior.

Here, we investigate the rheotaxic behavior of freely-swimming larval zebrafish in a radial flow assay. This vertebrate model presents a number of advantages for studying the neural basis of behavior (Portugues and Engert, 2009) and, in particular, its translucency and genetic tractability allow for non-invasive imaging of brain-wide neural activity (Orger et al., 2008; Ahrens et al., 2013; Panier et al., 2013). We tracked thousands of larvae in different sensory conditions (with or without light, with or without hydomechanical cues) and categorized the discrete bouts in sequences of exploration swim and counterflow swim. The counterflow swim sequences (CSS) showed clear position holding, both angularly and radially, when visual or hydromechanical cues could be exploited. We observed that the position holding mechanism is different when the larva has only access to visual or hydromechanical cues and that, except for the CSS initiation where the lateral line system allows for earlier triggering, the visual system is the dominant modality in shaping the swimming patterns during CSS.

2. RESULTS

2.1. Rheotaxis Assay

To study rheotaxis in freely swimming larval zebrafish we used the radial flow geometry proposed in Olszewski et al. (2012) in an assay allowing for high experimental throughtput. Clutches of tenths of wild-type larvae from 5 to 9 days post fertilization (dpf) were placed in the assay and series of aspiration from a suction point followed by water reinjection were applied (**Figures 1A,B**). Among the dozens of larvae present in the device, only the few lying in the field of view at the center of the assay were imaged during the suction phase by a high speed camera at 250 Hz. Flow rates ranging over a decade were applied with a cycle-to-cycle randomization. The reinjection flow randomly reset the positions of the larvae in the assay at each cycle, ensuring a renewal of the population lying in the field of view. We used an *a posteriori* image processing method to automatically track the larvae, extract body curvatures, and define swim bouts with great accuracy (see Materials and Methods, **Figure 1C** and Supplementary Video 1). The notation of quantities relative to swim bouts are introduced in **Figures 1D,E**.

The larvae showed robust positive rheotaxis, i.e., alignment toward the flow and counterflow swimming in the form of sequences of bouts (**Figure 2A**). With 52 clutches submitted to 90 cycles each, we recorded 4082 trajectories (i.e., $N \approx 4000$ larvae) and identified 2409 CSS comprising a total of 17,964 swim bouts. All trajectories that lasted more than 10 s showed a CSS. In order to tune the sensory information available to the larvae, half of them were chemically treated with $CuSO_4$ to inactivate the lateral line (see Materials and Methods) and, independently, half the experiments were performed in the dark, thus leading to four different sensory conditions.

2.2. Transition from Exploration to Counterflow Swim

In the absence of visual and hydrodynamic cues, the larvae passively drifted toward the suction point (**Figure 2B** and Supplementary Video 2). We sometimes observed brusque, oversized, and non-oriented escape bouts (see Supplementary Video 2), indicating that the remaining sensory systems (tactile, proprioceptive, and vestibular systems for instance) can trigger escape responses but are unable to generate CSS behavior on their own. All sensory conditions involving either the lateral line or the visual system showed CSS (**Figure 2B** and Supplementary Videos 3–5).

As the angle α between the body axis and the local stream lines determines the efficiency of each impulse to compensate the flow, it is a key parameter of counterflow swim. We observed a clear transition from initial exploration behavior for which α is uniformly distributed to CSS with peaked distribution of α (**Figure 3A**). Aligment along the stream lines can be achieved either actively during swim bouts, or simply passively because of the *Jeffery effect*: hydrodynamic computations show that elongated objects in sheared flows experience torque (Jeffery, 1922; Dhont and Briels, 2005) which, in our geometry, tends to align the larvae radially on a time scale that depends on the flow rate and the initial position (radius and angle) of the larva. We computed the circular variance of α in time bins of 0.5 s ranging from 10 s before to 10 s after the onset of the CSS (**Figure 3B**), and compared it with the circular variance of simulated passive trajectories (see Materials and Methods). During the exploration phase the circular variance was close to 1, the theoretical value for a uniform angular distribution. Notably, the circular variance did not decreased with time, suggesting that the larvae actively explored their angular space

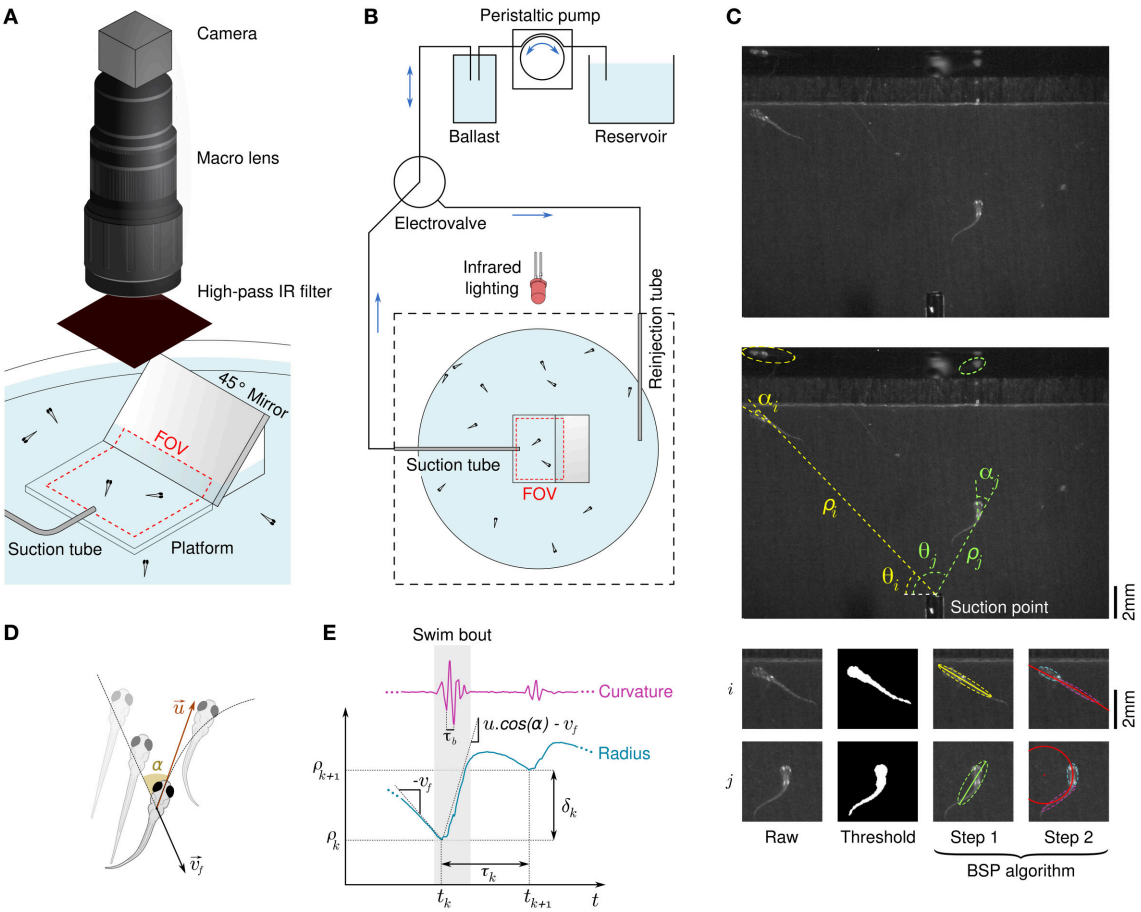

FIGURE 1 | Behavioral response of freely swimming zebrafish larvae to a radial flow. (A) Schematic diagram of the rheotaxis assay. Zebrafish larvae are spread all across the pool and a thin tube creates a radial flow by aspiration. The field of view (FOV) is a rectangle in the center of the assay which comprises a platform that locally raises the ground and the bottom part of a 45° mirror. An infrared-sensitive camera continuously images the FOV at a framerate of 250 Hz. **(B)** Schematic view of the flow control system. The suction tube is connected to a ballast, a peristaltic pump, and a reservoir. A computer-driven electrovalve allows to reinject water orthoradially to periodically randomize the larvae positions. **(C)** Illustration of the image processing algorithm. Raw grayscale images (top) are substracted to a background image and thresholded to materialize binarized larvae bodies (bottom left), from which polar coordinates $[\rho(t), \theta(t)]$ are derived (center). A BSP tree (bottom-right) is used to obtain the equivalent ellipses of the head and tail and define the body angle (head angle) $\alpha(t)$ and body curvature $\kappa(t)$. **(D)** Scheme defining the fluid velocity $\vec{v}_f$ and the bout impulse speed $\vec{u}$. **(E)** Swim bouts are located on the basis of the curvature's trace. For each swim bout k we define the radius ρ_k where the bout started and the inter-bout delay / distance, respectively $\tau_k = t_{k+1} - t_k$ and $\delta_k = \rho_{k+1} - \rho_k$.

at a pace that is sufficient to neutralize the effect of passive orientation (Supplementary Videos 6, 7). During the CSS the circular variance immediatly dropped to an asymptotical value close to 0, the theoretical value for perfect alignment. Quasi-radial orientation was achieved in one single bout for the three sensory conditions. For all later bouts, the distributions of body angles at the bout onset were slightly more peaked than at the bout offset, most likely due to the passive orientation occuring during inter-bout delays (**Figure 3C**).

2.3. Initiation and Regulation of Counterflow Swimming Sequences

To evaluate which hydomechanical cues are determinant in the initiation of CSS in larval zebrafish, we compared the average radial position ρ_1 and average velocity v_1 at the onset of CSS as functions of the suction flow rate (**Figure 4A**). For all sensory condition, the radial position was found to be independent of the flow rate, the velocity had a linear dependence and the acceleration a parabolic dependence (not shown). We checked that the distributions of ρ_1 are different from random positions in the field of view (two-sample Kolmogorov-Smirnov test, $p < 10^{-10}$ in all three sensory conditions), while the distributions of angular positions θ_1 could not be significantly differentiated from uniform randomness (two-sample Kolmogorov-Smirnov test, $p > 10^{-3}$ in all three sensory conditions). Notably, the average ρ_1 were significatively lower when the fish relied on its sole visual system than when it could use its lateral line (Welch's t-test, $p > 0.9$ for lateral line only compared to both sensory input, $p < 10^{-10}$ otherwise) and, coherently, the average v_1 were higher. In our paradigm where the fish is driven toward the suction point it means that the lateral line allows for an earlier initiation of the CSS behavior than the visual system. With both sensory modalities, the radii at which CSS initiates are undistinguishable from those of the lateral line only condition,

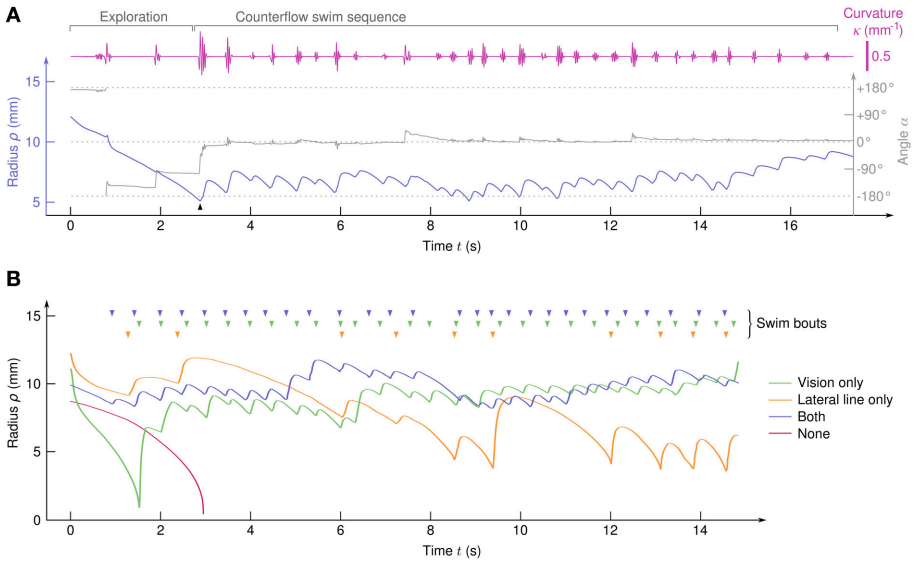

FIGURE 2 | Typical trajectories. (A) Traces of $\rho(t)$, $\alpha(t)$, and $\kappa(t)$ for a sample trajectory of a larva with both the visual system and the lateral line. A counterflow swim sequence of 31 bouts starts at $t \simeq 3s$ (arrow). **(B)** Typical trajectories of four larvae in the different sensory conditions. (top) Arrowheads indicate the swim bouts.

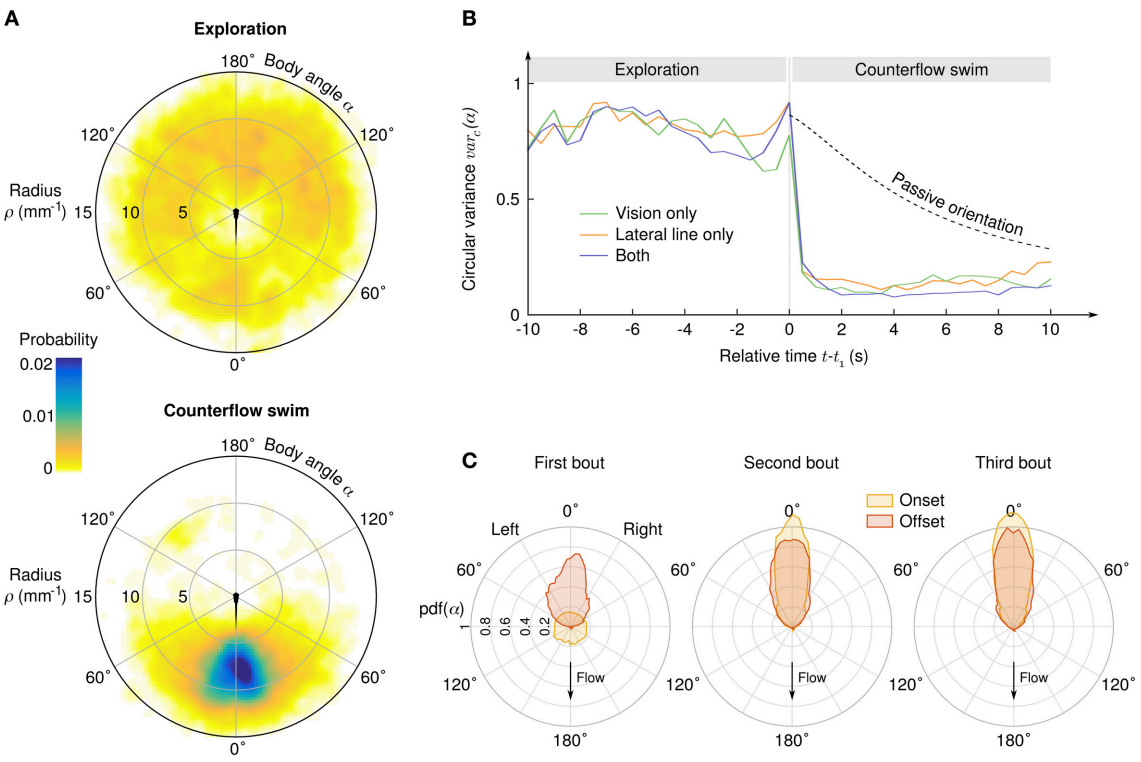

FIGURE 3 | Transition from exploration to counterflow swim. (A) Probability density of the suction point's location in the reference frame of the larva, before (top) and during (bottom) the counterflow swim sequence. **(B)** Circular variance of α as a function of the time relative to the first bout of the CSS, for three different sensory conditions. The "passive orientation" curve has been obtained numerically by computing the circular variance of putative trajectories of inert larvae with the same initial conditions (position and body angle). **(C)** Distributions of the body angle α at the onset (yellow) and offset (red) of the first three bouts of the CSS.

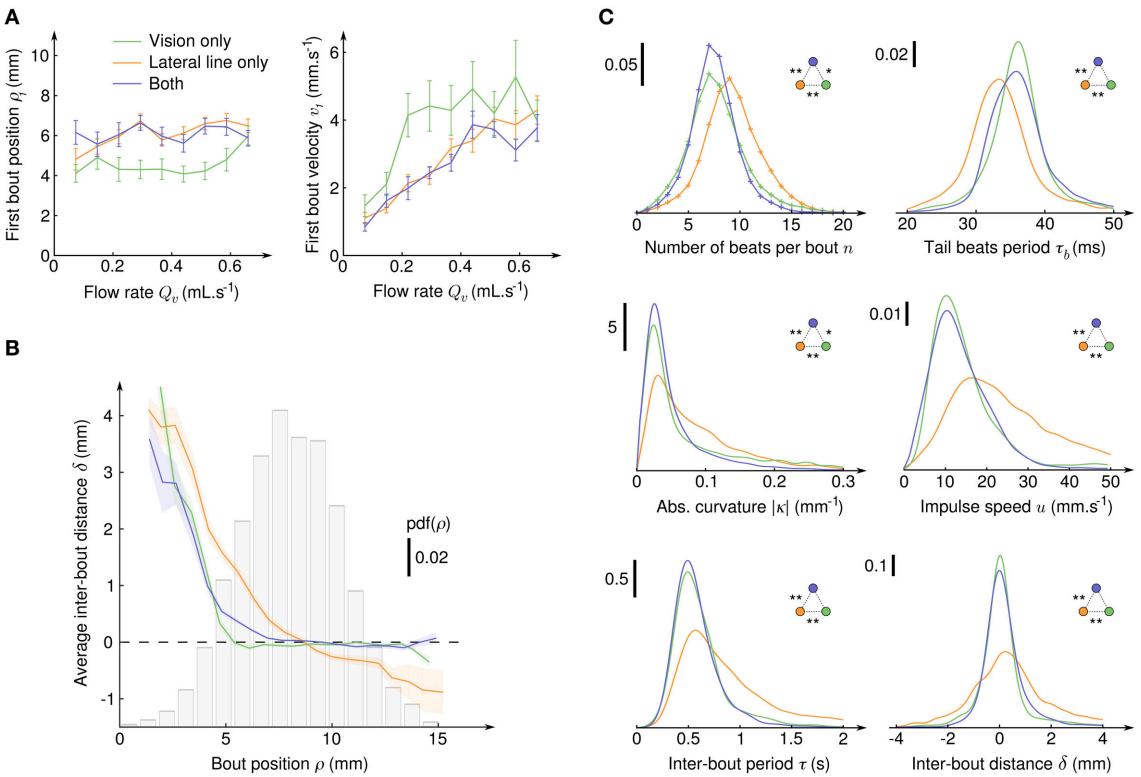

FIGURE 4 | Initiation, characterization and regulation of counterflow swim sequences. (A) Average radial position ρ_1 (left) and fluid velocity v_1 (right) at the onset of the first bout of the CSS as a function of the suction flow rate, for the three sensory conditions where CSS is observed. Error bars: standard error. **(B)** Average inter-bout distance δ as a function of the bout radial position ρ during the CSS. The dashed line at $\delta = 0$ indicates perfect distance holding. The bar plot shows the probability density function of ρ for all three sensory conditions. The colored transparent surfaces indicate standard errors. **(C)** Probability density functions of six quantities characterizing the intra- and inter-bout behavior during the CSS for the three sensory conditions. Pdf were obtained with kernel density estimation with Gaussian kernels: $\sigma_k^n = 0.75$, $\sigma_k^{\tau_b} = 1$, $\sigma_k^{|\kappa|} = 0.01$, $\sigma_k^u = 2$, $\sigma_k^\tau = 0.075$, and $\sigma_k^\delta = 0.25$. Two-sample Kolmogorov-Smirnov tests were used to determine if distributions are significantly different from each other (*$p < 10^{-3}$ and **$p < 10^{-6}$).

so the lateral line can be considered as the dominant sensory system.

After CSS initiation, the distributions of difference in angular position θ between the bouts' onsets and offsets were found Gaussian with large standard deviations (15.4° with lateral line only, 18.6° with vision only and 8.4° with both), indicating that in the course of a trajectory the larvae orientation in the laboratory frame θ varies significantly, although its relative position with respect to the suction point (ρ,α) is held (**Figure 3A**). Though the regulation of the body angle α during CSS appeared to be independent of the sensory condition, the regulation of radial position ρ was found to rely on different mechanisms (**Figure 4B**). With the lateral line only, the average inter-bout distance δ was positive close to the suction point (repulsion) and negative far away (attraction), leading to a stabilization process around an operating point corresponding in the assay to a circle of radius 8.7 mm around the suction point. With vision only, steep repulsion occured below a threshold at 5 mm, while above the threshold a plateau at $\delta = 0$ indicated efficient radial position holding at any distance from the suction point. With both sensory modalities, the fish behaves as with the sole visual system.

The inter-bout distance δ is the result of a complex process involving the inter-bout period τ tuned by the fish and the coupling between body movements and the surrounding medium resulting in bout impulses. The impulse amplitude reads $m.u$ where m is the mass of the larva and u is the impulse speed and depends on the number n of tail beats, the beating period τ_b and tail curvature κ. The distributions of n, τ_b, $|\kappa|$, u, τ, and δ are displayed on **Figure 4C** for the three sensory conditions, as well as the outcome of pairwise two-sample Kolmogorov-Smirnov tests. It appeared that for all these quantities the distributions for the lateral line only and for the visual system only were significantly different, and that the distributions for fishes having both modalities were either very close or undistinguishable from the distributions of the visual system only condition. The visual system thus appeared to be clearly dominant in controlling the swimming patterns during CSS.

2.4. Maturation of the Lateral Line and Visual Systems

To quantify how the CSS evolved with the development of the sensory systems and the associated neural circuits, we exploded the same data according to the age of the larvae (**Figure 5**).

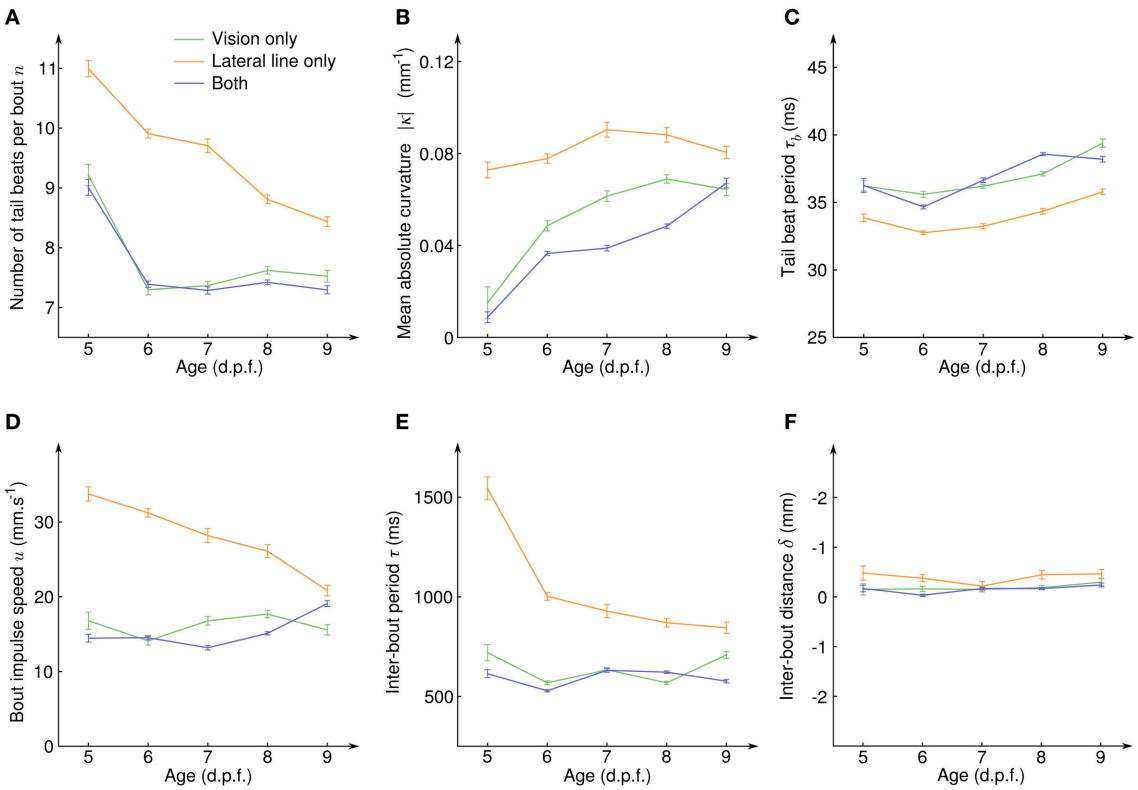

FIGURE 5 | Evolution of the counterflow swimming patterns with age for the different sensory conditions. (A) Average number of tail beats per bout n, **(B)** mean absolute curvature $|\kappa|$, **(C)** mean tail beat period τ_b, **(D)** average bout impulse speed u, **(E)** average inter-bout period τ, and **(F)** average inter-bout distance δ as a function of the larval stage for the three sensory conditions showing CSS. Error bars: standard errors.

For all sensory modalities and at all age, the average inter-bout distance δ was close to zero (**Figure 5F**), indicating than an efficient position holding was always performed. However, how this net result was achieved evolved with age in a different manner for the lateral line and the visual system. With the lateral line system only, the number of tail beats per bout n decreased with age (**Figure 5A**) while the mean absolute tail curvature $|\kappa|$ and the tail beat period τ_b remained constant (**Figures 5B,C**). This resulted in a decreasing bout impulse speed u (**Figure 5D**) which was compensated by a higher swim pace, i.e., a decrease of the inter-bout period τ (**Figure 5E**). With the visual system only, the number of tail beats per bout also decreased (**Figure 5A**) but it was directly compensated by an increase of the mean absolute curvature $|\kappa|$ (**Figure 5B**) and all other quantities (tail beat period, impulse speed, and inter-bout period) remained constant with age. When the fish had both sensory inputs, all the measured quantities showed similar average values than for the visual system only.

3. DISCUSSION

We have developed an assay for studying rheotaxis of freely swimming zebrafish larvae in radial flow geometry. The trajectories revealed two distinct swim phases: exploration, characterized by an active randomization of orientation, and CSS, characterized by an active locking onto the local streamlines direction. The transition between the two swim phases was characterized by a clear and instantaneous reorientation for all sensory conditions showing CSS and at all ages. Passive reorientation was found to be a minor effect in both phases due to the rapid pace of active bouts. During the CSS, the hydromechanical stabilization around $\alpha = 0$ nevertheless facilitated orientation locking by balancing the minute swerves of counterflow swim bouts.

We found that the CSS are triggered on average at a fixed radial distance from the suction point, independantly of the flow rate. This is an exquisitely relevant feature for survival, since it ensures predator avoidance at any flow, even minute. However, the precise combination of sensory cues that allow this behavior is still to be elucidated. Many candidates can be ruled out, including for instance thresholding over any instantaneous cue (e.g., fluid speed, acceleration, hydromechanical gradients, shear rate, etc.) as they depend linearly or super-linearly on the flow rate. It is therefore likely that CSS are initiated on the basis of temporal integration of a quantity that is accessible by both the visual system and the lateral line, but the frequent bouts performed during the exploration phase makes the extraction of a precise quantity very difficult.

Regarding position holding during CSS, two different mechanisms have been found. Though the net result is the same—the fish maintains its position on average in all conditions and at all ages—the compensation mechanisms are different. On one hand, with the visual system position holding is allowed at any distance from the suction point provided it is further than a repulsion limit at ≈1.5 body lengths, and is adjusted during larval development at the level of the bout itself by the number of tail beats and the tail curvature. On another hand, lateral line-mediated position holding relies on attraction and repulsion around an operating point and is tuned during larval development by both the average number of tail beats per bout and the inter-bout period.

The lateral line and visual systems proved to be dominant for distinct tasks. The lateral line, which offers earlier flow recognition, controlled the CSS initation radial position. After CSS initiation, the lateral line system was superseded by the visual system in all aspects of the swimming patterns, down to the tail beat scale. If the larva integrated inputs from both sensory modalities to build its behavioral response, we would expect the latter to differ from the single-modality behaviors and to observe e.g., a mixture of the behavioral features. However, for both CSS triggering and position holding none of measured quantities showed a clear difference with a single-modality condition ; by contraposition, we deduce that the absence of intermediary behavior rules out the possibility of multi-sensory integration during rheotaxis in this age range, in favor of multi-sensory prioritization. In addition, the fact that the swim paterns during CSS are controlled by the visual system does not mean that the lateral line system does not play a role in position holding, and, coherently with the litterature, our results demontrate that it is indeed used as a fallback mechanism. This is ethologically relevant to ensure survival during night time, in opaque water or when the visual system is damaged. Similarly, without the lateral line system the visual system can still trigger CSS, which might be useful in other flow geometries (e.g., with weak velocity gradients).

A closely related behavior is the escape response of small aquatic animals to predators using suction feeding (Engeszer et al., 2007), as the animal has swim away from the predator. The ability to detect and avoid high speed radial flows is critical for their survival, and is likely to be a multisensory process sharing many similarities with rheotaxis in milder flows. Though it is possible to simulate a predator strike in a linear flume (McHenry et al., 2009), the radial flow geometry is more realistic and allows for high experimental troughput. With our apparatus, it would be certainly of great interest to monitor and characterize the transition between position holding and escape responses as the flow rate increases.

4. MATERIALS AND METHODS

4.1. Fish Maintenance and Preparation

Zebrafish (*Danio Rerio*) embryos were obtained from natural spawning of AB wild-type lines. Larvae where reared in Petri dishes on a 14/10 h light/dark cycle at 28°. Eggs where kept in E3 solution with 10^{-5}% Methylene Blue before etching, and then in standard E3 solution. Larvae where fed powdered nursery food every day from 4 to 9 days post-fertilization (dpf). In preliminary experiments we couldn't observe any CSS for larvae younger than 5 dpf, so we used larvae from 5 to 9 dpf for the assay. All experiments were carried out in accordance with approved guidelines and approved by *Le Comité d'Éthique pour l'Expérimentation Animale Charles Darwin* (02601.01).

For experiments in which the lateral line was chemically ablated, larvae were bathed in 10 μM copper sulfate ($CuSO_4$, Sigma-Aldrich) during 2 h and rinsed several times in E3. All the experiments where then performed within 5 h to ensure the neuromasts did not regenerate. We checked the ablation by exposing treated larvae to 0.5 mM DASPEI solution (Sigma-Aldrich) for 40 min and observed the skin with a fluorescence binocular. All neuromast sites showed no or extremely weak fluorescence as compared to control larvae.

4.2. Assay

The assay consisted in a 150 mm-wide Petri dish (Sigma-Aldrich) containing 40–50 zebrafish larvae. A 0.9 mm-inner diameter needle (NN-2038S, Terumo) with a customly flattened and blunted tip was placed horizontally close to the center of the container to generate the aspiration flow (**Figure 1A**). A rectangular piece of transparent polymer (PMMA - 25 × 20 × 4 mm) lied in the field of view at the bottom of the Petri dish to locally reduce the water depth down to 4 mm. The suction needle was tubed to a ballast tank, a peristaltic pump (Ismatec IPC, Wertheim, Germany) and finally a reservoir tank filled with E3. The ballast smoothed the jerky flow generated by the peristaltic pump at high flow rates and served as a storage tank for larvae sucked during the experiment. Each experiment consisted in series of 90 suction/injection cycles. The flow rate during the suction phase was randomly choosen among nine different values ranging linearly from 0.07 to 0.66 mL.s^{-1}. Suction phases lasted no more than 20 s, such that the water depth change was neglectable even at the highest flow rate. During the injection phase, the same amount of water was reinjected in the assay at 0.22 mL.s^{-1}. An electrovalve (LHDA0533115H, The Lee Company) redirected the reinjected flow to a second syringue tip located far away from the suction point (**Figure 1B**). Orthoradial reinjection created a circular flow in the Petri dish which tended to gather the larvae at the center, in the field of view. A 10 s pause was marked between each reinjection and the next run to let the circular flow vanish. Injections/reinjections cycles and camera acquisition were fully automatized and managed by a custom set of programs using LabVIEW (National Instruments, Texas, USA), FlyCapture2 (Point Grey Research, Richmond, BC, Canada), and Sikuli (User Interface Design Group, MIT, Massachusetts, USA).

A Flea3 USB3 Camera (Point Grey Research, Richmond, BC, Canada) with an adjustable macro lens (Zoom 7000, Navitar, USA) recorded a 22 × 18 mm region of interest in the assay from above with a pixel size of 35 m. Trajectories were recorded by the camera in free-running mode at an average framerate of 250 frames.s^{-1} with pixel-encoded timestamps. A dark background was placed under the assay. Raking illumination of the scene

was performed with two high-power infra-red LEDs (850 nm, SFH 4750, Osram). An IR filter (LS387111 LO, Goodfellow, Huntingdon, England) placed in front of the lens blocked all visible light. A 45° mirror was placed in the field of view (**Figure 1A**) to check that larvae where not touching the bottom of the assay. Due to focus loss the mirrored images were too blurred to allow for precise extraction of the vertical position of larvae.

4.3. Image Processing

All data was analyzed using custom-written software in Matlab. On each image, larvae were detected by (i) substracting the run's average image, (ii) applying a Gaussian filter (175 × 175 μm box, σ = 50 μm), (iii) thresholding and filtering objects smaller than 500 pixels (∼50% of a larva).

To evaluate body curvature, we used an approach based on image moments inpired by the work of Rocha et al. (2002) for tracking articulated objects. We evaluated the level-1 *BSP*-tree to obtain two equivalent ellipses of the head and the tail of each larva at each time frame (**Figure 1C** and Supplementary Video 1). The body angle α was defined as the angle between the major axis of the head ellipse and the radial direction. We then considered the intersection of both ellipses' minor axes as the center of curvature and computed the radius of curvature R as the average distance between the center of curvature and all larva's pixels. The curvature was defined as $\kappa = 1/R$ and signed positively when the center of curvature was located on the right of the larva, negatively otherwise. This quantity accurately described the swim tail beats, even at very low amplitude (Supplementary Video 1).

The larvae were then tracked among all images with the algorithm described in Crocker and Grier (1996) with a maximal dispersion of 3.5 mm between two images and a memory of 100 time steps (400 ms). We used a custom graphical user interface to visualize the radial and angular trajectories, bouts and fits (described in the Data Analysis paragraph). We used this interface to manually discard the trajectories that are too short, for which the larva sticked to the bottom of the assay or multiple larvae contacted each other. Series of bouts with a clear motion away from the suction source were defined as CSS.

4.4. Data Analysis

All data was analyzed using software custom-written in Matlab.

Swim bouts were automatially detected based one the curvature signal κ. We first computed $\sigma_{\dot{\kappa}}$ the standard deviation of the derivative of the curvature over a sliding window of 20 ms, and divided it by a baseline trace obtained by taking the average of $\sigma_{\dot{\kappa}}$ below the median value over a large sliding window of 400 ms. Swim bouts were localized when the normalized $\sigma_{\dot{\kappa}}$ stood above a threshold of 5 for more than 40 ms. In each swim bouts the tail beats were automatically detected when the absolute relative curvature stood above a threshold of 0.1.

For each bout, the time at which the radius $\rho(t)$ was minimal defined the impulse start t_k. The radial position traces were then fitted on the 100 ms preceeding each bout by an affine function $\rho(t < t_k) = v_f t + c$ to extract the fluid velocity v_f, and on the 300 ms following each bout (or less if there was another bout in this range) by:

$$\rho(t > t_k) = \rho(t_k) + \lambda u cos(\alpha)(1 - e^{-t/\lambda}) - v_f t \qquad (1)$$

where u is the impulse velocity and λ is the Stoke's drag damping time scale. The latter can be written $\lambda = \Gamma\mu/m$ where μ is the dynamic viscosity, m is the mass of the larva and Γ is a constant solely depending on the geometry of the larva. The typical dimensions and mass of the larvae changed from 5 to 9 dpf (**Supplementary Figure 1A**), but this did not affected the distribution of the fitted λ (Kolmogorov-Smirnov test, $p = 10^{-2}$ between 5 and 9 dpf - **Supplementary Figure 1B**).

The circular variance of body angles α_k at the bouts' onsets is defined as:

$$var_c(\alpha) = 1 - |\frac{1}{N}\sum_{k=1}^{N} e^{i\alpha_k}| \qquad (2)$$

and varies from 0 for minimal dispersion (all angles are similar) to 1 for maximal dispersion (angles compensate exactly, or the distribution is uniform and N is large).

4.5. Simulation of Passive Reorientation

In our geometry the angular speed of a passive larva can be approximated by the non-linear first-order differential equation:

$$\dot{\alpha} = \frac{q}{L\rho} sin(\alpha) \qquad (3)$$

with L the length of the larva, and $q = \frac{Q_v}{2\pi h}$ the surfacic flow rate. This equation holds when $\rho \gg L$, and was solved numerically. We took as initial condition the actual position and body angle of the larvae at the beginning of each experiment.

AUTHOR CONTRIBUTIONS

RO designed and realized the experimental setup, performed the experiments, and contributed to image processing and data analysis. SW contributed to image analysis and animal tracking. AD and VB contributed to data analysis. GD contributed to data analysis and article writing. RC designed the experiment, analyzed data, and wrote the article.

ACKNOWLEDGMENTS

We thank Iris Odsrcil and Florian Engert for fruitful discussion. We also thank the *Institut de Biologie Paris Seine* (IPBS) and the UPMC fish facility for sharing their experience, manpower, and support. This work was financed by the CNRS.

SUPPLEMENTARY MATERIAL

The Supplementary Material for this article can be found online at: http://journal.frontiersin.org/article/10.3389/fnsys.2016.00014

Supplementary Figure 1 | Evolution of the drag coefficient during larval development. (A) Typical dimensions of zebrafish larvae at 5 and 9 dpf. **(B)** Probability density function of the drag coefficient λ at different larval stages.

REFERENCES

Ahrens, M. B., Orger, M. B., Robson, D. N., Li, J. M., and Keller, P. J. (2013). Whole-brain functional imaging at cellular resolution using light-sheet microscopy. *Nat. Methods* 10, 413–420. doi: 10.1038/nmeth.2434

Arnold, G. and Weihs, D. (1977). The hydrodynamics of rheotaxis in the plaice (*Pleuronectes Platessa* L.) . *J. Exp. Biol.* 75, 147–169.

Arnold, G. P. (1974). Rhoetropism in fishes. *Biol. Rev.* 49, 515–576.

Bak-Coleman, J. and Coombs, S. (2014). Sedentary behavior as a factor in determining lateral line contributions to rheotaxis. *J. Exp. Biol.* 217, 2338–2347. doi: 10.1242/jeb.102574

Baker, C. and Montgomery, J. (1999). The sensory basis of rheotaxis in the blind Mexican cave fish, *Astyanax fasciatus*. *J. Comp. Physiol. A* 184, 519–527.

Chagnaud, B. P., Hofmann, M. H., and Mogdans, J. (2007). Responses to dipole stimuli of anterior lateral line nerve Wbres in goldWsh, *Carassius auratus*, under still and running water conditions. *J. Comp. Physiol. A* 193, 249–263. doi: 10.1007/s00359-006-0184-8

Crocker, J. and Grier, D. (1996). Methods of digital video microscopy for colloidal studies. *J. Colloid Interface Sci.* 179, 298.

Dhont, J. K. G. and Briels, W. J. (2005). "Rod-like Brownian particles in shear flow," in *Soft Matter, Vol. 2: Complex Colloidal Suspensions*, chapter 3.10–3.16, eds G. Gompper and M. Schick (Weinheim: Wiley-VCH Verlag GmbH & Co. KGaA), 216–283.

Engeszer, R. E., Patterson, L. B., Rao, A. A., and Parichy, D. M. (2007). Zebrafish in the wild: a review of natural history and new notes from the field. *Zebrafish* 4, 21–40. doi: 10.1089/zeb.2006.9997

Jeffery, G. B. (1922). The motion of ellipsoidal particles immersed in a viscous fluid. *Proc. R. Soc. Lond. A Math. Phys. Eng. Sci.* 1012, 161–179.

Lyon, E. P. (1904). On rheotropism. I. — Rheotropism in fishes. *Am. J. Physiol.* 12, 149–161.

McHenry, M. J., Feitl, K. E., Strother, J. A., and Van Trump, W. J. (2009). Larval zebrafish rapidly sense the water flow of a predator's strike. *Biol. Lett.* 5, 477–479. doi: 10.1098/rsbl.2009.0048

Montgomery, J. C., Baker, C. F., and Carton, A. G. (1997). The lateral line can mediate rheotaxis in fish. *Nature* 389, 960–963.

Olszewski, J., Haehnel, M., Taguchi, M., and Liao, J. (2012). Zebrafish larvae exhibit rheotaxis and can escape a continuous suction source using their lateral line. *PLoS ONE* 7:e36661. doi: 10.1371/journal.pone.0036661

Orger, M. B., Kampff, A. R., Severi, K. E., Bollmann, J. H. , and Engert, F. (2008). Control of visually guided behavior by distinct populations of spinal projection neurons. *Nat. Neurosci.* 11, 327–333. doi: 10.1038/nn2048

Orger, M. B., Smear, M. C., Anstis, S. M., and Baier, H. (2000). Perception of Fourier and non-Fourier motion by larval zebrafish. *Nature* 3, 1128–1133. doi: 10.1038/80649

Panier, T., Romano, S. A., Olive, R., Pietri, T., Sumbre, G., Candelier, R., et al. (2013). Fast functional imaging of multiple brain regions in intact zebrafish larvae using selective plane illumination microscopy. *Front. Neural Circuits* 7:65. doi: 10.3389/fncir.2013.00065

Portugues, R. and Engert, F. (2009). The neural basis of visual behaviors in the larval zebrafish. *Curr. Opin. Neurobiol.* 19, 1–4. doi: 10.1016/j.conb.2009.10.007

Pouget, A., Beck, J. M., Ma, W. J., and Latham, P. E. (2013). Probabilistic brains: knowns and unknowns. *Nat. Neurosci.* 16, 1170–1178. doi: 10.1038/nn.3495

Rocha, L., Velho, L., and Carvalho, P. C. (2002). "Image Moments-Based Strucured and Tracking of Objects," in *Proceedings of the 15th Brazilian Symposium on Computer Graphics and Image Processing* (Fortaleza).

Suli, A., Watson, G. M., Rubel, E. W., and Raible, D. W. (2012). Rheotaxis in larval zebrafish is mediated by lateral line mechanosensory hair cells. *PLoS ONE* 7:e29727. doi: 10.1371/journal.pone.0029727

Van Trump, W. J. and McHenry, M. J. (2013). The lateral line system is not necessary for rheotaxis in the Mexican blind cavefish (*Astyanax fasciatus*). *Integr. Comp. Biol.* 53, 799–809. doi: 10.1093/icb/ict064

Conflict of Interest Statement: The authors declare that the research was conducted in the absence of any commercial or financial relationships that could be construed as a potential conflict of interest.

Active perception and goal-driven navigation in a virtual reality assay

The first models describing goal-driven navigation hypothesized that behavior is produced as a response to modifications of the environment [12]: the behavior could then be broken down in a sequence of stimulus / response where underlying neuronal circuits would operate in an open loop. We know now that this is a very limited description, even for non-vertebrates [13, 14]. To reach goals, animals massively use the feedback of their actions on their sensory system. A more realistic model would be a closed loop (also called feedback loop) where most of the perceived modifications of the environment would be due to the animal's movements. Today, this concept of "active sensing" is at the heart of numerous research activities.

Virtual reality systems – in which the environment is dynamically modified in response to the subject's motion – can be used as an experimental sandbox to probe sensory feedback loops. It is particularly interesting when one considers that the operator can artificially modify the feedback loop (*e.g.* change gains, add delays, etc.) and observe how the system compensate these perturbations.

I (modestly) contributed to setting up a virtual reality setup in the framework of the Ph.D. of Adrien Jouary [15] (Germán Sumbre's lab, IBENS). Indeed, until recently the virtual reality setups for zebrafish larvae could deliver only predefined stimuli triggered on the swim bout onsets [6, 16]. In order to adapt the feedback to features of the movement itself (direction, amplitude) one had to gain several orders of magnitude in the speed of image processing to perform it on-the-fly (typically in less than 15ms). This had been achieved thanks to the image moment analysis I developped (the same than in [17]) which provide the animal's bending only with very few computations.

The entire article in presented below.

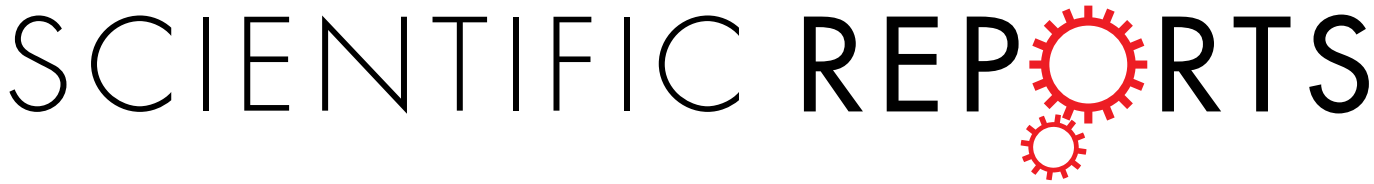

OPEN

A 2D virtual reality system for visual goal-driven navigation in zebrafish larvae

Received: 14 March 2016
Accepted: 06 September 2016
Published: 23 September 2016

Adrien Jouary[1], Mathieu Haudrechy[1], Raphaël Candelier[2] & German Sumbre[1]

Animals continuously rely on sensory feedback to adjust motor commands. In order to study the role of visual feedback in goal-driven navigation, we developed a 2D visual virtual reality system for zebrafish larvae. The visual feedback can be set to be similar to what the animal experiences in natural conditions. Alternatively, modification of the visual feedback can be used to study how the brain adapts to perturbations. For this purpose, we first generated a library of free-swimming behaviors from which we learned the relationship between the trajectory of the larva and the shape of its tail. Then, we used this technique to infer the intended displacements of head-fixed larvae, and updated the visual environment accordingly. Under these conditions, larvae were capable of aligning and swimming in the direction of a whole-field moving stimulus and produced the fine changes in orientation and position required to capture virtual prey. We demonstrate the sensitivity of larvae to visual feedback by updating the visual world in real-time or only at the end of the discrete swimming episodes. This visual feedback perturbation caused impaired performance of prey-capture behavior, suggesting that larvae rely on continuous visual feedback during swimming.

Early behavioral theories described complex goal-driven behaviors as reactive strategies, where behavior is generated only in response to an ever-changing external environment[1]. Therefore, behavior could be decomposed into a sequence of stimulus-response associations, where the neuronal mechanisms underlying these sensorimotor transformations could be studied in open-loop conditions. However, current theories have demonstrated that this is not the case[2], even in simple invertebrate animals[3,4]. Instead, in order to reach a goal, animals rely on the feedback resulting from their actions. Unlike open-loop conditions where external cues are independent from the animal's actions, in behaving animals, actions shape the perception of the environment. Motor-command signals are combined with sensory signals caused by the action of the body on the environment. Together, these signals allow for a continuous evaluation of the relevance of the motor commands.

Virtual reality (VR) systems provide the opportunity to investigate the role of sensory feedback during goal-driven behaviors, by allowing the experimentalist to artificially perturb or alter the sensory feedback. In closed-loop VR, the environment is continuously updated according to the animal's motor responses. Since in VR, the animal's head is restrained, VR systems are compatible with high-resolution functional neuronal recordings, and suitable for studying the neuronal basis of goal-driven behaviors. VR has been successfully applied to study two-dimensional place cells in the rat[5], path integration in the fly[6], and motor adaptation in the zebrafish[7].

Zebrafish is an emerging animal model for studying the neuronal circuit mechanisms underlying goal-directed behaviors. At 6 days post fertilization (dpf), the larva already displays a rich repertoire of visually guided motor behaviors such as prey tracking[8], the optomotor response[9] and phototaxis[10]. In walking animals, leg movements can be measured using a spherical treadmill in head-fixed preparations[11]. However, inferring the displacement intended by the tail movements of a zebrafish larva is not a straightforward task. In the past, two options have been used to record motor activity in zebrafish. The first option relied on "fictive swim", which involves recording, in paralyzed larvae, the activity of a bundle of motor neuron axons[7,12] as an indication of locomotion. Larvae turn using asymmetric tail oscillations. Thus, the direction of the intended movement was obtained by comparing the intensity of the signal recorded from both sides of the tail. Using this method, larvae can perform phototaxis and the optomotor response in a virtual 2D environment[13]. Alternatively, it is possible to monitor tail movements using a high-speed camera when the larva's head is restrained in low-melting agarose[14]. There are several

[1]École Normale Supérieure, PSL Research University, CNRS, Inserm, Institut de Biologie de l'ENS (IBENS), F-75005 Paris, France. [2]Sorbonne Universités, UPMC Univ. Paris 06, UMR 8237, Laboratoire Jean Perrin, F-75005 Paris, France. Correspondence and requests for materials should be addressed to G.S. (email: sumbre@biologie.ens.fr)

advantages to inferring the larva's motion directly from the tail movement kinematics, rather than using "fictive swim". First, due to the variation in the positioning of the electrodes, the fictive swim readout must be calibrated regularly. Second, recording tail movements allows classification of tail movements according to the animal's natural behavioral repertoire[15], or for fine tracking of tail kinematics[16]. Third, neuromuscular-blocking drugs can affect the normal activity of neuronal circuits (unpublished data). Finally, in addition to visual feedback, tail movements provide proprioceptive feedback, absent in paralyzed larvae. Previously, a method for VR using tail-movement kinematics to adjust the visual feedback was developed for the study of unidirectional displacement triggered by whole-field motion stimuli. The difference between successive images of the tail produced 1D forward navigation in the virtual environment[14]. Another method was adapted to provide predefined feedback independent of the kinematics of the tail at the onset of the tail movement[17]. In the latter, the visual feedback was not linked to the kinematics of the tail movements but only to its onset time.

In contrast to these approaches, here we propose a method capable of providing two-dimensional feedback in real time, adapted to different types of tail movements. In order to relate the tail kinematics to the intended displacements of the larvae, we generated a library of larvae movements in free-swimming conditions, containing a diverse sample of the larva's behavioral repertoire. This library enabled us to extract the relationship between tail kinematics and the resulting change in orientation and position of the larva. In head-restrained larvae, this readout was computed in real time to readjust accordingly the visual environment displayed around the larva. Our VR approach enabled the larva to interact meaningfully with its environment in different behavioral contexts. The larvae could change their swimming direction to follow a whole-field motion, and track small moving virtual prey. Perturbation of the delay of the visual feedback affected the success rate of capturing the virtual prey, suggesting that larvae rely on a continuous feedback for navigation. The behavioral database and the code required to infer the trajectory from the tail movements were written in a Python Jupyter Notebook[18]. The code controlling the visual feedback was written in C++. They are all open source and can be downloaded and modified as required (www.zebrain.biologie.ens.fr/codes)

Results

Prediction of the larva's trajectory from the kinematics of tail movements. Zebrafish larvae navigate by producing discrete stereotypical tail movements called swim bouts. In agarose-restrained larvae, the typical frequency of tail oscillations during a bout, is 20 to 30 Hz[19]. In order to provide real-time feedback, tail kinematics should be filmed at high-acquisition rates (typically above 200 Hz). Therefore, the processing of the acquired images must be computed in just a few milliseconds. The Reynold's number of swimming larvae ranges between 50 and 900 Re, which puts them in a transitional flow regime[20], thus neither inertial nor viscous forces can be neglected. This situation is unlike adult fish that swim in flow regime, where approximations could enable the real-time computation of the thrust generated by the tail movements[21]. Real-time computation of the thrust in transitional flow regime is, so far, technically impossible.

To predict trajectories from tail kinematics, we used a data-driven approach to learn the relationship between the tail movement kinematics and the fish displacement in the horizontal plane (two dimensions). We recorded the displacement and tail kinematics from free-swimming larvae to generate a library of tail movements (see Materials and Methods). Our library of movements consisted of ~300 tail bouts from 6–8 dpf nacre larvae. The shape of the tail was quantified by computing the tail deflection[22] (see Fig. 1b and Materials and Methods). Figure 1 shows the time series of the tail deflection associated with stereotypical movements. This quantification of tail kinematics was fast (we used a C++ written algorithm capable of analyzing the tail movements at 200 Hz), and it resulted in a low-noise, smooth oscillating time series. To describe the change in orientation and position of the larvae in the swimming plane, we used three parameters: axial, lateral and yaw speeds (Fig. 2a). Figure 2c shows the kinematic parameters of free-swimming larvae associated with four previously described maneuvers: scoot, J turn, routine turn and C bend[23]. These maneuvers have distinct kinematics and correspond to different behavioral contexts (e.g. J turn is associated with hunting and C bend with escape from predators). Kinematic parameters were chosen to be smooth oscillating times series during swim bouts.

In order to establish the relationship between the oscillating tail deflections and changes in orientation and position of the larva, we used an auto-regressive model with external input (ARX Model). This technique can predict the value of a kinematic parameter (axial, lateral and yaw speed) using a linear combination of both its past value and the past and current values of the tail deflection (see Fig. 2b and Materials and Methods). Thus, a simple regression is needed to fit the relationship between the tail deflection and the resulting trajectories. To assess the significance of our model, we predicted the trajectories in the test dataset of free-swimming larvae (a random set of 20% of the tail bouts in our library), based only on the changes in tail deflection. The resulting trajectories were then compared to the actual trajectories of the larvae. Figure 2c shows that the trajectories resulting from different categories of tail movements can be fitted using the same model. Due to error accumulation, the trajectory predicted from the tail deflection may sometimes diverge from the observed trajectory, but the overall kinematics were similar. The quality of the prediction of the final orientation and position after a tail bout is shown in Fig. 2d. To compute the error between the predicted and the observed paths, we used a bootstrap between the test and the training datasets, in order to get a reliable estimate of our error. The mean square error (MSE) in the prediction of the direction of movements was 19.4° (Fig. 2d.ii), a similar MSE of 23.4° was observed in the prediction of the change in the direction of the larva's head (Fig. 2d.i). The MSE in the prediction of the larva's displacement was 0.3 mm representing 1/10 of the body length of the larva (Fig. 2d.iii). Moreover, we showed that our method was able to generalize by predicting trajectories of tail movements absent in the training set (see Materials and Methods), thus confirming that the ARX method captures the most relevant dynamics of the larva's locomotion.

To create the visual VR system, larvae were head-restrained in a drop of low-melting agarose and placed in a recording chamber (see Materials and Methods). The tail movements were then filmed with a high-speed camera at a frame rate of 200 Hz. Larvae do not track moving gratings faster than 10 Hz[24]. Thus, a video projector with a

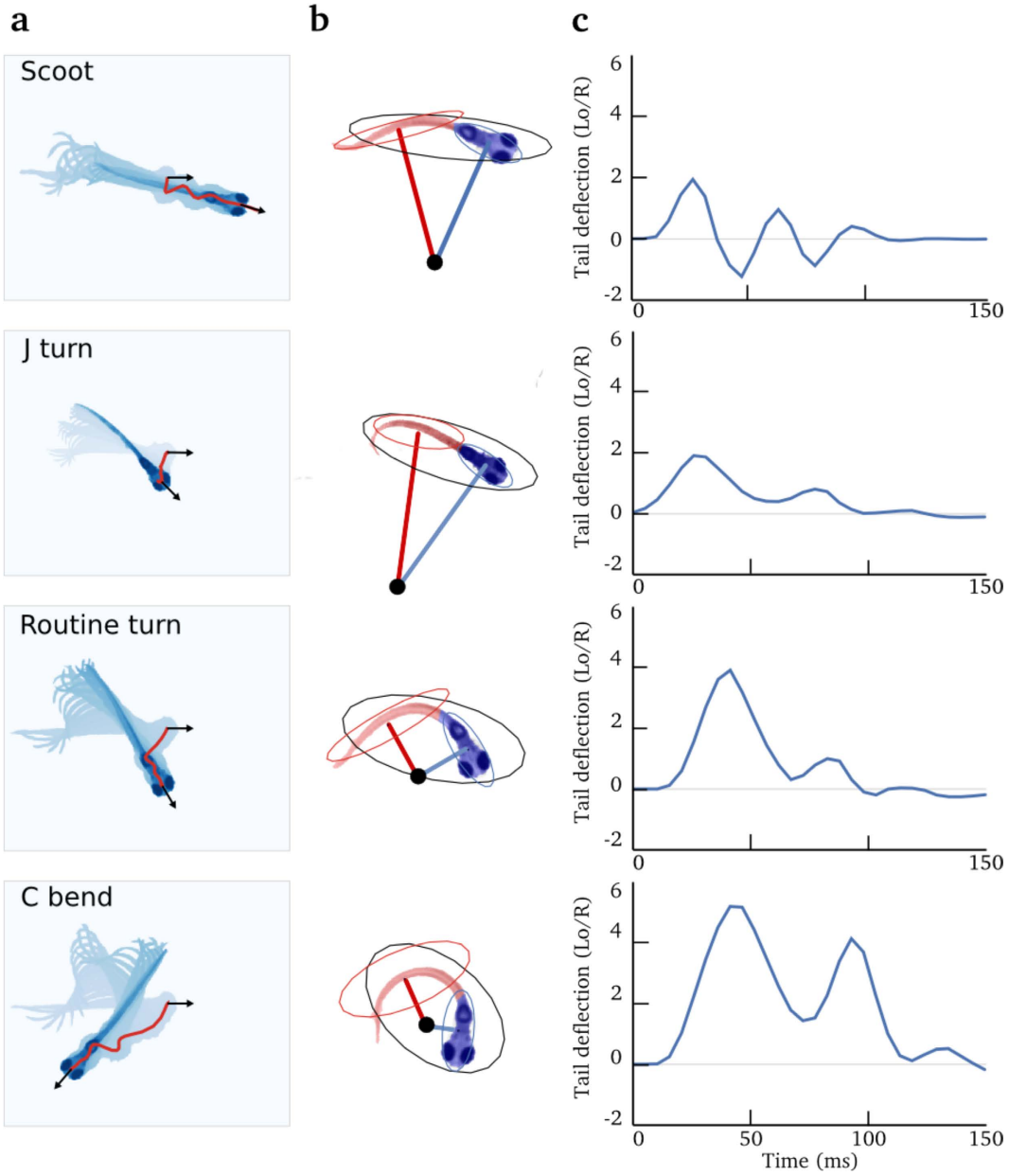

Figure 1. Quantification of tail movements in free-swimming conditions. Row depict movements from different categories. **(a)** Superimposition of the image of a larva during a tail bout. The first image is in light blue and successive images are darker. The path followed by the head is shown by a red line, the black arrows represent the head orientation at the beginning and end of the bout. **(b)** Illustration of the image processing method to a characteristic snapshot of the movement in **(a)**, an ellipse was fitted on the binarized image of the larva (in black). Pixels were split in two groups according to the major axis of the black ellipse: pixels shown in red or blue, superimposed on the larva. For each of these two groups of pixels, a second ellipse was fitted (red and blue ellipse) and the corresponding minor axes were drawn in red and blue. The center of curvature (black dot) was defined as the intersection between the two minor axes. The deflection was defined as the inverse of the average distance between all the pixels in the larva and the center of the curvature ($1/R$). To obtain a dimensionless value, the result was multiplied by the length of the larva at rest L_o. The sign of the deflection was computed as left = negative and right = positive. **(c)** The resulting deflection of the tail over time, for each of the different types of movements in **(a)**.

refresh rate of 60 Hz was adequate for the visual temporal acuity of the zebrafish larva. We computed the time lag of the feedback loop using the following procedure. We modified our C++ VR routine to provide a simple feedback: if the camera sensed higher light level (when a LED was turned on), the monitor screen switched from black to white. We then used two photodiodes and an oscilloscope to compute the delay between the onset of the LED and the onset of the screen illumination. Using this approach, we estimated a latency of 70 ± 10 ms (mean $\pm$ s.t.d).

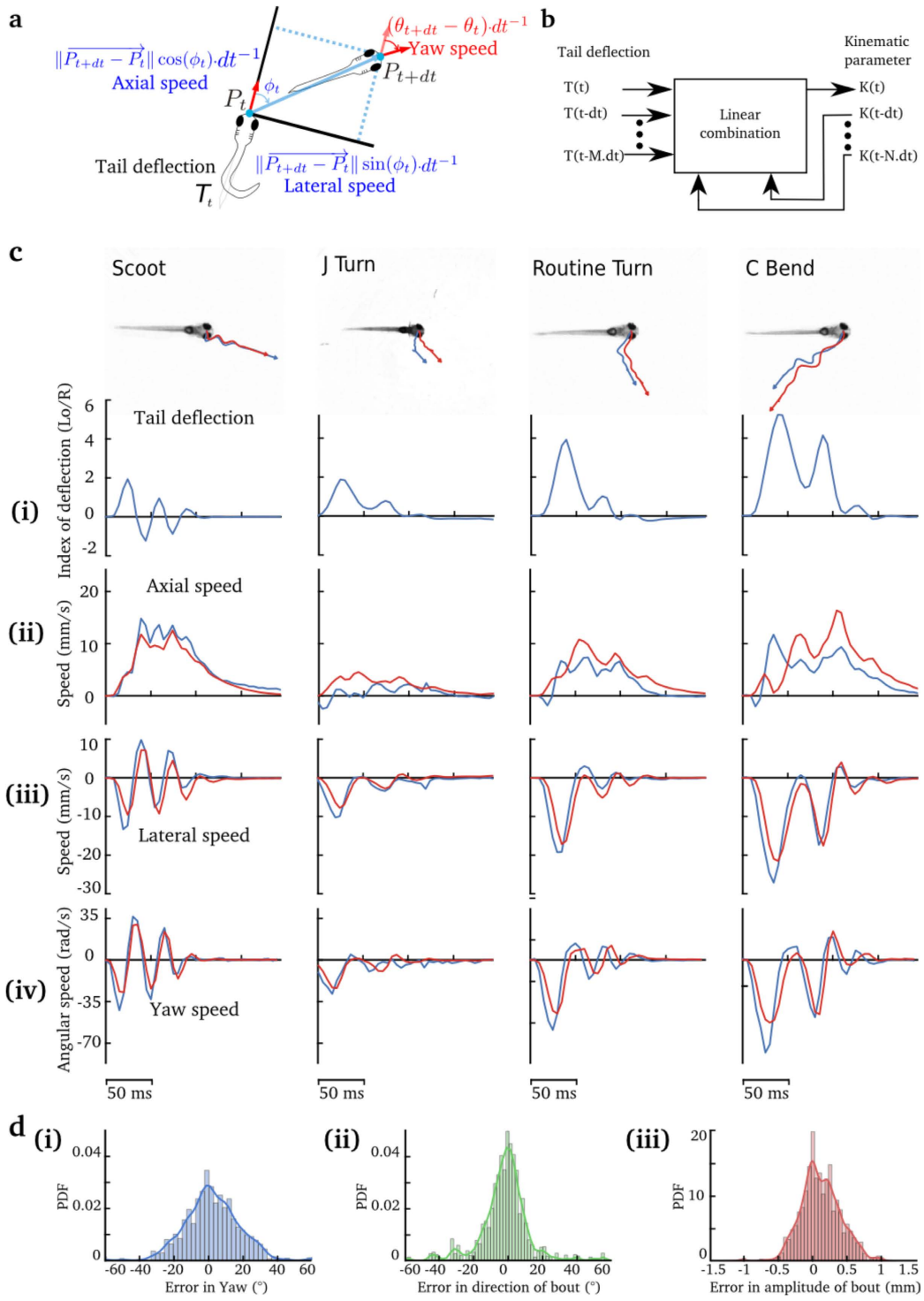

Figure 2. Prediction of the larva's trajectory from the deflection of the tail. (a) Parametrization of the displacement of the larva in the horizontal plane. Only 3 parameters are required to describe the trajectory: the axial, lateral and yaw speed. **(b)** Illustration of the Auto-regressive Model with External Input. Each of the three parameters of trajectory was computed using the tail deflection. Each of the kinematic parameters at time t, $K(t)$ was computed using a linear combination of its past values: $K(t - dt)$, $K(t - 2dt)$, …, $K(t - Ndt)$ and the present and past values of the tail deflection: $T(t)$, $K(t - dt)$, …, $T(t - Mdt)$. See Materials and Methods for details. **(c)** Examples of four different types of movements showing the true path of the larva (in blue) and that predicted (in red). **(i)** Tail deflection corresponding to different categories of movement. **(ii)** The axial speed. **(iii)** The lateral speed. **(iv)** Yaw angle. For each case, the observed kinematic parameter is in red, and the predicted in blue. **(d)** Distribution of the errors between the predicted position and orientation, and those observed, for: **(i)** change in head orientation; **(ii)** direction of movement; **(iii)** amplitude of the tail bout. The results presented in **(c)** and **(d)** were taken from the test dataset.

Using the ARX model, we inferred the changes in kinematic parameters resulting from tail movements in real time and updated accordingly the patterned visual stimuli projected around, or below the larva's recording chamber. The VR software was based on a custom program written in C++, using OpenCV to process images and OpenGL to display the visual environment. The routine required for providing the visual feedback in real time is available at (www.zebrain.biologie.ens.fr/codes). Due to the flexibility of this method, we were able to study different types of visual behaviors. All routines required for the analysis of the library of movements and the generation of the ARX model were programmed in a Python Jupyter Notebook. This approach enables others to reproduce the data analysis, and to easily adapt the code according to their own needs. As a proof of principle, we tested the VR system using two different goal-directed visual behaviors: the optomotor response and prey-capture behavior.

Optomotor response in a two-dimensional visual virtual reality system. When presented with a whole-field coherently moving visual stimulus, zebrafish larvae turn and swim in the direction of the perceived motion. This behavior, known as the optomotor response (OMR), allows the larvae to maintain a stable image of the world on the retina, and thus, a stable position with respect to their visual environment. For example, OMR could prevent larvae from being carried downstream by water currents. The OMR can be reliably evoked in the larvae from 5 dpf and it is maintained throughout the entire lifespan of the fish[25].

Based on previous studies, we chose a grating velocity of 1 cm/s and a spatial frequency of 1 cm projected on a screen placed 0.5 cm underneath the larva[13,14]. At the beginning of each trial, the angle between the initial orientation of the grating and the head direction of the larva was randomly chosen between −180° and 180°. During the stimulation, the speed and orientation of the grating were updated in real time according to the larva's tail kinematics (see Supplementary Movie 1). Each experiment consisted of 120 trials, where each trial was composed of periods of visual stimulation (6 s) and periods in which the grating was steady (20 s). For the data analysis, we only considered and analyzed trials where larvae generated at least one tail bout. The analyzed trials represented 40 ± 7.5% (mean ± s.t.d) of all trials.

When larvae were initially aligned with the direction of the moving gratings, they displayed shorter latencies (Fig. 3f) and swam at an average speed of 0.43 ± 0.25 cm/s in the direction of the moving stimulus (mean ± s.t.d, N = 148 trials, from 5 larvae, Supp. Fig. 2c). The larva's ability to follow and align itself with the whole-field moving stimulus was improved by applying a gain of 3 to the axial speed. This improvement could be explained by the change in tail dynamics when the head is restrained in agarose[19], and/or the lack of feedback from other sensory modalities (e.g. the lateral line). Larvae produced on average 3.26 ± 1.8 bouts per trial (mean ± s.t.d, N = 546 trials, from 9 larvae) and the average bout duration was 313 ± 8 ms (mean ± s.e.m, N = 1783 bouts, from 9 larvae), which is consistent with previous reports[19]. The distribution of angles between the larva and the stimulus direction decreased with time (Fig. 3c,d). Successive bouts brought the angle of the larva's head to an average deviation of 20° ± 2.1° (mean ± s.e.m) with respect to the axis of displacement of the moving grating (Fig. 3g). We considered that a larva was aligned with the direction of the stimulus motion if the angle of its head and the grating motion was lower than 30° (chosen to approximately match the average deviation at the end of the trials, 36.4°, all trials considered). The proportion of aligned larvae increased by two-fold during the 6 s trials (from 28.2% to 51.6%, N = 546 trials, from 9 larvae, Fig. 3e,h).

Because this alignment could result from feedforward motor commands that do not necessarily rely on feedback, we performed a control experiment to test the effect of the visual feedback on the larva's behavior. At the beginning of each trial, the direction of the larva's head was aligned with the movement of the grating. Each experiment was composed of 50 trials in open-loop conditions interleaved with 50 trials in closed loop where the speed and orientation of the grating were updated in real time according to the tail kinematics of the larva. Each trial was composed of periods of visual stimulation (10 s) and periods in which the grating was steady (20 s). In open-loop conditions, the speed of the larvae in the virtual environment increased at the beginning of the trials and decreased after a few seconds (Suppl. Fig. 2a,d). Moreover, the number of scoot tail movements associated with forward swim was significantly higher in the closed-loop conditions (see Materials and Methods and Suppl. Fig. 2e). Because forward scoots have longer durations than turns, the average bout duration was longer when larvae were initially aligned with the direction of the whole-field moving stimulus (517 ms) than in the conditions where the larvae were initially set a random angle with respect to the direction of the moving stimulus (330 ms). The bout durations were shorter in closed-loop (517 ms) than in open-loop conditions (770 ms, Suppl. Fig. 2b, N = 5, p = 0,04, Wilcoxon signed-rank test). This difference in bout duration was already significant at the first bout (536 ± 189 ms in closed loop and 1296 ± 572 ms in open loop, N = 5, p = 0.03, Wilcoxon signed-rank test). Additionally, we observed that larvae reacted to the absence of feedback by increasing the intensity of their tail oscillations during the first bout (Supp. Fig. 2g–f). In certain cases, the lack of feedback led to an abrupt change in tail kinematics during the first bout (Supp. Fig. 2f). These results confirm previous findings[14], and further suggest that within the framework of the OMR, larvae can integrate visual feedback during a bout and react to it by modulating tail deflections adequately (e.g. increase in duration of the bout, interruption or even modulation of amplitude and orientation of the tail oscillations during the first bout, Supp. Fig. 2).

Overall, these results confirm that the trajectory reconstructed from tail movements can be used to provide visual feedback in real time, enabling larvae to orient according to moving visual stimuli, in a 2D visual virtual environment.

Prey capture in a two-dimensional visual virtual reality system. At 5 dpf, zebrafish larvae start hunting prey. This behavior is critical for survival and relies on several decision-making processes. The first step is visual recognition. Larvae rely mostly on vision to capture prey, as demonstrated by the dramatic decrease in the number of prey eaten in the dark[16,26]. Prey capture can also be induced in free-swimming or head-restrained larvae when presenting small moving dots (~4° in size) in the larva's field of view[15,27–30]. This size has been shown to optimally elicit prey capture[15,27,28] and match the natural neuronal circuit tuning of the larva's optic tectum[15,28,30],

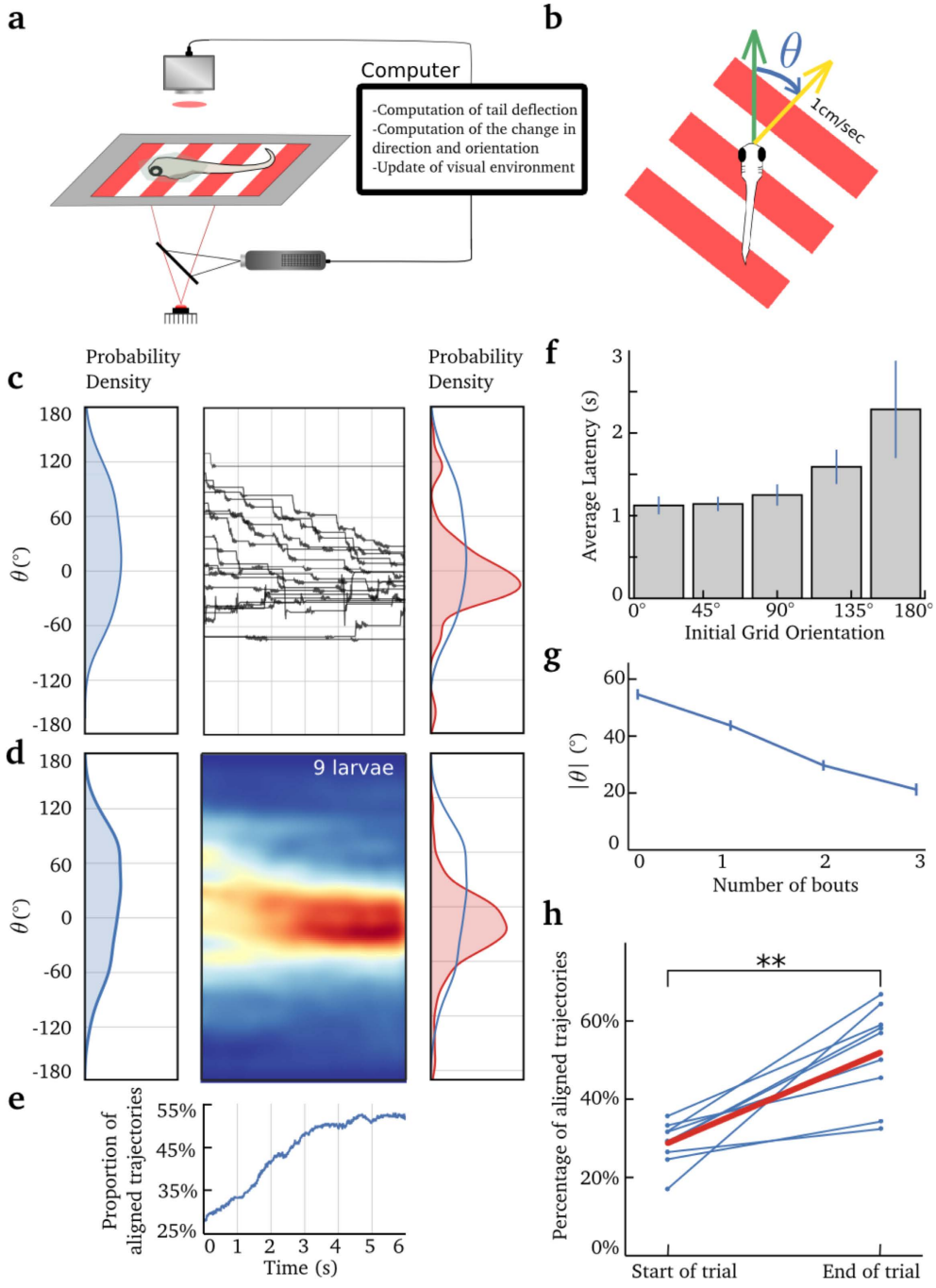

Figure 3. The optomotor response in virtual reality. (**a**) A schematic of the experimental setup. The tail was imaged using a high-speed camera, an IR LED for illumination, and a high-pass filter to prevent the visual stimulus from reaching the camera. A projector was used to display the moving grating on a diffusive screen placed 0.5 cm below the larva. The larva was head-embedded in low-melting agarose at the bottom of a petri-dish. The tail was free to move. **(b)** The grating moved at 1 cm/s. θ represents the difference between the larva's heading direction (green arrow) and the direction of the moving grating (yellow arrow). **(c)** Center panel: example of the changes in θ for one larva (20 trials). Left panel: Initial distribution of θ for the same larva. Right panel: Final orientation ($\theta_{t=6s}$) distribution. The initial orientation distribution ($\theta_{t=0}$) is superimposed in blue for comparison. **(d)** Left panel: Initial orientation distribution for all larvae and all trials for which at least one bout was generated. Center panel: color-coded density of trajectory as a function of time for the 6 s trials. Left panel: Initial distribution of $\theta_{t=0}$ for all larvae. Right panel: Final orientation distribution ($\theta_{t=6s}$) for all larvae. **(e)** Proportion of larvae aligned with the moving stimuli ($\theta_t \in [-30^\circ, 30^\circ]$) as a function of time during the trial. The time scale is common to **(c)**, **(d)** and **(e)**. **(f)** Histogram of latency as a function of the initial orientation of the grating, error bar indicates s.e.m. **(g)** Average of $|\theta|$, for successive bouts, error bar indicates s.e.m. **(h)** Average percentage of trajectories aligned with the moving stimulus ($\theta_t \in [-30^\circ, 30^\circ]$), at the beginning and at the end of the trials, for each larva. The average is shown in red.

the highest visual processing area necessary for visually guided prey detection and capture[26]. As observed for free-swimming larvae, prey capture in head-restrained conditions showed similar locomotor and oculomotor movements intended to bring the larva in front of the virtual prey[17,27]. In contrast, large dots elicited turns away from the stimulus[27,29,31–33]. After detection, the larva initiates a series of bouts to precisely and progressively orient towards and approach the prey. During prey capture, the larva adapts the speed, intensity and directionality of its movements based on the updated position of the prey[16].

Under head-restrained conditions, we reproduced the orientation and pursuit maneuvers toward the virtual prey, in a visual virtual environment (Fig. 4a,b). No increase in gain was applied for this experiment because prey capture relies on small-amplitude movements that are less affected by embedding the head of the larvae in agarose[19]. Experiments consisted of 166 trials. Each trial mimicked a situation where a 100 μm light spot appeared 1.5 mm away from the larva. In this configuration, the apparent angle of the virtual prey (4°) optimally elicited a prey-capture behavior[15,27]. The larva was head-restrained in a drop of low-melting agarose and placed in an elevated stage in the center of a cylindrical recording chamber. At the beginning of each trial, we projected on the circular screen a 4° circular black spot moving on a white background at an angular speed of 20°/s along the azimuthal plane. The black spot began first appeared at ±90° relative to the longitudinal axis of the larva, and moved towards 0° (rostrally).

Immediately after the onset of the larva's first tail bout, the angular speed of the prey in the virtual environment was set to 0°/s. Any further changes in size and position of the black circle projected on the screen depended on the predicted trajectory of the larva. Figure 4b and Supplementary Movie 2 illustrate the experimental design. If the larva oriented itself toward the virtual prey, the black spot was then projected towards the center of the larva's field of view in accordance with the predicted change in yaw, and its radius was increased as the larva swam in its direction. We considered that a larva captured the virtual prey if its trajectory in the virtual environment reached at least 400 μm from the virtual prey (beyond this point, larvae usually execute a maneuver to swallow the prey based on ram or suction[16]). A trial ended after a successful capture, or when the angle between the larva's head and the virtual paramecium exceeded ±90°, the latter representing a failure.

We found that larvae produced at least one tail movement in 14% of the trials (13.8%, N = 6750 trials, from 27 larvae), which is consistent with previous reports[17,27,30]. Figure 4f shows that the tail movements produced during the trials were based more on forward scoots and less on large amplitude movements (routine turns, C bends and bursts) compared to the movements spontaneously produced between trials. This is consistent with the fine maneuvers required to catch the virtual prey.

In trials where at least one tail movement was generated, larvae were able to capture virtual prey on average 16.1% of the time (166 trials per larva, 27 larvae), and up to 40% for the best performing larvae (Fig. 4c). Successful captures of virtual prey were associated with an increase in asymmetric scoot movements (Materials and Methods and Fig. 4g), a category of movements including small amplitude turns such as J turns. As a control experiment, we shuffled the trajectories of the larvae in VR with respect to the position of the virtual prey. For each larva, control paths were generated by associating paths in VR with random virtual-prey locations within the larva's field of view (±90°). Then, we computed the average percentage of captures for the shuffled trajectories. Random trajectories could reach the target in only 4.8% of the cases, compared to 16.1% (Fig. 4c, $p = 1.4^{*}10^{-5}$, Wilcoxon signed-rank test).

Larvae preferentially initiated the first tail bout when the prey was at a ±30° angle in their field of view (Fig. 4e). The larvae performed an average of 3.6 ± 2.6 bouts (mean ± s.t.d, N = 99 successful trials, from 27 larvae) to capture the virtual prey, compared to 4.4 bouts in free-swimming conditions[17]. For cases in which larvae failed to capture the virtual prey, their paths were still oriented toward the final target (Fig. 4d). As observed in freely swimming larvae[16], the first bout coarsely brought the paramecia in front of the larva, and successive finer correcting bouts (including J turns) brought the paramecia progressively closer (Fig. 4g,h). The duration of bouts was 191 ± 29 ms (mean ± s.t.d, N = 27 larvae) as previously reported (188 ms[16]), which is significantly shorter than those observed during OMR (313 ms).

These experiments show that the prey-capture behavior in the 2D visual VR can reproduce previously described characteristics of prey-capture behavior in freely-swimming larvae, thus validating the use of this visual VR system to study the role of visual feedback during fine goal-driven behavior.

Integration of visual information during tail bouts. The visual system could use two potential strategies to provide information about the executed movements. The relative position of external landmarks before and after a bout can provide visual feedback on the result of a motor action. An alternative strategy is to have a continuous update on the action rather than a discrete one, by integrating the angular speed of the visual environment during the movement itself. Computing the cumulative rotation (before and after the movement) would, however, require the visual system to integrate over a large angular displacement and extremely high velocities (the amplitude of oscillations of the head during a turn, can reach velocities of up to 4000°/*s*, Fig. 2c.iv). Previous studies have reported that the larva uses visual feedback following the end of the bouts to compare the observed and the expected position[17]. In this previous study, a predefined feedback was presented at the onset of a tail movement independently of its kinematics. In contrast, our method provides a continuous update of the larva's trajectory according to the tail kinematics.

To test whether visual feedback is used by the larva during the generation of bouts, we altered the visual feedback provided during the swim bouts. More specifically, we performed experiments in which the feedback was updated only at the end of the bout, when the speed was slower than 0.2 mm/s (Fig. 5a and Supplementary Movie 3). This perturbation was introduced in one-third of the trials (83 trials per larva, 27 larvae). In comparison to trials in which visual feedback was provided in real time, the visual-feedback-delayed trials resulted in longer bout durations: 215 ± 42 ms vs. 191 ± 29 ms (mean ± s.t.d, $p = 0.0012$, Wilcoxon signed-rank test, N = 27 larvae; Fig. 5b). Although we did not find significant differences in the categories of movement produced in the two conditions, individual bouts were less successful at reaching the virtual prey in the delayed feedback condition

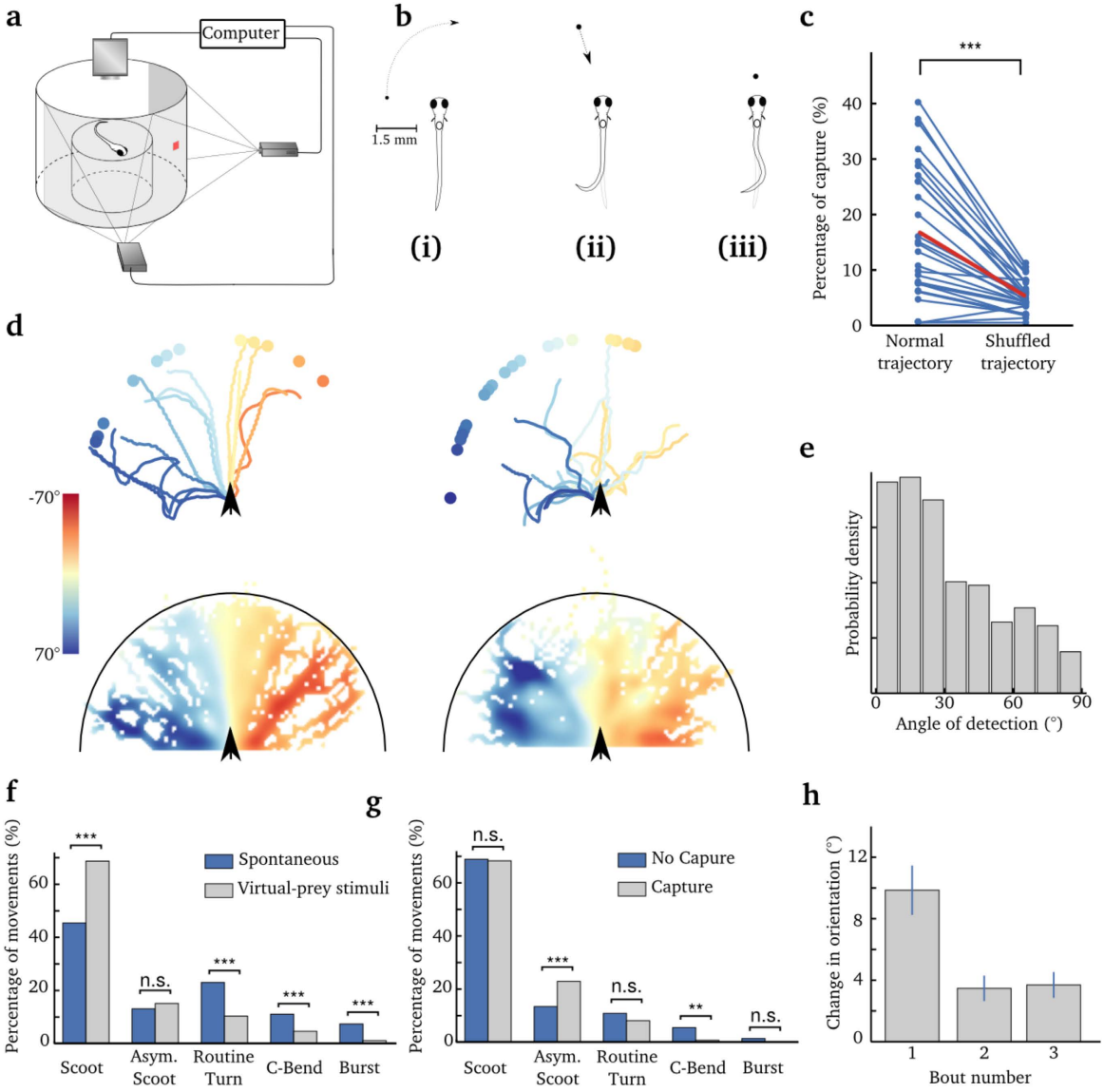

Figure 4. Prey-capture behavior in virtual reality. (a) Schematic of the experimental setup. The larva is positioned on an elevated stage in the center of a cylindrical recording chamber. Visual stimuli were projected on a screen surrounding the recording chamber, covering a field of view of 180°, and centered around the direction of the larva's head. The tail was imaged using a high-speed camera mounted on a binocular. For illumination, an IR LED was placed below the chamber. Two projectors were used to project the virtual prey, each covering a field of view of 90°. **(b)** Presentation of the virtual environment during each trial. (i) The virtual prey of 4° appeared from either side of the larva with an angular speed of 20°/s. (ii) After the onset of the first tail bout, the angular speed of the virtual prey was set to 0°/s and its position on the screen was further updated according to the larva's tail movements only. (iii) A trial was considered successful if the larva got at least 400 μm from the virtual prey. **(c)** Percentage of trials that ended in successful capture of the virtual prey. Only trials where larvae executed at least one tail bout were considered. Left: Each dot represents the performance of individual larvae. Right: The performance obtained by shuffling the angular positions of the virtual prey in each dataset. The red segment depicts the average. ($p = 1.4^{*}10^{-5}$, Wilcoxon signed-rank test). **(d)** Examples of paths of a larva towards the virtual prey. The paths are color-coded according to the position of the virtual prey at the onset of the first tail bout (color bar). Upper panel: Individual paths for one larva. Left: Paths leading to capture. Right: paths failing to capture the virtual prey. Lower panel: Superposition of the trajectories from all larvae (N = 27). Each bin of the meshgrid is color-coded according to the average position of the virtual prey for the trajectory in that bin (color bar). Left: paths leading to capture. Right: Paths failing to capture the virtual preys. In all panels, the black arrows indicate the initial position of larvae. **(e)** Distribution of the angle of the virtual prey at the bout's onset in the first trial. **(f)** Proportion of bouts in each category of movement, during the trials (virtual-prey stimuli) and between trials (spontaneous). Not Significant: $^{*}p > 0.05$, $p < 0.05$, $^{**}p < 0.01$, $^{***}p < 0{,}001$. **(g)** Proportion of bouts in each category of movement for successful or unsuccessful trials. **(h)** Change in head orientation for the first three bouts. Only trials in which larvae performed at least three bouts were considered. Error bar: s.e.m.

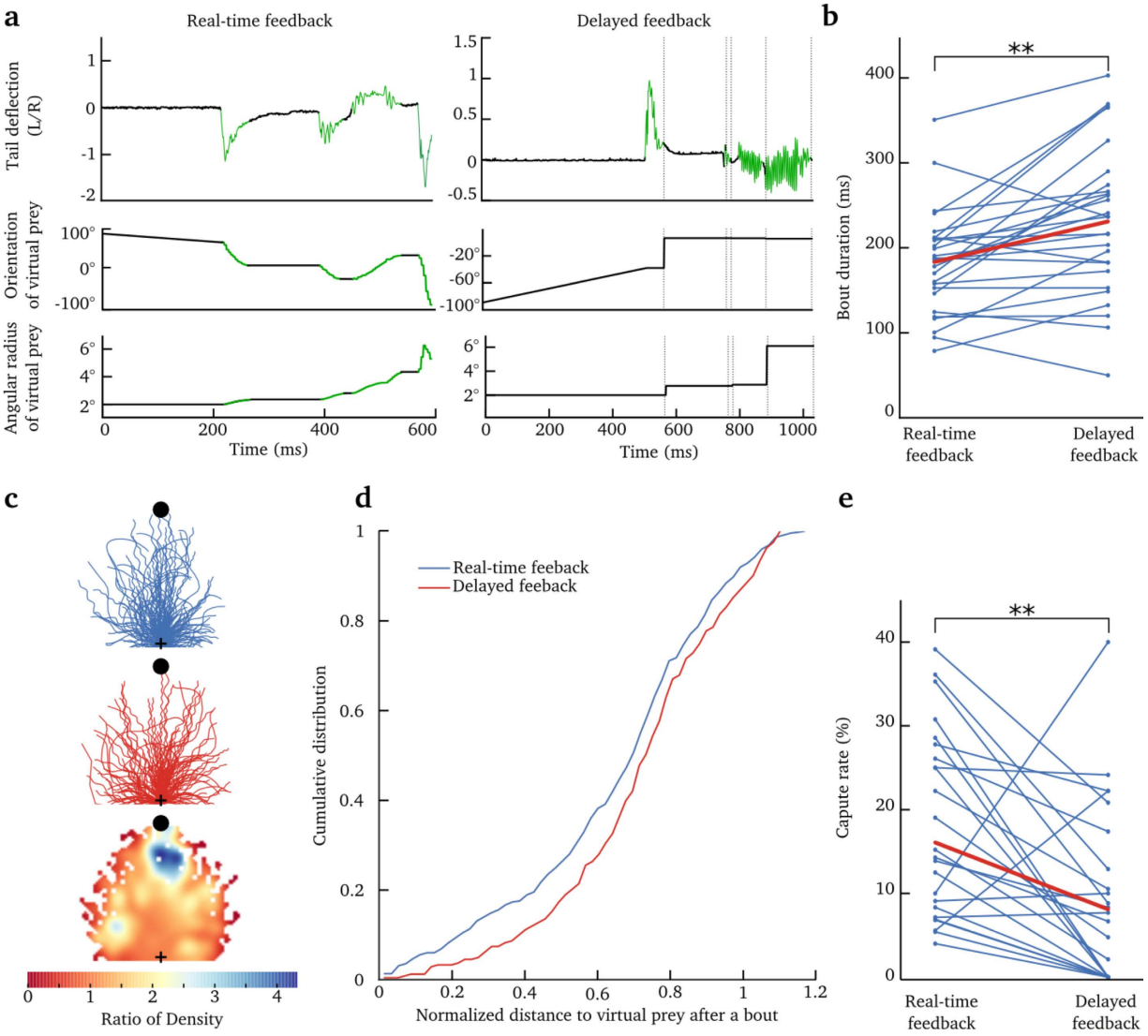

Figure 5. Delayed visual feedback affects prey-capture behavior. (a) Tail deflection of the larva and the corresponding modification of the virtual-prey position (visual feedback): angular position and size of the virtual prey. Left panel: feedback was continuously updated during tail movements (green). Right panel: the feedback was delayed and presented only after the end of the bout (the time indicated by the vertical dashed lines). The green segments on all curves indicate the detection of tail bouts and the corresponding modification in size and position of the virtual prey. **(b)** Average duration of bouts in real-time and delayed feedback conditions, for each larva. The average is shown in red. ($p = 0.0012$, Wilcoxon signed-rank test). **(c)** Normalized bouts: the paths of each bout was rotated and rescaled according to the position of the virtual prey (black dot). The starting position is indicated by the black cross. Upper panel: normalized bouts for all larvae when the feedback was presented in real time. Middle panel: normalized bouts of all larvae, when the feedback was presented at the end of a bout (delayed feedback). Lower panel: ratio of the density of normalized bouts. The color bar indicates the ratio of density between the real-time and delayed feedback conditions (>1 indicates that the density of paths is larger for the real-time with respect to the delayed feedback) **(d)** Cumulative distribution of the normalized distance to the virtual prey at the end each bout, for trials in which the feedback was provided in real time (blue) or after the end of the bout (red). The distribution were significantly different ($p = 0.04$, Kolmogorov-Smirnov test). A normalized distance of 0.5 means that the bouts reduced the distance to the prey by half. **(e)** Percentage of trials that ended in a successful capture of the virtual prey, for real-time feedback (left), and delayed feedback trials (right) (from 27 larvae). The red segment depicts the average.

(Fig. 5c,d, the normalized distance to the virtual prey after a bout is 0.66 ± 0.27 in real-time feedback conditions and 0.73 ± 0.24 in delayed-feedback conditions (mean $\pm$ s.t.d), $p = 0.04$, Kolmogorov-Smirnov test). This subtle change in the visual feedback also decreased the percentage of capture by half from an average of 16% to 8% (Fig. 5e, $p = 0.002$, Wilcoxon signed-rank test).

Moreover, we did not observe significant differences in the inter-bout-interval (IBI) between the real-time ($1.23\,s \pm 1.10\,s$ (s.t.d)) and delayed-feedback conditions ($1.30\,s \pm 1.08\,s$ (s.t.d)). In contrast to previous studies[17],

the paths generated by the larvae were unique and highly variable. This could explain the observed large variability in the IBI and account for our inability to detect significant changes in the IBI between the two conditions.

Overall, these findings suggest that the zebrafish larvae are capable of integrating visual information during movements and not only in-between bouts as previously suggested[17].

Discussion

In contrast to studies in natural conditions, VR systems enable the manipulation of visual feedback, and therefore are ideal to study its role during goal-directed behaviors. To generate the visual VR system, we first determined the speed and orientation of free-swimming larvae from their tail kinematics. For this purpose, we used an autoregressive model fitted on a relatively small library (approximately 300 tail bouts) in order to relate a tail movement to the trajectory of the larvae. As a proof of principle, we first tested our VR system using a whole-field moving stimulus (grating) capable of inducing OMR. Under these conditions, larvae were able to align and swim in the direction of motion using tail bouts of relatively long durations (~300 ms). Larvae presenting initial deviations with respect to the direction of the grating's motion were capable of aligning with the stimulus after 3 tail bouts. When they were aligned with the motion of the grating, the presence of visual feedback increased the proportion of forward scoot movements over turn movements. In open-loop conditions, larvae generated significantly longer bouts of increasing amplitude or could transition from scoot to burst regime within a single bout, as if they were searching for visual feedback. The same VR approach allowed us to study prey-capture behavior in a virtual environment. After detection of the virtual prey, larvae produced a fine tail movement that first coarsely aligned them with the moving virtual prey. Then, using on average two other short duration bouts (~190 ms), larvae were capable of reaching the virtual prey with a success rate of 16% and up to 40% for the best larvae. The paths were associated with fine reorientation maneuvers.

Our method reproduced features of free-swimming navigation during goal-driven behavior (e.g. duration of bouts and reduction in angle with respect to the virtual prey in the first bout). However, we found a difference in the frequency of emergence of spontaneous behavior. In head-restrained conditions, larvae generated fewer tail bouts than in free-swimming conditions: one bout every 1.22 ± 0.16 s in free-swimming conditions (mean $\pm$ s.t.d, from T. W. Dunn *et al.*[34]), in contrast with one bout every 43.3 ± 26.4 s (mean $\pm$ s.t.d, from previous study[35]) in head-restrained conditions. The difference was conserved despite the introduction of a visual-feedback loop in head-restrained conditions. This difference could emerge from the absence of sensory feedback from non-visual modalities (e.g vestibular, lateral line), or from the stress generated by the immobilization of the larvae.

In addition, the control of the visual environment allowed studying of the role of visual feedback on the behavioral performance of the larvae. Previous studies suggested that visual feedback is mostly used by the larvae at the end of the bout[17]. Here, we show that when the visual feedback was updated only at the end of a tail bout rather than in real time, individual bouts were longer and less precise in reaching the virtual prey with a 50% decrease in the prey-capture success rate. These results suggest that larvae are capable of integrating visual feedback and reacting within a swimming bout, despite their short durations and the larva's large head-angular velocities. The discrepancy between our results and those of Trivedi *et al.*[17] could emerge from a difference in the type of feedback provided during movement in the two studies. In the previous study, the paramecia disappeared during movement and reappeared at the end of the bout, at a predefined position. In our case, the virtual prey was always visible, thus providing more robust visual feedback. Overall, our experiments suggest that despite the short duration of the tail bouts, they can be modulated in real time according to the received visual feedback, rather than being feed-forward ballistic movements.

The zebrafish larva is a unique vertebrate model that enables the combination of optogenetics and single-plane illumination microscopy (SPIM) to monitor virtually whole-brain dynamics with near- or single-cell resolution[13,36,37]. To image the larva using SPIM, the larva needs to be head-restrained in low-melting agarose. Although tail movements can be monitored simultaneously, no visual feedback about its own acts is provided. The combination of SPIM and visual VR systems will enable monitoring whole-brain dynamics and behavior in more natural conditions, such as those encountered by the larva when freely swimming. In the future, this method could be used to study the neural mechanisms underlying fine goal-directed behaviors and error correction. Finally, the observation of motor actions in goal-driven navigation is limited by the level of locomotor activity in head-fixed larvae. Prey-capture behaviors could be triggered in only 14% of the trials, similar to previous reports[17,27,30]. In the future, these limitations could be improved by using multi-sensory stimulation[38,39], or by combining the response of larvae with appropriate learning paradigms[40]. A similar methodology could also be applied in juvenile or adult zebrafish in order to study more complex cognitive processes such as social behaviors[41,42] or place conditioning[43] in VR conditions.

Materials and Methods

Zebrafish preparation. Experiments were performed on 6–8 dpf nacre larvae, a mutant lacking melanophores[44]. Embryos were collected, and raised at 28 °C in E3 embryo medium. Larvae were kept on a 14/10 h on/off cycle and fed with paramecia after 5 dpf. For VR experiments, larvae were embedded in low-melting agarose (2%) dorsal side up in the center of the circular recording chamber. After the agarose jellified, the chamber was filled with embryo medium. For OMR experiments, the agarose around the tail was removed up to the swim bladder, using a scalpel. For prey-capture experiments, the eyes were also free to move. All experiments were carried out in accordance with approved guidelines and approved by *Le Comité d'Éthique pour l'Expérimentation Animal Charles Darwin (03839.03).*

Imaging of zebrafish movements. An IR LED (850 nm, IR dragon optic, Osram) was used to illuminate the larvae from below. For imaging the eyes and tail movements, we used a high-speed camera (200 Hz, M3 MotionScope, Redlake) mounted on a microscope (PZMIII-BS, World Precision Instrument). The setup was

placed on an anti-vibration table (Kinetic System vibraplane 2212). In free-swimming conditions, the position and orientation of the larvae were computed by detecting the high contrast eyes of the nacre larva. The tail movements were quantified using the method presented in Fig. 1. An ellipse was fitted on the binarized image of the fish. Then the pixels of the larva's image were split into two groups, according to the major axis of the ellipse, and an ellipse was fitted on each of the two sets of pixels. A center of curvature was defined as the intersection of the minor axis of the two ellipses. From the center, the deflection was defined as the inverse of the average distance between all the pixels in the fish and the center of curvature ($1/R$). The result was multiplied by the length of the fish at rest (L_0) in order to obtain a dimensionless value. The Python code required to extract the paths and tail deflection from the video of a larva is available in an Jupyter Notebook (https://github.com/ajouary/VR_Zebrafish/blob/master/Code/FishTracking.ipynb) for reproducibility and reuse.

Classification of tail bouts. This method uses fuzzy K-nearest neighbor to classify movements according to their similarity with respect to manually labeled tail bouts. We used the Dynamic Time Warping algorithm to compare the time series of tail deflections[35]. Movements were classified in five categories: scoot, asymmetric scoot, routine turn, C bend and burst. Asymmetric scoots included small amplitude turns such as J turns, O bends were grouped along with bursts. This method has a classification accuracy of 82%.

We pooled the movements generated by all larvae and used a Chi-squared test to compute the significance of the difference in the proportions of movements performed in each category for the different conditions (Fig. 4c,d and Supp. Fig. 2.e). We then applied a Bonferroni correction to adjust for multiple comparisons.

Library of tail bouts in free-swimming conditions. We recorded the library containing in total ~300 tail bouts in 5 sessions. The videos were recorded at 200 Hz, with an exposure of 1 ms (M3 MotionScope, Redlake), in a field of view corresponding to 4 cm^2 in the center of a petri-dish containing approximately 10 larvae. Prey-capture trajectories were recorded by introducing paramecia in one of the sessions. C bends and bursts occurred spontaneously, for instance when the wave generated by one larva triggered a startle response in a larva nearby. Only movements that started and finished inside the field of view were kept for further analysis. Although we did not identify individual larvae, we estimated that each larva would not contribute to more than ~5 bouts in the database. Supplementary Figure 1 shows the tail deflections of all the tail bouts in the library, classified according to the movement category they belong to.

Visual stimulation. A pico-projector (refresh rate of 60 Hz, P4x, aaxa) was used for the visual stimulation projected on the diffusive screen (N° 216, White diffusion, Rosco Cinegel). For the OMR experiments in VR, the larva was immobilized the at the center of a petri dish. The stimulus consisted of a square wave grating with a spatial period of 1 cm, at the maximal contrast, projected on a screen placed 5 mm below the larva. For prey-capture experiments, the larva was positioned on an elevated stage within a cylindrical chamber of 5 cm diameters. The cylinder was surrounded by a diffusive screen. Two projectors were placed at ±45° relative to the larva's head direction to create the visual environment. The position of the projectors was chosen to minimize the deformations generated by the curvature of the circular chamber.

Autoregressive Model with External Input. The Autoregressive Model with External Input is a time-domain system identification model which has the following structure:

$$\sum_{k=0}^{N} a_k y(n-k) = \sum_{k=0}^{M} b_k x(n-k) + e(n) \tag{1}$$

In our case, y represents the output kinematic parameters (axial, lateral or yaw speed), x is the input tail deflection and e is the error. k is an index variable corresponding to successive video frames acquired at 200 Hz. $a_0 = 1$ ensures that the resulting system is causal (if $a_0 = 0$, the past value of y depends on the current value of x). M and N represent the size of the memory for the input and output, respectively. The vector of unknown parameters we seek to identify is:

$$\Theta = [a_1, a_2, \ldots, a_N, b_0, \ldots, b_M]^T \tag{2}$$

To identify the unknown variables, we started by observing the system at rest (before the onset of a tail bout). An input signal $x(n)$ is then fed into the system, and the output $y(n)$ is observed for the interval $0 \leq n \leq K$, where n is a temporal index and K is the total number of time steps in the time series:

$$\begin{aligned}
y(0) &= b_0 x(0) + e(0) \\
y(1) &= b_0 x(1) + b_1 x(0) - a_1 y(0) + e(1) \\
&\vdots \\
y(n) &= \sum_{k=0}^{N} b_k x(n-k) - \sum_{k=1}^{M} a_k x(n-k) + e(n) \\
&\vdots \\
y(K) &= \sum_{k=0}^{N} b_k x(K-k) - \sum_{k=1}^{M} a_k x(K-k) + e(K)
\end{aligned} \tag{3}$$

	Trained on Small, Tested on Large	Trained on Large, Tested on Small	Trained on 80%, Tested on 20%
R^2 of Lateral Speed	0.74	0.71	0.67 ± 0.05
R^2 of Axial Speed	0.52	0.77	0.79 ± 0.1
R^2 of Yaw Speed	0.72	0.71	0.72 ± 0.04

Table 1. Each column contains the value of the goodness of fit for the three kinematic parameters evaluated using the ARX model. For the last column, the dataset was split randomly in a train and test dataset containing respectively 80% and 20% of the tail bouts. The goodness of fit was evaluated on the test dataset. This procedure was iterated 100 times leading to an estimate of the mean and the standard deviation for the goodness of fit.

All these equations can be written as a large matrix equation:

$$D\Theta = Y - E \tag{4}$$

With:

$$\begin{aligned} D &= \begin{bmatrix} 0 & 0 & \dots & 0 & x(0) & 0 & \dots & 0 \\ -y(0) & 0 & \dots & 0 & x(1) & x(0) & \dots & 0 \\ \vdots & \vdots & \vdots & \vdots & \vdots & \vdots & \vdots & \vdots \\ -y(n-1) & -y(n-2) & \dots & -y(n-N) & x(n) & x(n-1) & \dots & x(n-M) \\ \vdots & \vdots & \vdots & \vdots & \vdots & \vdots & \vdots & \vdots \\ -y(K-1) & -y(K-2) & \dots & -y(K-N) & x(K) & x(K-1) & \dots & x(K-M) \end{bmatrix} \\ Y &= [y(0), y(1), \dots, y(n), \dots, y(K)]^T \\ E &= [e(0), e(1), \dots, e(n), \dots, e(K)]^T \end{aligned} \tag{5}$$

Thus, the solution for Θ is obtained by a linear regression that minimizes the norm of the error vector. The memory size N and M were chosen to maximize the goodness of fit in the test set. For the lateral and yaw speed we chose $N = 7$ (corresponding to a 35 ms memory), $M = 7$ (35 ms), the input x was the tail deflection. For the axial speed, because this kinematic parameter is mostly positive, we used the absolute value of the tail deflection, $|x|$, as the input with $N = 20$ (100 ms) and $M = 7$ (35 ms). The values obtained for the goodness of fit were $R^2_{Lateral} = 0.67$, $R^2_{Axial} = 0.79$ and $R^2_{Yaw} = 0.72$.

We then tested the ability of the ARX model to fit unobserved trajectories. We split the dataset into two groups of equal size: large or small bouts, according to the maximal tail deflection in each bout. We assessed the goodness of fit of the ARX regression when generalizing between the small and large movements (see Table 1).

Table 1 shows that the axial speed trained on small tail bouts poorly predicted the kinematics of large tail bouts, probably because the measurement of axial displacement is noisier for small tail bouts than for large ones. In the other configurations, the goodness of fit of the regression trained on small movements and evaluated on large movements (and vice-versa) was close to the goodness of fit obtained when training on a mix of small and large bouts. These results demonstrate the ability of our method to predict the kinematics of trajectories outside the training dataset. The Python code required to extract the parameters Θ from a library of tail movements is available in the Jupyter Notebook (https://github.com/ajouary/VR_Zebrafish/blob/master/Code/PredictionTrajectory.ipynb) for reproducibility and reuse.

References

1. Edelman, S. The minority report: some common assumptions to reconsider in the modelling of the brain and behaviour. *Journal of Experimental & Theoretical Artificial Intelligence* **28,** 1–26 (2015).
2. Chen, X. & Engert, F. Navigational strategies underlying phototaxis in larval zebrafish. *Front. Syst. Neurosci.* **8** (2014). http://dx.doi.org/10.3389/fnsys.2014.00039.
3. Mischiati, M. *et al.* Internal models direct dragonfly interception steering. *Nature* **517,** 333–338 (2015).
4. Ofstad, T. A., Zuker, C. S. & Reiser, M. B. Visual place learning in drosophila melanogaster. *Nature* **474,** 204–207 (2011).
5. Aronov, D. & Tank, D. W. Engagement of neural circuits underlying 2d spatial navigation in a rodent virtual reality system. *Neuron* **84,** 442–456 (2014).
6. Seelig, J. D. & Jayaraman, V. Neural dynamics for landmark orientation and angular path integration. *Nature* **521,** 186–191 (2015).
7. Ahrens, M. B. *et al.* Brain-wide neuronal dynamics during motor adaptation in zebrafish. *Nature* **485,** 471–477 (2012).
8. Borla, M. A., Palecek, B., Budick, S. & O'Malley, D. M. Prey capture by larval zebrafish: evidence for fine axial motor control. *Brain, behavior and evolution* **60,** 207–229 (2002).
9. Orger, M. B., Kampff, A. R., Severi, K. E., Bollmann, J. H. & Engert, F. Control of visually guided behavior by distinct populations of spinal projection neurons. *Nature neuroscience* **11,** 327–333 (2008).
10. Burgess, H. A., Schoch, H. & Granato, M. Distinct retinal pathways drive spatial orientation behaviors in zebrafish navigation. *Current biology* **20,** 381–386 (2010).
11. Dombeck, D. A. & Reiser, M. B. Real neuroscience in virtual worlds. *Current opinion in neurobiology* **22,** 3–10 (2012).
12. Vladimirov, N. *et al.* Light-sheet functional imaging in fictively behaving zebrafish. *Nature Methods* **11,** 883–884 (2014).
13. Ahrens, M. B., Orger, M. B., Robson, D. N., Li, J. M. & Keller, P. J. Whole-brain functional imaging at cellular resolution using light-sheet microscopy. *Nature methods* **10,** 413–420 (2013).
14. Portugues, R. & Engert, F. Adaptive locomotor behavior in larval zebrafish. *Front. Syst. Neurosci.* **5** (2011). http://dx.doi.org/10.3389/fnsys.2011.00072.

15. Semmelhack, J. L. *et al.* A dedicated visual pathway for prey detection in larval zebrafish. *eLife* **3** (2014). http://dx.doi.org/10.7554/eLife.04878.
16. Patterson, B. W., Abraham, A. O., MacIver, M. A. & McLean, D. L. Visually guided gradation of prey capture movements in larval zebrafish. *The Journal of experimental biology* **216,** 3071–3083 (2013).
17. Trivedi, C. A. & Bollmann, J. H. Visually driven chaining of elementary swim patterns into a goal-directed motor sequence: a virtual reality study of zebrafish prey capture. *Frontiers in Neural Circuits* **7** (2013). http://dx.doi.org/10.3389/fncir.2013.00086.
18. Pérez, F. & Granger, B. E. Ipython: a system for interactive scientific computing. *Computing in Science & Engineering* **9,** 21–29 (2007).
19. Severi, K. E. *et al.* Neural control and modulation of swimming speed in the larval zebrafish. *Neuron* **83,** 692–707 (2014).
20. McHenry, M. J. & Lauder, G. V. The mechanical scaling of coasting in zebrafish (danio rerio). *Journal of Experimental Biology* **208,** 2289–2301 (2005).
21. Bergmann, M. & Iollo, A. Modeling and simulation of fish-like swimming. *Journal of Computational Physics* **230,** 329–348 (2011).
22. Olive, R. *et al.* Rheotaxis of larval zebrafish: Behavioral study of a multi-sensory process. *Front. Syst. Neurosci.* **10** (2016). http://dx.doi.org/10.3389/fnsys.2016.00014.
23. Budick, S. A. & O'Malley, D. M. Locomotor repertoire of the larval zebrafish: swimming, turning and prey capture. *Journal of Experimental Biology* **203,** 2565–2579 (2000).
24. Rinner, O., Rick, J. M. & Neuhauss, S. C. Contrast sensitivity, spatial and temporal tuning of the larval zebrafish optokinetic response. *Investigative ophthalmology & visual science* **46,** 137–142 (2005).
25. Bilotta, J. Effects of abnormal lighting on the development of zebrafish visual behavior. *Behavioural brain research* **116,** 81–87 (2000).
26. Gahtan, E., Tanger, P. & Baier, H. Visual prey capture in larval zebrafish is controlled by identified reticulospinal neurons downstream of the tectum. *The Journal of neuroscience* **25,** 9294–9303 (2005).
27. Bianco, I. H., Kampff, A. R. & Engert, F. Prey capture behavior evoked by simple visual stimuli in larval zebrafish. *Front. Syst. Neurosci.* **5** (2011) http://dx.doi.org/10.3389/fnsys.2011.00101.
28. Romano, S. A. *et al.* Spontaneous neuronal network dynamics reveal circuit's functional adaptations for behavior. *Neuron* **85,** 1070–1085 (2015).
29. Barker, A. J. & Baier, H. Sensorimotor decision making in the zebrafish tectum. *Current Biology* **25,** 2804–2814 (2015).
30. Bianco, I. H. & Engert, F. Visuomotor transformations underlying hunting behavior in zebrafish. *Current Biology* **25,** 831–846 (2015).
31. Dunn, T. W. *et al.* Neural circuits underlying visually evoked escapes in larval zebrafish. *Neuron* (2016).
32. Temizer, I., Donovan, J. C., Baier, H. & Semmelhack, J. L. A visual pathway for looming-evoked escape in larval zebrafish. *Current Biology* **25,** 1823–1834 (2015).
33. Burgess, H. A. & Granato, M. Modulation of locomotor activity in larval zebrafish during light adaptation. *Journal of Experimental Biology* **210,** 2526–2539 (2007).
34. Dunn, T. W. *et al.* Brain-wide mapping of neural activity controlling zebrafish exploratory locomotion. *eLife* **5** (2016). http://dx.doi.org/10.7554/elife.12741.
35. Jouary, A. & Sumbre, G. Automatic classification of behavior in zebrafish larvae. *bioRxiv* (2016) http://www.biorxiv.org/content/early/2016/05/10/052324.full.pdf.
36. Panier, T. *et al.* Fast functional imaging of multiple brain regions in intact zebrafish larvae using selective plane illumination microscopy. *Frontiers in Neural Circuits* **7** (2013) http://dx.doi.org/10.3389/fncir.2013.00065.
37. Wolf, S. *et al.* Whole-brain functional imaging with two-photon light-sheet microscopy. *Nature methods* **12,** 379–380 (2015).
38. Candelier, R. *et al.* A microfluidic device to study neuronal and motor responses to acute chemical stimuli in zebrafish. *Sci. Rep.* **5,** 12196 (2015). http://dx.doi.org/10.1038/srep12196.
39. Yokogawa, T., Hannan, M. C. & Burgess, H. A. The dorsal raphe modulates sensory responsiveness during arousal in zebrafish. *The Journal of Neuroscience* **32,** 15205–15215 (2012).
40. Roberts, A. C., Bill, B. R. & Glanzman, D. L. Learning and memory in zebrafish larvae. *Frontiers in Neural Circuits* **7** (2013) http://dx.doi.org/10.3389/fncir.2013.00126.
41. Dreosti, E., Lopes, G., Kampff, A. R. & Wilson, S. W. Development of social behavior in young zebrafish. *Frontiers in Neural Circuits* **9** (2015) http://dx.doi.org/10.3389/fncir.2015.00039.
42. Arganda, S., Pérez-Escudero, A. & de Polavieja, G. G. A common rule for decision making in animal collectives across species. *Proceedings of the National Academy of Sciences* **109,** 20508–20513 (2012).
43. Mathur, P., Lau, B. & Guo, S. Conditioned place preference behavior in zebrafish. *Nature protocols* **6,** 338–345 (2011).
44. Lister, J. A., Robertson, C. P., Lepage, T., Johnson, S. L. & Raible, D. W. Nacre encodes a zebrafish microphthalmia-related protein that regulates neural-crest-derived pigment cell fate. *Development* **126,** 3757–3767 (1999).

Acknowledgements

This work was supported by EraSysBio+ Zebrain, ERC stg 243106, ANR-10-LABX-54 MEMO LIFE, ANR-11-IDEX-0001-02 and the PSL Research University. A.J acknowledges support from the *Fondation pour la Recherche Médicale* and the ENS Cachan. We thank P. Gongal for editorial assistance.

Author Contributions

A.J. conceived the experiments, performed behavioral assay in free-swimming conditions, analyzed the data, and built the setup and software. M.H. carried out VR assay and participated in discussions about the experiments. R.C. developed the method for computing the deflection index and ran analysis on tail movements in free-swimming conditions. A.J. and G.S. designed the project and wrote the manuscript.

Additional Information

Supplementary information accompanies this paper at http://www.nature.com/srep

Competing financial interests: The authors declare no competing financial interests.

How to cite this article: Jouary, A. *et al.* A 2D virtual reality system for visual goal-driven navigation in zebrafish larvae. *Sci. Rep.* **6**, 34015; doi: 10.1038/srep34015 (2016).

Chapter 3

Functional imaging with light sheet microscopy

Contents

Calcium imaging in zebrafish larvae

Calcium imaging

This imaging technique is based on recording fluorescent reporters whose quantum efficiency or absoption/emission wavelenghts depend on Ca^{2+} concentration in the neurons. When the membrane is depolarized, ion channels open, let calcium ions enter the soma and fluorescence increases. In contrast with sodium or potassium ions which are present at a high concentration in the soma, the concentration of calcium ions in a resting neuron is relatively low. During a spike, the calcium concentration can be multiplied by a factor 10 to 100 [5], while the concentration of the other ions have lower fluctuations. Calcium is thus a reporter of choice for neural activity since it maximizes the fluctuations of fluorescence during a spike [18, 19].

Two families of calcium indicators are currently available: synthetic and genetically encoded (GECI). Synthetic reporters have to be injected in every sample beforehand, and even if their dynamic is excellent it presents many drawbacks: the injection is invasive, the resulting spatial distribution is highly heterogeneous and the reporter's lifetime is only a few hours long

(afterwards the signal-to-noise ratio severely drops). *A contrario*, genetically encoded calcium reporters are "naturally" expressed by the transcription/traduction process at the level of the cell. In addition to their relative ease of use, they offer an homegeneous repartition, a longer lifetime (typ. a week) and the ability to target certain neuronal populations by using specific promoters. On the other hand, their dynamics is slow and doesn't allow for single spike resolution.

Calcium reporters

So far, at the LJP we have essentially used genetically encoded reporters from the GCaMP familly. They are composed of cpEGFP, a green fluorescence protein designed to fold circularly, binded to a calmoduline (CaM) molecule and a synthetic peptide M13 [20]. The cpEGFP is fluorescent even without calcium ions, with maximal absoprtion at 485 $nm$and maximal emission at 515 nm. Calmoduline is naturally present in the soma and plays a signalling role for calcium ions. The fixation of calcium ions on CaM induces a change in conformation of the M13 peptide, which in turn changes the conformation of the cpEGFP and increases its quantum efficiency.

We have used several generations of GCaMP, with various signal-to-noise ratios and rise / decay times. Starting from GCaMP6, one can choose between 3 reporters with different decay times: GCaMP6f ($\simeq$600 ms), GCaMP6m ($\simeq$1.5 s) and GCaMP6s ($\simeq$3 s). We use mostly GCaMP6f. In the future, we would like to extend our panel of calcium reporters, especially with RCaMP [21] (absorption at 600 nm) which is compatible with channelrhodopsin (absorption at 480 nm).

Limitations of point-scanning microscopes

Recording *in vivo* neural activity cannot be done with a simple epifluorescence microscope since it is designed for thin, quasi-2D samples. To image inside a 3D sample there is a need to discard out-of-focus photons, a technique called *optical sectionning* [22]. The confocal microscope is the most widespread setup to feature optical sectionning: a pinhole conjugated with the objective's focal point blocks most of the photons coming from out-of-focus regions. This allows to measure fluorescence in a single point of the sample, *i.e.* a voxel. One then have to scan the whole sample to obtain the complete volume, voxel by voxel.

Another type of optical sectionning is to prevent the fluorescent photons to be emitted in out-of-focus regions. This is the principle at play in 2-photon microscopes [23] and is quite common for calcium imaging [24]. An

infrared laser at approximately twice the absorption wavelength is focalized on a point of the sample, such that two photons of low energy arriving simultaneously on the same molecule can bring a sufficient amount of energy to trigger fluorescence and the emission of a single photon of high energy, in the visible spectrum. According to this mecanism, emission is localy proportional to the square of the excitation beam intensity; in practice this means that one needs a high photon density – both spatially and temporally – to make emission a probable event. This is the case only around a tiny volume close to the objective's focal point. As for the confocal microscope, this point has to be scanned to image the whole sample volume.

This point-scanning feature of both setups impose a severe limitation as the time necessary to record a complete volume is proportionnal to the number of voxels, and hence there is a tradeoff between the acquisition frequency and the number of voxels per volume. Though technical improvements (like acquisition parallelization [25] or smart startegies to image only relevant voxels [26]) allows some gain in data throughput, a real performance breakthrough could only come from a different microscope design.

The light sheet microscope

Light sheeet illumination allows precisely for imaging simultaneously the whole focal plane, instead of the focal point. However, to keep optical sectionning only the focal plane should be illuminated. To that aim, the sample is lighten up from the side with a laser light sheet precisely aligned on the observation objective focal plane. Thus, in contrast with point-scanning fluorescence microscopes the light pathes for excitation and observation are physically dissociated and there are two objectives, one for excitation and one for observation.

With this geometry, one can image the whole focal plane at once with a standard camera. The field of view (FOV) and the acquisition frequency are now decoupled: the FOV depends on the observation objective (magnification, numerical aperture) and the sensor size, while the acquisition frequency depends on the power of the emitted light and the camera specifications (speed, sensitivity, noise). The recent development of objectives with intermediate magnification and high numerical aperture and of sCMOS cameras with large sensors, high frequency and high sensitivity allowed for a maximization of the efficiency of this imaging geometry and high data throughput.

In addition to the gain in data throughput, light sheet microscopy has a relatively mild effect on the sample as compared to point-scanning micro-

scopes. With the latters, a large fraction of photons absorbed by the tissues do not contribute to the final image. In the light sheeet geometry only the imaged zone is illuminated which limits to the minimum photobleaching and phototoxicity. In addition, as those effects are generally non-linear a continuous illumination is generally favorable.

This last point has been the early motivation for developping light sheet imaging to record the full embryogenesis of drosophilae, and then of zebrafish larvae. In 2004, Huisken *et al.* showed that light sheet microscopy could image all the mucles of a fixed $4\,dpf$. Medaka larvae [27]. The axial resolution was $6\,\mu m$with a field of view of 1,5 x 0,9 mm. The same setup has then been employed to image a drosophila embryo with 56 planes every 5 minutes for 17 hours.

In 2008, Keller *et al.* built a setup with $1\,\mu m$resolution and a FOV of 700 x $700\,\mu m$ [28]. The authors followed the development of a zebrafish embryo for which all cell nuclei expressed GFP. The resolution was sufficient to see cellular divisions. In order to follow all displacements and cellular divisions, 400 images per minute where produced for more than 24 hours.

The high data throughput has then been employed for calcium imaging in 2008 in Holekamp *et al.* during *ex-vivo* recrodings of neural activity in the mouse excised vomeronasal organ [29]. To keep the sample horizontal, the illumination and observation branches are tilted at $\pm 45^\circ$ from the vertical plane. In a FOV of 700 x $100\,\mu m$, 88 neurons could be recorded at $200\,fps$. The fluorescent Oregon green BAPTA-1 reporter was injected, and single spikes could be isolated if they were more than $50\,ms$apart.

In the continuation of these works, we have applied the same microscopy technique to calcium imaging in zebrafish larvae, whose dimensions and transparency were decisive assets to perform brain-wide *in vivo* recordings of neural activity. The following article details all the technical aspects of our first light sheet setup developped at the LJP, including many aspects of image processing and data analysis.

frontiers in
NEURAL CIRCUITS

METHODS ARTICLE
published: 09 April 2013
doi: 10.3389/fncir.2013.00065

Fast functional imaging of multiple brain regions in intact zebrafish larvae using Selective Plane Illumination Microscopy

Thomas Panier[1], Sebastián A. Romano[2,3,4], Raphaël Olive[1], Thomas Pietri[2,3,4], Germán Sumbre[2,3,4], Raphaël Candelier[1] and Georges Debrégeas[1]*

[1] *CNRS/UPMC Laboratoire Jean Perrin, Université Paris 6, Paris, France*
[2] *Ecole Normale Supérieure, Institut de Biologie de l'ENS, IBENS, Paris, France*
[3] *Inserm, U1024, Paris, France*
[4] *CNRS, UMR 8197, Paris, France*

Edited by:
Gonzalo G. De Polavieja, Instituto Cajal. CSIC, Spain

Reviewed by:
Rainer W. Friedrich, Friedrich Miescher Institute for Biomedical Research, Switzerland
Johann Bollmann, Max Planck Institute for Medical Research, Germany

****Correspondence:***
Georges Debrégeas, CNRS/UPMC Laboratoire Jean Perrin, Université Paris 6, FRE 3231, 4 place Jussieu, 75005 Paris, France.
e-mail: georges.debregeas@upmc.fr

The optical transparency and the small dimensions of zebrafish at the larval stage make it a vertebrate model of choice for brain-wide *in-vivo* functional imaging. However, current point-scanning imaging techniques, such as two-photon or confocal microscopy, impose a strong limit on acquisition speed which in turn sets the number of neurons that can be simultaneously recorded. At 5 Hz, this number is of the order of one thousand, i.e., approximately 1–2% of the brain. Here we demonstrate that this limitation can be greatly overcome by using Selective-plane Illumination Microscopy (SPIM). Zebrafish larvae expressing the genetically encoded calcium indicator GCaMP3 were illuminated with a scanned laser sheet and imaged with a camera whose optical axis was oriented orthogonally to the illumination plane. This optical sectioning approach was shown to permit functional imaging of a very large fraction of the brain volume of 5–9-day-old larvae with single- or near single-cell resolution. The spontaneous activity of up to 5,000 neurons was recorded at 20 Hz for 20–60 min. By rapidly scanning the specimen in the axial direction, the activity of 25,000 individual neurons from 5 different z-planes (approximately 30% of the entire brain) could be simultaneously monitored at 4 Hz. Compared to point-scanning techniques, this imaging strategy thus yields a $\simeq$20-fold increase in data throughput (number of recorded neurons times acquisition rate) without compromising the signal-to-noise ratio (SNR). The extended field of view offered by the SPIM method allowed us to directly identify large scale ensembles of neurons, spanning several brain regions, that displayed correlated activity and were thus likely to participate in common neural processes. The benefits and limitations of SPIM for functional imaging in zebrafish as well as future developments are briefly discussed.

Keywords: zebrafish model system, spontaneous activity, correlation analysis, neuroimaging, imaging, three-dimensional, light-sheet imaging

INTRODUCTION

Cognitive processes generally implicate extended neural networks spanning several areas of the brain. In order to shed light on the neural basis of these processes, it is thus necessary to simultaneously monitor the dynamics of multiple brain regions with single-cell resolution (Alivisatos et al., 2012). In striking contrast with this requirement, current experimental methods sample a small number of neurons located in a single brain area. Silicon-based nanoprobes allow electrophysiologists to simultaneously record up to a few hundred neurons (Du et al., 2011; Stevenson and Kording, 2011). Their future development is however limited by the intrinsically invasive nature of the technique. In the last two decades, functional imaging approaches, in which the neurons' spiking dynamics is monitored *via* the increase in fluorescence of calcium-binding reporters, have allowed to partially circumvent this limitation (Grienberger and Konnerth, 2012). Further assets of neuro-imaging, with respect to electrophysiology, include the accurate localization of the monitored neurons, the possibility to distinguish cell identity using specific markers and the precise manipulation of neural activity using optogenetic methods (Wyart et al., 2009).

Imaging of three-dimensional fluorescent tissues requires optical sectioning, which is generally obtained by using confocal or two-photon microscopy (Denk et al., 1990; Yuste and Denk, 1995; Bollmann and Engert, 2009). These point-scanning microscopy (PSM) approaches in turn impose a drastic limit in recording speed: in order to collect a significant number of photons in a given voxel, a minimum laser dwelling time of the order of 1 µs is needed (Holekamp et al., 2008). This yields a bound of roughly 10^6 voxels per second in acquisition rate, which, even with optimized scanning trajectories (Salomé et al., 2006; Lillis et al., 2008; Grewe et al., 2010; Katona et al., 2012), limits the number of neurons that can be dynamically recorded.

In recent years, selective-plane illumination microscopy (SPIM) has been rediscovered in the context of embryo development (Mertz, 2011; Tomer et al., 2011; Weber and Huisken, 2011)

and physiology (Huisken et al., 2004; Verveer et al., 2007; Keller and Dodt, 2012). In this imaging configuration, optical sectioning is performed through side-on illumination of the sample by a thin (micrometer-thick) laser sheet, whereas fluorescence photons are collected by a camera whose optical axis is orthogonal to the illumination plane. One of the significant assets of this approach, compared to PSM, lies in the fact that different regions in the focal plane are simultaneously illuminated and are thus exposed for a much longer time in average. As a result, the data throughput is in practice limited by the camera transfer rate, which is currently of the order of a few hundreds of Mpixels per second for highly sensitive sensors.

The strongest limitation of light-sheet microscopy compared to epifluoresence methods lies in the need to access the sample from two orthogonal axis. This is a severe constraint when dealing with large organs such as mammalian brain (Engelbrecht et al., 2010), which may explain why this method has not yet received a lot of attention from neurophysiologists. The only functional imaging experiments using SPIM that have been reported so far were performed on excised mice's vomeronasal organs (Holekamp et al., 2008; Turaga and Holy, 2012). Although the effective penetration depth was quite modest (of the order of 150 μm), this experiment did prove to produce simultaneous recordings of an unprecedented number of neurons with single-cell resolution.

Zebrafish is an ideal candidate for the use of SPIM-based *in vivo* functional imaging. At the larval stage, its brain is transparent and relatively small (typically $200 \times 500 \times 1000\,\mu$m) which makes it fully amenable for PSM-based calcium imaging (Higashijima et al., 2003; Niell and Smith, 2005; Ramdya and Engert, 2008; Sumbre et al., 2008; McLean and Fetcho, 2009; Del Bene et al., 2010; Aizenberg and Schuman, 2011; Ahrens et al., 2012). Here we demonstrate that SPIM can be used as an alternative optical method for functional imaging in zebrafish, as it also provides single- or near single-cell resolution of a very large fraction of the brain volume of larvae aged 5–9 dpf. We show that this technique further yields a $\simeq$20-fold increase in acquisition speed (number of recorded neurons times acquisition rate) compared to point-scanning techniques without compromising the signal-to-noise ratio (SNR). We illustrate the potential of this approach by using the extended FOV provided by the SPIM technique to identify multiple brain regions exhibiting correlated spontaneous activity, and thus likely to participate in common neural processes. Since zebrafish larvae's brains are relatively small and compact (almost no extra-cellular space), we show that the *simultaneous* recording of the whole brain activity at several Hertz with single-cell resolution is within reach.

MATERIALS AND METHODS

GENERATION OF TRANSGENIC FISH

The tol2 HuC:GCaMP3 vector was built by successive ligations of a 3.2 kb fragment of the zebrafish HuC (elav3) promoter (gift from HC Park, Kyungpook National University, Korea. Park et al., 2000), then GCaMP3 calcium probe (gift from L. Looger, Howard Hughes Medical Institute, Ashburn, Virginia, USA Tian et al., 2012) into pT2KXIG in (from K. Kawakami, National Institute of Genetics, Shizuoka, Japan). HuC promoter drives the expression of a RNA-binding protein and has been involved in neuronal differentiation. In zebrafish, the 3.2 kb proximal region encompassing 2771 base pairs of the 5′-upstream sequence up to the translation start site in +383/+385, has been shown to be sufficient to target specifically and efficiently all differentiated neurons (Park et al., 2000).

One cell stage Nacre zebrafish embryos (Lister et al., 1999) (mitfa−/−) were injected with 20 ng of the plasmid DNA and 25 ng of transposase RNA (generated from pCS-TP plasmid, K. Kawakami). Injected embryos were raised to adulthood and crossed individually with Nacre fish to obtain F1 embryos. These embryos were then screened and selected according to their level of transgene expression. The embryos with the strongest expression were raised to adulthood and incrossed to obtain the homozygous HuC:GCaMP3^{GS5} line. The HuC:GCaMP3^{GS5} embryos were collected and raised at 28.5°C in E3 embryo medium. The larvae were kept under 14/10 h on/off light cycles and fed after 6 dpf. All experiments were approved by *Le Comité d'Éthique pour l'Expérimentation Animale Charles Darwin* (Ce5/2009/027).

LARVAE PREPARATION

Zebrafish larvae aged 5–9 dpf were embedded in a low-melting-temperature agarose solution at a concentration of 1.8% in embryo medium. In order to minimize movement artifacts, the solution contained 0.3 mg/ml of Pancuronium bromide, a paralyzing agent. The fish was introduced into a glass capillary tube of internal diameter 1.5 mm. The tube was then inserted inside a PMMA square chamber filled with embryo medium and the fish was partially extruded using a piece of plastic tubing inserted in the capillary tube (**Figure 1C**). Both sides of the specimen chamber along the illumination path consisted of glass coverslips. The larva dorsoventral axis was aligned vertically by rotation of the agarose cylinder. The chamber was then positioned in the SPIM set-up on a 3-axis manual positioning stage. A piezo-positioner (piezosystem jena PZ 400 OEM) further allowed sub-micrometric vertical displacement of the chamber.

OPTICAL SET-UP

The light sheet was obtained by rapidly scanning a focused laser beam through the specimen (**Figure 1A**). A 488 nm Coherent Sapphire laser beam of power 2 mW and $1/e^2$ diameter of 0.7 mm was projected onto a galvanometric scanning mirror (Century Sunny TSH8203) driven sinusoidally at 200–400 Hz over an angular range of 9°. A scanning lens (30 mm focal length—Thorlabs AC254-030-A), placed in front of the scanning mirror, transformed the angular deflection into a horizontal displacement of the incident light. The beam was then refocused by a tube lens (200 mm focal length - Thorlabs AC508-200-A) onto the entrance pupil of a low-NA (0.16) 5x objective lens (Zeiss EC Plan-Neofluar) facing the specimen chamber. The association of the scanning and the tube lenses extended the beam to a diameter of 4.6 mm at the entrance of the illumination objective. This optical configuration yielded a 2 mm-wide illumination sheet. Its thickness profile was characterized by imaging 100 nm in diameter fluorescent beads embedded in an agarose gel cylinder as

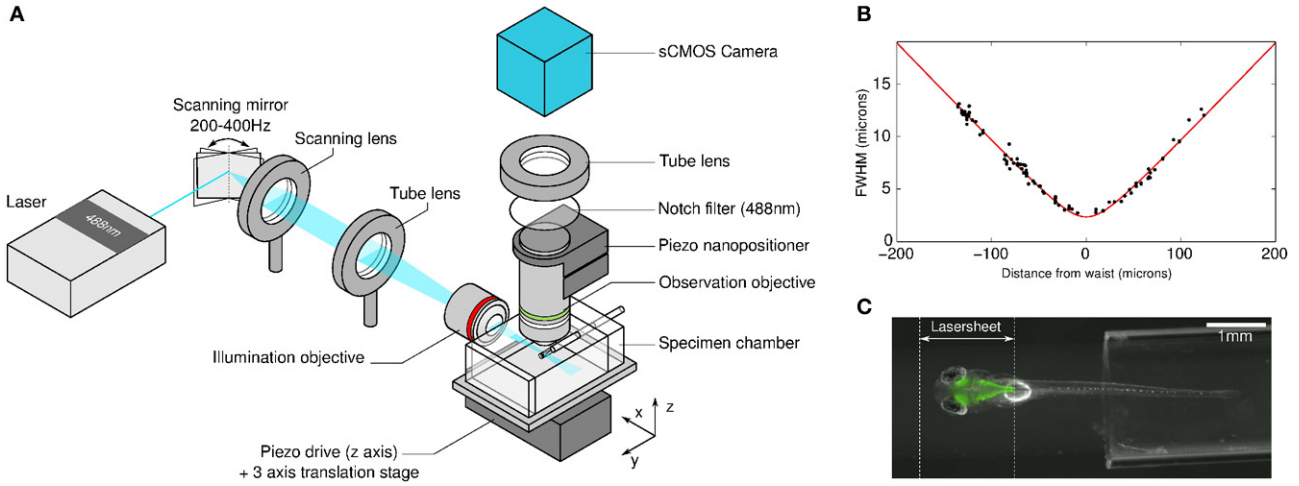

FIGURE 1 | SPIM-based functional imaging. (A) Sketch of the optical set-up. **(B)** Laser sheet thickness profile (FWHM) along the light propagation axis. Each data point corresponds to a measurement obtained with one fluorescent bead. The red curve is the best fit of the data with the theoretical profile of a Gaussian focused beam (see Truong et al., 2011) from which the value of the waist's FWHM = 2.3 μm is deduced. **(C)** Low magnification image of the larva embedded in the agarose gel cylinder and illuminated by the light sheet.

they were scanned vertically across the laser sheet. The recorded intensity signal of each bead exhibited a Gaussian profile from which the local laser-sheet full width at half maximum (FWHM) was extracted. The sheet profile was found invariant along the scanning direction, as shown by the small dispersion obtained when plotting the measured FWHM values against the beads' distance to the waist (**Figure 1B**). The profile along the propagation axis was found consistent with that expected for a Gaussian beam.

The detection objective consisted of a high-NA (1.0) 20x water-immersion objective (Olympus XLUM-PLFLN) mounted vertically onto a piezo nanopositioner (piezosystem jena MIPOS 500), allowing precise adjustment of the focus plane with the light sheet. The fluorescence light was collected by a tube lens (150 mm focal length -Thorlabs AC254-150-A) and passed through a notch filter (Thorlabs NF488-15) in order to eliminate 488 nm photons. The image was then formed onto a sCMOS sensor (PCOedge). Full 16-bit images (2560 × 2160 pixels) could be recorded at a maximum rate of 100 Hz directly onto RAID-0 hard drives. The 20x magnification yielded a field of view of $1 \times 0.8\,mm^2$, with a pixel area of $0.4 \times 0.4\,\mu m^2$. In standard experiments, images were recorded at 10–20 Hz for 20–60 min and then converted into 16-bit TIFF files.

3D RECORDINGS

3D recordings were obtained by sequentially imaging 5 distinct z-planes separated by a distance of 8 μm (total range of 32 μm). Every 50 ms, the specimen chamber was rapidly moved to a next position using the piezo-positioner. The sequence of the successive positions was interlaced in order to minimize the maximum step size and thus limit the acceleration imposed on the fish. The camera was asynchronously triggered 10 ms after each vertical displacement, and each frame was acquired for an exposure time of 40 ms. The 10 ms delay was necessary to allow for the agar cylinder to come to rest and prevent vibration-induced blurring of the images. At the end of the run, the frames were sorted to produce 5 separate stacks corresponding to each z-plane. Each stack was analyzed independently using the same algorithm as in single z-plane recordings.

AUTOMATIC IMAGE SEGMENTATION

A segmentation routine written in Matlab was developed in order to automatically identify the regions of interest (ROIs) corresponding to individual somata and neuropil regions (the Matlab code is provided as a Supplementary Material). The brain contour was first manually outlined on the first image. A highly contrasted image was then obtained by time-averaging the complete images stack. Small XY drifts were corrected by registering each image of the stack with respect to the first one by extracting the displacement vector that provided the maximum correlation. The typical maximum excursion measured over an experimental run was of the order of a few microns. However small, if not corrected, this drift was found to significantly blur the time-averaged image and hamper the proper identification of individual somata. The drift displacement sequence was also used to identify periods of strong motor behaviors. As they induced significant artifacts in the fluorescence signals, the corresponding time-periods were eliminated from the analysis.

The segmentation procedure consisted of several steps. First, the image was smoothed by running a Gaussian filter with a width equal to half the typical soma diameter (5 pixels). Local contrast stretching was applied at the scale of individual neurons. A watershed algorithm was implemented on the resulting smoothed gray-scale image, returning a collection of adjacent regions associated with putative individual somata (regions of neuropil of similar area were also retained for further analysis). A few regions were then automatically eliminated based on morphological constraints (retained ROIs had a total area between

40 and 400 pixels and an equivalent ellipse eccentricity less than 0.85). The program allowed further visualization of the resulting segmentation and manual elimination of incorrectly identified neurons. Typically, a few tens of regions, essentially located at the border of the brain, were manually discarded. Given the large FOV offered by the visualization technique, up to 5,000 somata were typically imaged and their individual ROI automatically detected within a single z-plane. This segmentation procedure took approximately 1 h per 10,000 frames, with a few minutes of user time.

SIGNAL EXTRACTION AND BASELINE NOISE ESTIMATION

The fluorescence time signal $F(t)$ for each neuron was extracted by evaluating the mean intensity across the pixels within each ROI, in each motion-corrected image. After subtraction of the background, estimated from the average intensity of pixels outside the brain, a baseline fluorescence signal was estimated for each neuron by the running average of the 8th percentile of the raw data in sliding windows of 30 s length (Dombeck et al., 2007). The resulting smooth curve b_{slow} locally approximated the baseline level and reflected slow fluctuations unrelated to the fast calcium transients evoked by spiking activity. The relative variation of fluorescence intensity, dF/F, was calculated as $dF/F = (F(t) - b_{slow})/b_{slow}$.

The standard deviation σ_{noise} of each neuron's baseline fluctuations was extracted from the distribution of neuronal dF/F values. These distributions are skewed toward positive values reflecting the presence of activity-evoked positive transients in the fluorescence signal. In contrast, negative data points are unlikely to be related to neuronal firing. The standard deviation of the baseline noise was thus estimated by postulating that these negative fluctuations were part of a Gaussian stochastic process. Consistently, the corresponding region of the distribution could be accurately fitted with a Gaussian function ($r^2 = 0.997 \pm 0.002$ for a representative dataset) from which the standard deviation σ_{noise} was extracted for each neuron's fluorescence time-series.

2P-PSM EXPERIMENTS

In order to provide a comparison between SPIM and 2P-PSM approaches, neural recordings of spontaneous activity in the tectum were performed on similar GCaMP3-expressing larvae using a MOM-sutter system. Its main components consisted of a 25x NA1.05 Olympus objective and a Mai Tai DeepSee Ti:sapphire laser used at 920 nm with an output power of less than 3 mW after the objective. The filters consisted of a FF705 dichroic, a AFF01-680 short path (IR Blocker) and a FF01520/70 band-pass filter, all from Semrock. The PMT was a H1070 (GaAsP) from Hamamatsu. Images of 256 x 256 pixels were acquired at 4 Hz.

ANALYSIS OF NEURONAL ACTIVITY CORRELATIONS

For this analysis, we only considered fluorescence transients inferred to result from neuronal firing by imposing a threshold on each individual time-series. Any dF/F value below $3\,\sigma_{noise}$ was set to 0. For each dataset, 100 independent runs of the K-means algorithm with squared Euclidean distance and random seeds were performed (MacQueen, 1967). Only the run with minimal total sum of distances was retained. In order to determine the total number K of clusters in the segmentation, a sweep in K space between 1 and 20 was performed, and the results were inspected with silhouette plots. For example, when analyzing the data displayed in **Figure 5**, $K = 12$ was found to be the best solution. Importantly, the neuronal clusters shown in this figure, which are the most compact, proved robust with respect to changes in K between 10 and 20.

RESULTS

Our main objective was to establish the advantages and limitations of SPIM for *in-vivo* functional imaging in zebrafish. Spontaneous activity was recorded in 5–9-day-old HuC:GCaMP3 zebrafish larvae. First, we characterized the volume of the brain accessible to single-cell calcium imaging using SPIM. Second, we estimated the gain in the number of neurons that could be simultaneously sampled, and in the maximum accessible acquisition rate, that this imaging strategy provides compared to standard 2P-PSM experiments. Finally, we showed how the extended FOV provided by SPIM allows one to probe correlations in spontaneous activity among multiple brain regions as an indication of inter-regional brain connectivity.

OPTICAL SECTIONING EFFICIENCY OF THE SPIM SET-UP

In SPIM, the efficiency of the optical sectioning is set by the thickness of the illumination sheet. As expected for scanned illumination with a Gaussian beam, the laser sheet profile was found to be invariant along the scanning axis and to display a hyperbolic profile along the light propagation axis, with a diffraction-limited minimum thickness of 2.3 μm located at the focal plane of the illumination objective (see **Figure 1B**). This value was found to increase to 7 μm at a distance of 80 μm from the waist. Given the characteristic inter-neuron distance (of the order of 7 μm), the method thus yields single neuron resolution over a FOV of $\simeq 160 \times 1000\,\mu m$ around the midline of the larva, a region which contains the majority of the somata. In the most distal regions of the zebrafish brain, the illumination sheet spans 1–2 neuron diameter such that SPIM does not provide single-cell resolution.

Despite this limited axial resolution, the images appeared highly contrasted in most of the brain volume, allowing for the implementation of an automatic segmentation algorithm in order to identify ROIs associated with each neuron. This aspect of the method is illustrated in **Figure 2**. Images were taken at successive z-positions with 0.4 μm intervals across the brain over a total vertical distance of 220 μm (see Supplementary Movie 1). The exposure time was set to 100 ms such that the complete stack was acquired in less than 1 min. We were able to automatically identify virtually all the somata throughout the brain volume except for small telencephalic regions located in the shadow of the eye and in the neuropil regions.

The robustness of the automatic segmentation procedure is illustrated in **Figure 2B** for different brain areas at a depth of 104 μm, which corresponded to the middle of the preceding stack. The segmentation was performed on the image obtained by time-averaging 18, 000 frames acquired at 10 Hz over 30 min, which corresponds to a typical neural recording configuration. The possibility to automatically identify somata's ROIs is a crucial

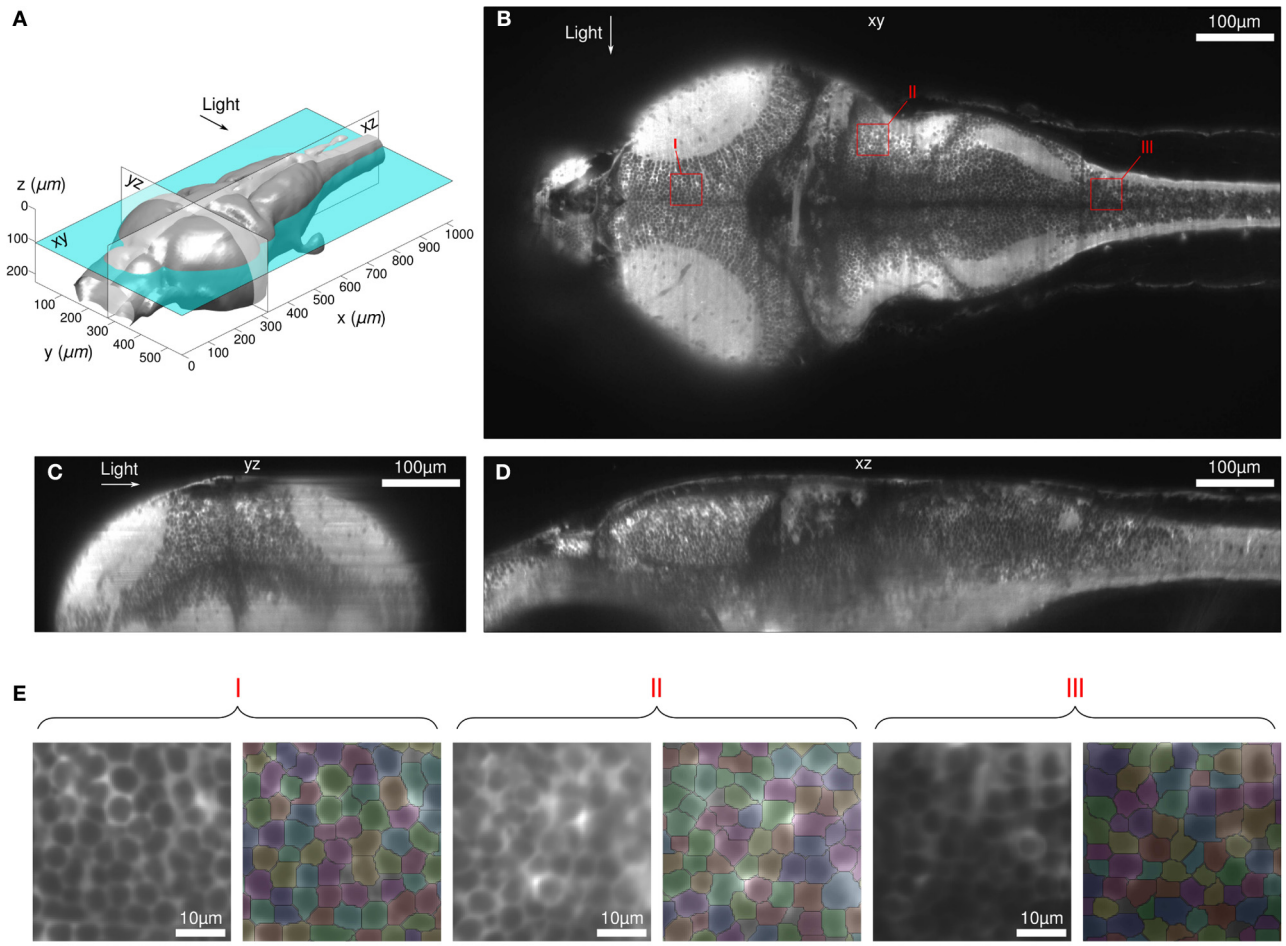

FIGURE 2 | Stack and segmentation. (A–D) Multi-view sections of the brain-volume reconstructed from a complete 3D stack (no filtering). The voxel volume is $0.4 \times 0.4 \times 0.4\,\mu m^3$. See Supplementary Movie 1 for a complete visualization of the brain. **(E)** Result of the segmentation algorithm for 3 different sub-regions shown in **(B)** with red-squares.

aspect of the present approach, since the manual outlining of ≃5,000 neurons per plane would otherwise impose a severe practical limit on the method.

One should be aware that the light sheet thickness measurement described in Materials and Methods provides an upper bound for the axial resolution in the actual experiment. When imaging the brain volume, the scattering of the illumination beam tends to reduce the effective axial resolution. Similarly, the x-y resolution is expected to be degraded by the scattering of the fluorescence photons. The magnitude of these effects was estimated by computing the cellular-scale contrast, defined as the difference in intensity between the brightest and dimmest pixels (second and 98th percentile) over areas slightly larger than the somata characteristic ROIs. As anticipated, the contrast was found to be maximum in the most dorsal region of the fish, where the distances traveled by the illumination and fluorescent photons were both minimum. The contrast then decreased continuously with the depth of observation, but with a moderate decay rate of $40 \pm 5\%$ per $100\,\mu m$.

FAST, BRAIN-WIDE CALCIUM IMAGING

Images of a single z-plane were acquired at 10–20 Hz (50–100 ms exposure time) over periods of 20–60 min (a short excerpt of a 10 Hz recording is provided in supplementary Movie 2). In the majority of the experiments, the plane of observation was chosen to encompass a large number of neurons from all major brain regions (spinal cord, hindbrain, midbrain, and forebrain). After automatic segmentation, the relative fluorescence time series dF/F was extracted for each individual soma and for neuropil regions of similar area (**Figure 3**).

As no external stimulation was applied, the recorded fluorescence dynamics reflected spontaneous neural activity. Strictly speaking, the illumination wavelength (488 nm) being within the fish visual spectrum, the larva was submitted to a visual stimulation. However, owing to the rapid scanning rate (>200 Hz), such a stimulation can be considered physiologically time-invariant and the fish is expected to habituate rapidly. Consistently, we did not observe any systematic change in the level of neural activity over the duration of the experiments. This was

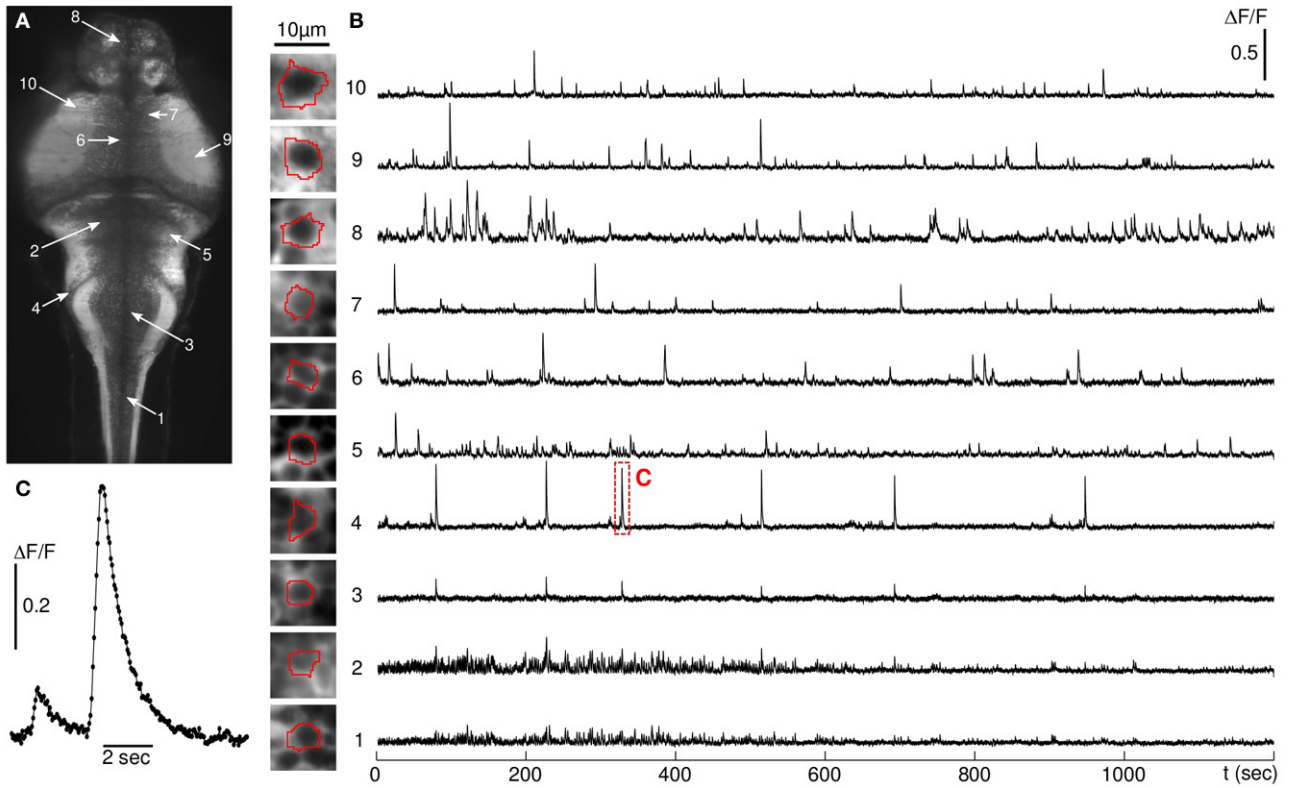

FIGURE 3 | Fluorescence signals. (A) Time-averaged image of a brain slice of a 6 dpf larva. **(B)** Individual traces of 10 neurons whose locations are indicated in red on the image, recorded at 20 Hz acquisition rate. the thumbnails display each neuron's ROI. **(C)** Blow-up view of a typical activity-related fluorescence event indicated by a red rectangle in **(B)**.

checked by computing the mean of the activity-related transients in the first and second half of the runs. The difference between both measurements was not found to be statistically significant.

In all runs, the laser intensity was set to 2 mW. At this power, the fluorescence baseline did not display any noticeable decay over the duration of the experimental runs, which indicated the absence of significant photo-bleaching. Furthermore, as already mentioned, the level of activity showed no systematic change. Both observations provided a solid indication that phototoxicity effects should be rather limited at this level of illumination. At 6 mW, although the level of photo-bleaching was still relatively modest (≈10% baseline intensity decay in 20 min), the activity-related signal from somata in all regions of the brain tended to vanish. This effect was reversible, i.e. the original fluorescence transient level could be recovered by setting the power back to 2 mW. The most plausible interpretation of this set of observations is that before phototoxicity effects become significant, the calcium-bound fluorophores, which have a much higher quantum yield that the unbound species, reached their photo-emission saturation rate resulting in a significant reduction in amplitude of the fluorescence transients.

In some experiments, streaking artifacts were observed in the form of rapid correlated fluctuations of intensity along narrow bands oriented parallel to the illumination axis. These flickering regions resulted from the motion of light absorbing objects (probably the hemoglobin within blood cells) circulating along the exposed face of the animal. As they crossed the light sheet, they projected a thin shadow along the illumination path. When too intense, these fluctuations biased the analysis of the fluorescence signals, so that the corresponding neurons had to be manually eliminated from the analysis.

THREE-DIMENSIONAL CALCIUM-IMAGING

The high data throughput provided by SPIM can be used to obtain dynamic 3D brain-wide recordings of neural activity at a lower acquisition rate. As a proof of concept, we recorded 5 different z-planes, separated by 8 μm, a distance which guaranteed that neurons from different slices were distinct. Axial scanning was obtained by sequentially moving the specimen at the successive z-positions (**Figure 4A**). This approach allowed for the simultaneous recording of over 25,000 individual neurons (and large neuropil regions) at 4 Hz. **Figures 4B,C** shows the location of the centers of mass of the sampled ROIs and the associated dF/F traces for a few neurons, located in different regions of the brain.

EVALUATING THE SIGNAL-TO-NOISE RATIO (SNR)

In order to evaluate the sensitivity of the method, a statistical comparison was made between spontaneous activity recordings

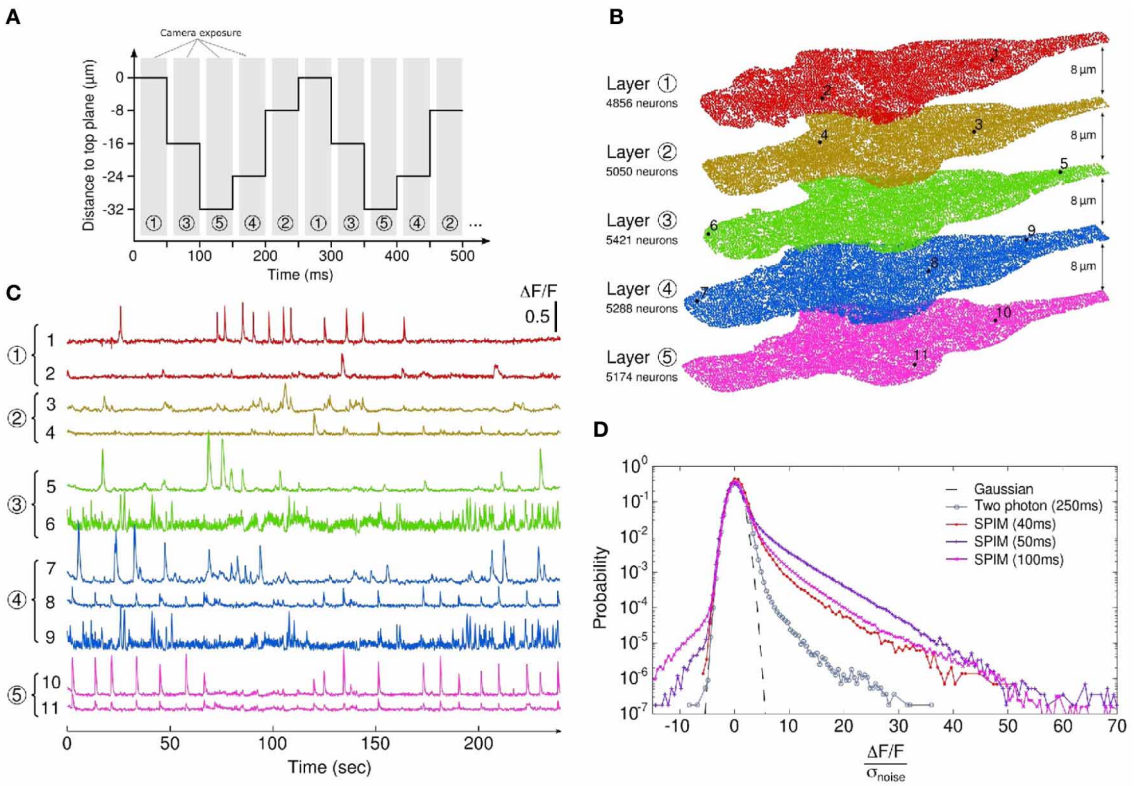

FIGURE 4 | 3D calcium-imaging. (A) Interlaced sequence of acquisition of 5 z-planes separated by 8 µm intervals. Exposure time is 40 ms and each plane is recorded at a rate of 4 Hz. **(B)** Localization of the monitored ROIs (somas and neuropil regions) obtained through automatic segmentation on the 5 different planes. The number of actual somas is given for each z-plane, yielding a total of 25789 simultaneously recorded neurons (see Supplementary Movie 3 for the 5 z-frames fluorescence dynamics). **(C)** Characteristic signals from neurons within the stack. **(D)** Comparison of the noise-normalized fluorescence signal distributions for SPIM-based experiments (colored) and a 2P-PSM experiment (gray). For each experiment, the exposure time is indicated. The 40 ms-exposure SPIM experiment is the 3D imaging run (5 z-planes, 4 Hz effective recording rate).

obtained using SPIM and 2P-PSM in the tectal region under comparable experimental conditions (see Materials and Methods, all statistics were computed from three independent runs for each set-up). At 10 Hz acquisition rate, the standard deviation σ_{noise} of the baseline fluorescence signal (extracted for each neuron, see Materials and Methods) using SPIM was found to be of order 1% ($\sigma_{noise} = 0.008 \pm 0.002$). This quantity was measured at 0.13 ± 0.04 in 2P-PSM at 4 Hz acquisition rate. The relatively low noise level observed in SPIM is a consequence of the larger photon count provided by the method. A significant fraction of these photons, however, originates from regions outside the in-focus ROIs, owing to the less efficient sectioning and the wide-field nature of this optical method. This in turn increases the background signal, thus limiting the amplitude of the dF/F transients. For comparable configurations, 2P-PSM recordings actually displayed statistically higher dF/F peak signals: the average of the dF/F values within the highest percentile was found to be 0.11 and 0.55 in SPIM and 2P-PSM, respectively.

To provide a fair SNR comparison between both methods, each neuronal dF/F distribution was thus normalized by its baseline noise standard deviation σ_{noise}. The resulting noise-normalized fluorescence distributions are shown in **Figure 4D** for three experimental SPIM runs (single z-plane recordings at acquisition rates 10 and 20 Hz, 5 z-planes 3D recording at 4 Hz) and for a typical run performed at 4 Hz using 2P-PSM. Although the SPIM experiments used lower exposure times (40–100 ms instead of 250 ms), the corresponding distributions appeared to be more significantly skewed toward large positive values as compared to 2P-PSM, which indicated that the SNR was improved. Across all experiments, the skewness of the noise-normalized distribution was found to be 3.70 ± 0.78 in SPIM as compared to 0.54 ± 0.11 in 2P-PSM. Although this difference is statistically significant, one should consider such a determination of the relative SNR as a rough estimate since the level of spontaneous activity in the tectum may vary significantly between runs.

IDENTIFYING BRAIN-WIDE HIGHLY CORRELATED NEURONAL CLUSTERS

One of the important assets of the SPIM method, with respect to PSM approaches, lies in the possibility of simultaneously recording neural activity in distinct brain regions. This in turn enables the identification of ensembles of neurons spanning

different regions of the brain that exhibit correlated activity and are thus likely to be interconnected or activated by a common source. Here we illustrate this possibility by using a 60 min long single plane recording of multiple brain regions at 10 Hz acquisition rate. The fluorescence time-series of each neuron was first thresholded in order to extract activity-related events (see Materials and Methods). The rest of the data points was set to zero. This thresholding was necessary to eliminate coherent baseline noise, induced by minute laser intensity fluctuations, which would have otherwise biased the correlation analysis.

The distribution of pair-wise correlations showed a heavy-tail of fairly large values, suggesting the presence of significantly correlated activity (**Figure 5A**). As a first attempt to identify the optimal clustering of the neural activity time-series, the K-means algorithm was implemented (see Materials and Methods). An example of the computed partitionings is shown in **Figure 5B**, where a reasonable clusterization of highly correlated neuronal groups with moderate cross-talk can be observed. Three of these clusters topographical layouts are shown in **Figures 5C–G**, together with excerpts of (unfiltered) fluorescence traces of 3 neurons within each cluster.

The first cluster revealed significant correlations among neighboring neurons in the optic tectum (**Figure 5C**). Notice that the mean pair-wise correlation was found to continuously decay from a confined region located at the border of the neuropil. The second cluster consisted of neurons mostly located in the spinal cord (**Figure 5E**). In the first 10 min of the run, these neurons exhibited characteristic rhythmic synchronous activity at a typical frequency of 0.2 Hz (see **Figure 5F**). In the paralyzed preparation, these bouts of spinal cord activity are likely to be associated with fictive swimming events. The large FOV allowed us to further identify a sub-population of distant neurons located in two bilaterally symmetric confined regions, which probably correspond to the medial octavolateralis nucleus. A similar cluster of correlated neurons was observed in another animal exhibiting fictive swimming. Finally, stripes of neurons located in the vagal lobe, a brain structure implicated in the processing of gustatory stimuli, were found to be correlated with distant bilaterally symmetric neuronal clusters probably located at the secondary gustatory nuclei (SGN), in the isthmus ventrally to the cerebellum (**Figure 5G**). It should be noticed that these three functional clusters, associated with three distinct modalities (visual, motor, and gustatory), were identified from a single 60 min long recording of a single z-plane.

DISCUSSION

In PSM-based calcium-imaging, neurons are probed sequentially, which imposes a trade-off between the number of sampled neurons N_{cells} and the acquisition rate f_{acq} (Lütcke and Helmchen, 2011). In order to increase the maximum of the product $N_{\text{cells}}f_{\text{acq}}$, AOM-based random scanning approaches have been developed, which aimed at minimizing the time wasted in acquiring regions outside the neurons volume. Notice that this issue is almost irrelevant in zebrafish, since most of the brain consists of tightly packed somata (almost no extra-cellular space). A fundamental limit in data throughput is, however, set by the minimum dwelling time of the laser at each voxel required to record a significant number of photons.

Scanned laser sheet imaging also relies on sequential recording of neurons, but those within a given line are illuminated and recorded in parallel. As established in the present experiment, this yields a $\simeq 20-$fold increase in the accessible $N_{\text{cells}}f_{\text{acq}}$ product for similar experimental conditions. Hence, while current PSM-based calcium-imaging set-ups in zebrafish allow monitoring $\simeq$1000 neurons at 5 Hz, SPIM allows monitoring up to 5,000 neurons from a single z-plane at 20 Hz, and over 25,000 neurons from 5 different z-planes at 4 Hz, with similar or better SNR. This large increase in data throughput offered by SPIM-based calcium imaging opens new opportunities for studying various aspects of neural processes.

TOWARD *in toto* DYNAMIC NEURAL RECORDING OF A VERTEBRATE BRAIN

Larval zebrafish constitutes a unique vertebrate system to study the activity of brain-wide neural circuits and help decipher the way information is processed across different brain regions. This possibility was illustrated in a recent paper by Ahrens et al. (2012). By recording calcium activity in an animal that interacted fictively with a virtual environment, the authors were able to identify neural populations spanning multiple brain areas that were activated during specific phases of adaptive locomotion. Owing to the limited number of neurons sampled during a single recording, different experiments and animals had to be fused in order to produce a complete physiological map of the associated neural networks. This approach was not only time-consuming but also implicitly assumed that the recruited neuronal population was invariant from run to run and animal to animal. In order to overcome these limitations, one would need to *simultaneously* record the complete brain. This would allow for the gathering of similar data on a single-trial basis, and thus permit one to probe the variability in the spatial pattern of the recruited neural population.

In its current configuration, our SPIM set-up allows one to simultaneously sample $\simeq$30% of the total number of neurons (Hill et al., 2003) at 4 Hz. Given the decay time of GCaMP3 (of the order of 0.5 s), this acquisition rate guarantees that any calcium transient for a given neuron within this volume is detected. This result was shown as a proof-of-concept and further refinements are needed. In particular, axial scanning was obtained by continuously moving the sample across the light-sheet. This approach presents two major drawbacks. First, it submits the larva to an oscillatory acceleration of maximum amplitude of order $0.1\,\text{ms}^{-2} = 10^{-2}\,\text{g}$ where g is the gravitational acceleration. Although relatively low, this inertial stimulation may trigger responses from the fish's vestibular system. Second, the softness of the agar gel limits the rate at which successive z-positions can be imaged, since a significant time is needed for the cylinder to come to rest. Both issues could be addressed by maintaining the specimen fixed while synchronously moving the laser sheet (using a second galvanometric mirror) and the observation objective. Higher z-scanning rates could also be obtained by using tunable optical components (Grewe et al., 2011). Given the constant progress in GECI sensitivity (Akerboom et al., 2012) and sCMOS

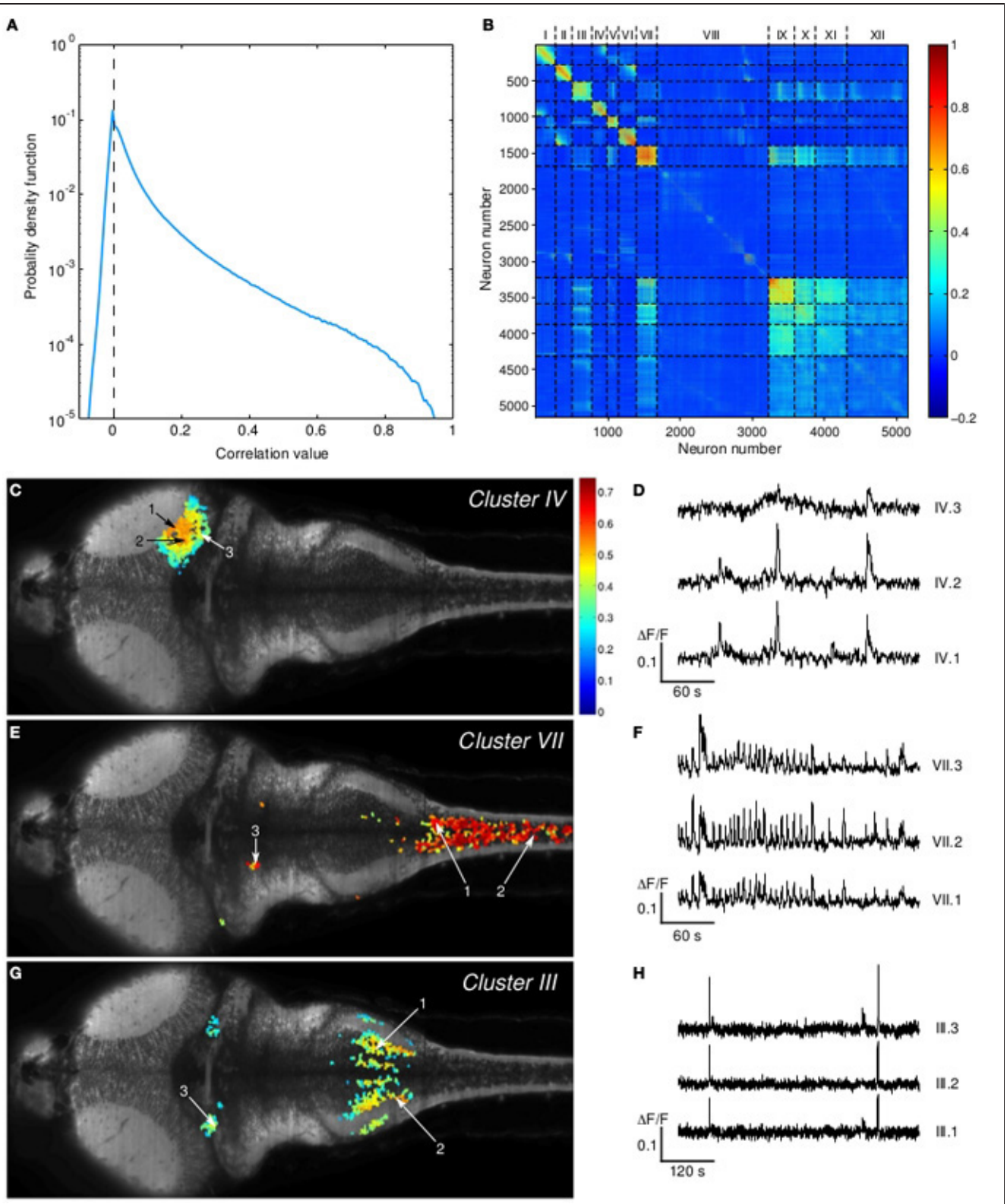

FIGURE 5 | Activity-correlated neuronal clusters. (A) Distribution of pair-wise correlations. The data were obtained from a 10 Hz, 60 min long experiment on a 6 dpf larva. **(B)** Correlation matrix sorted using the K-means algorithm with associated cluster partitioning. **(C–G)** Topographical layouts of clusters IV-VII-III. The color code corresponds to the mean pair-wise correlation value with the neurons from the cluster. For each cluster, 3 short excerpts of fluorescence traces exhibiting clear activity correlation are shown **(D–H)**.

sensors, SPIM-based calcium imaging should provide virtually full brain simultaneous recording at several Hertz in the near future.

PROBING THE TIME-STRUCTURE OF BRAIN-WIDE NEURAL ACTIVITY PATTERNS

Calcium-imaging was originally seen as a way to overcome the limitation in the number of neurons that could be recorded using electrophysiological approaches. For a long time, it was believed that an inevitable corollary of this method was to sacrifice temporal information as the calcium signals were typically probed at a few Hertz, far below physiological timescales. In recent years, several fast imaging experiments proved this assumption wrong. Recently, Grewe *et al.* demonstrated a $\simeq$10 ms resolution on the firing dynamics of individual neurons based on calcium-imaging performed at hundreds of Hertz (Grewe et al., 2010). This time-resolution was actually set by the intrinsic dynamics of the fluorescent calcium indicator (Oregon Green BAPTA-1). This achievement demonstrated that calcium-imaging could constitute a suitable method for probing neural networks dynamics with near-millisecond resolution, and thus could serve to explore how spike-timing may play a role in neural processes. However, this exciting result was obtained at the cost of the number of probed neurons, of the order of a few tens *i.e.* close to that currently recorded using silicon-based nanoprobes. Fast *in vivo* neural recordings are thus currently restricted to spatially confined micro-circuits. In contrast, SPIM should allow reaching high acquisition rates while still probing a large number of neurons. In the present experiments, the acquisition rate was limited to 20 Hz since the relatively slow GCaMP3 rising time (of the order of 100 ms) sets the bandwidth within which spiking dynamics can be efficiently probed. Increasing the acquisition rate would only degrade SNR without enhancing the time-resolution. With sufficiently rapid and sensitive calcium reporters—such as the synthetic sensors used by Grewe et al. (2010)—it should be possible to record up to 1000 neurons with near-millisecond resolution.

Several limitations of this method still need to be addressed. First, the optical sectioning only guarantees single-cell resolution in the most proximal part of the brain. Different methods could be implemented to increase the axial resolution, such as structured illumination (Keller et al., 2010) or confocal light-sheet imaging (Silvestri et al., 2012). A second issue is related to the use of visible light illumination (488 nm), which currently hampers the proper stimulation of the fish visual system. This limitation could be circumvented by using two photon fluorescence excitation with the same SPIM geometry (Palero et al., 2010; Truong et al., 2011). This would in turn opens the possibility to implement Bessel-beam illumination. Beyond the expected gain in optical sectioning efficiency provided by this method (Planchon et al., 2011), the self-healing property of Bessel beams may permit to mitigate the problems of streaking.

In the present article, we have demonstrated how the extended FOV provided by this alternative imaging strategy allows one to identify brain-wide functional neuronal circuits by straightforward correlation analysis of the spontaneous activity pattern. Overall, the combination of SPIM-based functional imaging, transgenic larvae and methods for statistical data analysis will lead to the generation of a whole brain atlas of functional neuronal connectivity, either by monitoring spontaneous or sensory-evoked activity, or through localized channelrhodopsin-2 stimulation.

ACKNOWLEDGMENTS

We are grateful to Laurent Bourdieu and Jean-François Leger for constant support and numerous advices throughout the assembly of the SPIM set-up. This work was supported in part by EraSysBio+ ZeBrain and ERC stg 243106.

SUPPLEMENTARY MATERIAL

The Supplementary Material for this article can be found online at: http://www.frontiersin.org/Neural_Circuits/10.3389/fncir.2013.00065/abstract

REFERENCES

Ahrens, M. B., Li, J. M., Orger, M. B., Robson, D. N., Schier, A. F., Engert, F., et al. (2012). Brain-wide neuronal dynamics during motor adaptation in zebrafish. *Nature* 485, 471–477.

Aizenberg, M., and Schuman, E. M. (2011). Cerebellar-dependent learning in larval zebrafish. *J. Neurosci.* 31, 8708–8712.

Akerboom, J., Chen, T.-W., Wardill, T. J., Tian, L., Marvin, J. S., Mutlu, S., et al. (2012). Optimization of a GCaMP calcium indicator for neural activity imaging. *J. Neurosci.* 32, 13819–13840.

Alivisatos, A., Chun, M., Church, G. M., Greenspan, R. J., Roukes, M. L., and Yuste, R. (2012). The brain activity map project and the challenge of functional connectomics. *Neuron* 74, 970–974.

Bollmann, J. H., and Engert, F. (2009). Subcellular topography of visually driven dendritic activity in the vertebrate visual system. *Neuron* 61, 895–905.

Del Bene, F., Wyart, C., Robles, E., Tran, A., Looger, L., Scott, E. K., et al. (2010). Filtering of visual information in the tectum by an identified neural circuit. *Science* 330, 669–673.

Denk, W., Strickler, J., and Webb, W. (1990). Two-photon laser scanning fluorescence microscopy. *Science* 248, 73–76.

Dombeck, D. A., Khabbaz, A. N., Collman, F., Adelman, T. L., and Tank, D. W. (2007). Imaging large-scale neural activity with cellular resolution in awake, mobile mice. *Neuron* 56, 43–57.

Du, J., Blanche, T. J., Harrison, R. R., Lester, H. A., and Masmanidis, S. C. (2011). Multiplexed, high density electrophysiology with nanofabricated neural probes. *PLoS ONE* 6:e26204. doi: 10.1371/journal.pone.0026204

Engelbrecht, C. J., Voigt, F., and Helmchen, F. (2010). Miniaturized selective plane illumination microscopy for high-contrast *in vivo* fluorescence imaging. *Opt. Lett.* 35, 1413–1415.

Grewe, B. F., Langer, D., Kasper, H., Kampa, B. M., and Helmchen, F. (2010). High-speed *in vivo* calcium imaging reveals neuronal network activity with near-millisecond precision. *Nat. Methods* 7, 399–405.

Grewe, B. F., Voigt, F. F., van't Hoff, M., and Helmchen, F. (2011). Fast two-layer two-photon imaging of neuronal cell populations using an electrically tunable lens. *Biomed. Opt. Express* 2, 2035–2046.

Grienberger, C., and Konnerth, A. (2012). Imaging calcium in neurons. *Neuron* 73, 862–885.

Higashijima, S.-I., Masino, M. A., Mandel, G., and Fetcho, J. R. (2003). Imaging neuronal activity during zebrafish behavior with a genetically encoded calcium indicator. *J. Neurophysiol.* 90, 3986–3997.

Hill, A., Howard, C. V., Strahle, U., and Cossins, A. (2003). Neurodevelopmental defects in zebrafish (*Danio rerio*) at environmentally relevant dioxin (TCDD) concentrations. *Toxicol. Sci.* 76, 392–399.

Holekamp, T. F., Turaga, D., and Holy, T. E. (2008). Fast three-dimensional fluorescence imaging of activity in neural populations by objective-coupled planar illumination microscopy. *Neuron* 57, 661–672.

Huisken, J., Swoger, J., Del Bene, F., Wittbrodt, J., and Stelzer, E. H. K. (2004). Optical sectioning deep inside live embryos by selective plane illumination microscopy. *Science* 305, 1007–1009.

Katona, G., Szalay, G., Maak, P., Kaszas, A., Veress, M., Hillier, D., et al. (2012). Fast two-photon *in vivo* imaging with three-dimensional random-access scanning in large tissue volumes. *Nat. Methods* 9, 201–208.

Keller, P. J., and Dodt, H.-U. (2012). Light sheet microscopy of living or cleared specimens. *Curr. Opin. Neurobiol.* 22, 138–143.

Keller, P. J., Schmidt, A. D., Santella, A., Khairy, K., Bao, Z., Wittbrodt, J., et al. (2010). Fast, high-contrast imaging of animal development with scanned light sheet-based structured-illumination microscopy. *Nat. Methods* 7, 637–642.

Lillis, K. P., Eng, A., White, J. A., and Mertz, J. (2008). Two-photon imaging of spatially extended neuronal network dynamics with high temporal resolution. *J. Neurosci. Methods* 172, 178–184.

Lister, J. A., Robertson, C. P., Lepage, T., Johnson, S. L., and Raible, D. W. (1999). Nacre encodes a zebrafish microphthalmia-related protein that regulates neural-crest-derived pigment cell fate. *Development* 126, 3757–3767.

Lütcke, H., and Helmchen, F. (2011). Two-photon imaging and analysis of neural network dynamics. *Rep. Prog. Phys.* 74:086602. doi: 10.1088/0034-4885/74/8/086602

MacQueen, J. (1967). "Some methods for classification and analysis of multivariate observations," in *Proceedings of 5-th Berkeley Symposium on Mathematical Statistics and Probability,* Vol. 1, (Berkeley, CA: University of California Press), 281–297.

McLean, D. L., and Fetcho, J. R. (2009). Spinal interneurons differentiate sequentially from those driving the fastest swimming movements in larval zebrafish to those driving the slowest ones. *J. Neurosci.* 29, 13566–13577.

Mertz, J. (2011). Optical sectioning microscopy with planar or structured illumination. *Nat. Methods* 8, 811–819.

Niell, C. M., and Smith, S. J. (2005). Functional imaging reveals rapid development of visual response properties in the zebrafish tectum. *Neuron* 45, 941–951.

Palero, J., Santos, S. I. C. O., Artigas, D., and Loza-Alvarez, P. (2010). A simple scanless two-photon fluorescence microscope using selective plane illumination. *Opt. Express* 18, 8491–8498.

Park, H. C., Kim, C. H., Bae, Y. K., Yeo, S. Y., Kim, S. H., Hong, S. K., et al. (2000). Analysis of upstream elements in the HuC promoter leads to the establishment of transgenic zebrafish with fluorescent neurons. *Dev. Biol.* 227, 279–293.

Planchon, T. A., Gao, L., Milkie, D. E., Davidson, M. W., Galbraith, J. A., Galbraith, C. G., et al. (2011). Rapid three-dimensional isotropic imaging of living cells using Bessel beam plane illumination. *Nat. Methods* 8, 417–423.

Ramdya, P., and Engert, F. (2008). Emergence of binocular functional properties in a monocular neural circuit. *Nat. Neurosci.* 11, 1083–1090.

Salomé, R., Kremer, Y., Dieudonné, S., Léger, J.-F., Krichevsky, O., Wyart, C., et al. (2006). Ultrafast random-access scanning in two-photon microscopy using acousto-optic deflectors. *J. Neurosci. Methods* 154, 161–174.

Silvestri, L., Bria, A., Sacconi, L., Iannello, G., and Pavone, F. S. (2012). Confocal light sheet microscopy: micron-scale neuroanatomy of the entire mouse brain. *Opt. Express* 20, 20582–20598.

Stevenson, I. H., and Kording, K. P. (2011). How advances in neural recording affect data analysis. *Nat. Neurosci.* 14, 139–142.

Sumbre, G., Muto, A., Baier, H., and Poo, M.-M. (2008). Entrained rhythmic activities of neuronal ensembles as perceptual memory of time interval. *Nature* 456, 102–106.

Tian, L., Hires, S. A., and Looger, L. L. (2012). Imaging neuronal activity with genetically encoded calcium indicators. *Cold Spring Harb. Protoc.* 2012, 647–656.

Tomer, R., Khairy, K., and Keller, P. J. (2011). Shedding light on the system: studying embryonic development with light sheet microscopy. *Curr. Opin. Genet. Dev.* 21, 558–565.

Truong, T. V., Supatto, W., Koos, D. S., Choi, J. M., and Fraser, S. E. (2011). Deep and fast live imaging with two-photon scanned light-sheet microscopy. *Nat. Methods* 8, 757–760.

Turaga, D., and Holy, T. E. (2012). Organization of vomeronasal sensory coding revealed by fast volumetric calcium imaging. *J. Neurosci.* 32, 1612–1621.

Verveer, P. J., Swoger, J., Pampaloni, F., Greger, K., Marcello, M., and Stelzer, E. H. K. (2007). High-resolution three-dimensional imaging of large specimens with light sheet-based microscopy. *Nat. Methods* 4, 311–313.

Weber, M., and Huisken, J. (2011). Light sheet microscopy for real-time developmental biology. *Curr. Opin. Genet. Dev.* 21, 566–572.

Wyart, C., Del Bene, F., Warp, E., Scott, E. K., Trauner, D., Baier, H., et al. (2009). Optogenetic dissection of a behavioural module in the vertebrate spinal cord. *Nature* 461, 407–410.

Yuste, R., and Denk, W. (1995). Dendritic spines as basic functional units of neuronal integration. *Nature* 375, 682–684.

Conflict of Interest Statement: The authors declare that the research was conducted in the absence of any commercial or financial relationships that could be construed as a potential conflict of interest.

Received: 08 February 2013; accepted: 25 March 2013; published online: 09 April 2013.

Citation: Panier T, Romano SA, Olive R, Pietri T, Sumbre G, Candelier R and Debrégeas G (2013) Fast functional imaging of multiple brain regions in intact zebrafish larvae using Selective Plane Illumination Microscopy. Front. Neural Circuits 7:65. doi: 10.3389/fncir.2013.00065

2-photon ligh sheet microscopy

One of the main drawbacks of the lightsheet setup presented above is that the laser wavelength ($488\,nm$) lies in the middle of the animal's visible spectrum [30]. Even though the laser does not hit the retina, no optical setup is perfect and there are reflections at every diopter (*e.g.* lenses, objective and air/water interface) and in the sample tank which finally arrive into the eye. In addition, the zebrafish larval brain contains photosensitive cells perceiving the blue domain [31]. Finally, during 3D recordings the light sheet – and thus the reflections seen by the animal – oscillates at a frequency of a few Hertz, and can be perceived by the visual system.

As far as we know, though it still seems possible to use the $488\,nm$light sheet to study robust reflexes related to the visual system like the opto-motor reflex [32], it is a strong limitation to study finer effects. For instance, in some yet unpublished work Volker Bormuth has shown that the opto-kinetic reflex is strongly hampered, if not totally suppressed, by the simple presence of the blue laser in the brain. Somehow, the same situation is similar to what happened more than 20 years ago, when researchers willing to study the visual system without illumination bias started to use 2-photon microscopes instead of the confocal. Indeed, as the wavelength of the infrared laser stands out of the visible spectrum the animal is plunged in "visible darkness".

Given the fact that the visual system is the most developped sensory modality in $5\,dpf$zebrafish larvae and that a large fraction of the community works on vision-related topics, it sounded essential to transpose the light sheet setup to 2-photon fluorescence. In a collaboration with Emmanuel Beaurepaaire and Willy Supatto (*École Polytechnique*, LOB), we have tested the feasibility of 2-photon functional imaging in zebrafish larvae on their already existing microscope and then we developed our own at the LJP, in the framework of the Ph.D. of Sébastien Wolf.

The following article briefly presents the technique and compares the effects of visible and infrared illumination on the responses of the visual system to flashes.

Whole-brain functional imaging with two-photon light-sheet microscopy

To the Editor: Several studies recently demonstrated that one-photon (1P) light-sheet imaging gives access to the spontaneous activity of a large fraction of the zebrafish larval brain at nearly single-cell resolution[1–3]. This imaging method, however, requires an intense and extended illumination at a wavelength ($\lambda = 488$ nm) that lies within the most sensitive region of the fish visible spectrum[4] and therefore likely stimulates the blue photoreceptors in the retina as well as other photosensitive cells[5]. As an alternative, we report on brain-wide three-dimensional (3D) neural recordings during visuomotor integration in zebrafish larvae using two-photon (2P) light-sheet imaging[6] at a wavelength of 930 nm combined with visual stimulation.

The extent to which 1P illumination interferes with visually driven processes is critical as it determines the suitability of light-sheet imaging for behavioral neuroscience. Vladimirov *et al.* recently showed that the optomotor reflex and the associated motor-adaptation behavior could be normally evoked during 1P light-sheet imaging[3]. However, these robust behaviors are not driven by the blue and UV cones[7] and are not even affected by ablation of the optic tectum, the largest visual center in fish[8]. To evaluate the relevance of 2P excitation for whole-brain visual studies and directly compare 1P and 2P excitation regimes, we implemented a twin light-sheet system (**Fig. 1a**, **Supplementary Figs. 1** and **2**, and **Supplementary Table 1**). This system provided similar axial and lateral resolutions in the 1P and 2P configurations and enabled functional imaging with cellular resolution in ~80% of the brain volume (**Supplementary Figs. 3** and **4**), without measurable photobleaching during long-term (1-h) recordings. We exposed 4- to-6-d-old zebrafish larvae expressing the calcium indicator GCaMP5G to a series of blue flashes of increasing intensity. We successively recorded evoked neural activity at 4 Hz using 1P and 2P imaging in approximately the same layer of the

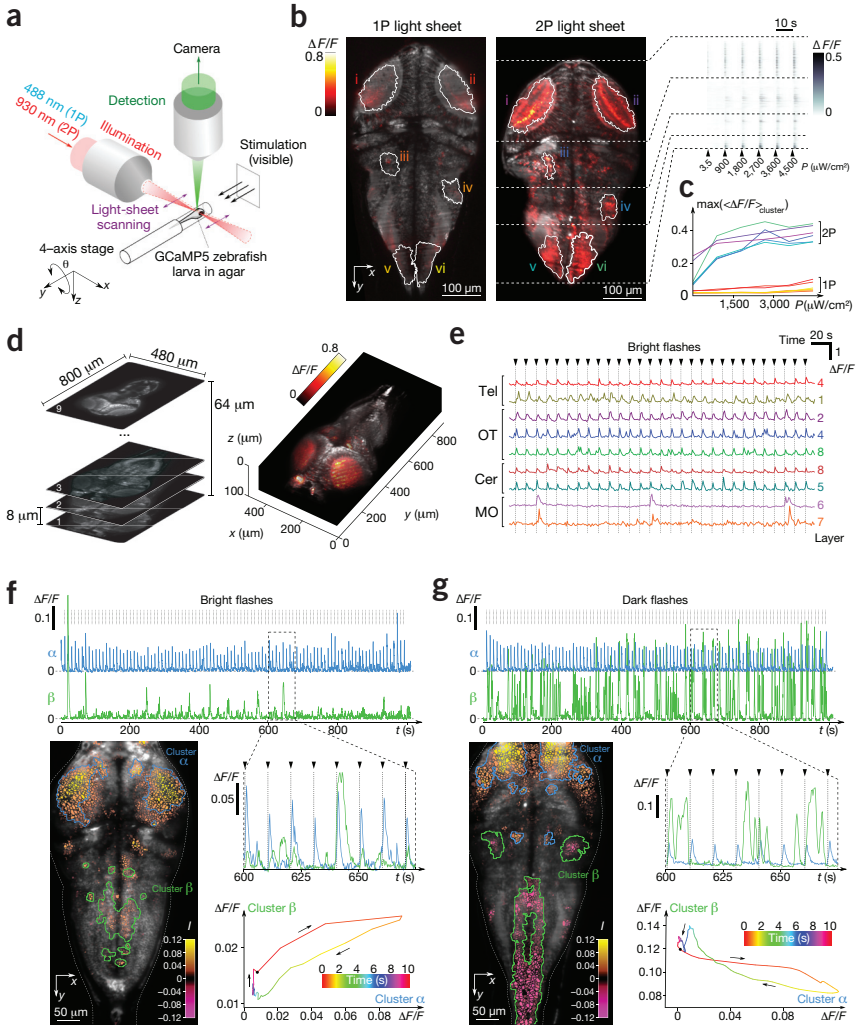

Figure 1 | Two-photon (2P) light-sheet functional imaging of visually evoked neural activity. (**a**) The 1P/2P light-sheet imaging system. (**b**) Left, brain-wide section of a 5-d-old larva overlaid with the flash-evoked neural response ($\Delta F/F$, 250 ms after the flash) measured with 1P and 2P light-sheet imaging. Images were recorded at 4 Hz and averaged over 20 successive flash presentations at 4,500 µW cm^{-2}. Right, post-stimulus raster plot of 3,283 neurons and neuropil regions. Data are averaged over 20 flash presentations for each stimulus intensity. (**c**) Post-stimulus response of the regions contoured in **b** for various stimulus intensities. Data in **b**,**c** are representative of $n = 9$ larvae. (**d**) 3D recording of activity evoked by 3,600 µW cm^{-2} flashes. A stack of nine layers with 8-µm intervals was recorded every second, yielding a total of 36,063 neurons monitored at 1 Hz. The 3D volume rendering of the fish brain shows the $\Delta F/F$ response measured immediately after the flash. (**e**) Typical signals of flash-responsive neurons in different brain regions (Tel, telencephalon; OT, optic tectum; Cer, cerebellum; MO, medulla oblongata). (**f**,**g**) Network analysis of flash-induced neural responses. The images display the stimulus-averaged response to a 200-ms-long bright flash (**f**) or a 1-s-long dark flash (**g**). The color code in the micrographs represents the variation of $\Delta F/F$ averaged over the first 1.5 s after the flash. The blue and green lines delimit the two most prominent neuronal clusters responding to bright and dark red flashes as computed using the *k*-means algorithm ($k = 12$), whose time dynamics are shown in the three associated graphs. For bright flashes, the activity of the hindbrain cluster was enhanced after the flash onset, whereas dark flashes induced a transient reduction of its activity.

same fish. The imaged section was chosen so as to avoid direct exposure of the eyes to the illumination beam. During 2P imaging, the flashes elicited acute neural responses in various regions of the brain (**Fig. 1b** and **Supplementary Video 1**) even at the lowest flash intensity (3.5 μW cm^{-2}). At an illumination intensity compatible with 3D imaging, the response during 1P imaging was either abolished or greatly attenuated (**Fig. 1b** and **Supplementary Video 2**). To quantify this observation, we extracted the maximum of the post-stimulus signal in the five most responsive regions in both experiments. In 2P imaging, all regions displayed a substantial response at the lowest stimulus intensity, which rapidly reached a plateau as the visual stimulation became more intense (**Supplementary Figs. 5** and **6,** and **Fig. 1c**). During 1P imaging, the visually evoked activity was mostly confined to the tectal neuropil, the region that receives direct projections from retinal ganglion cells. To elicit measurable signals in other brain areas, the stimulus intensity had to be increased up to 4,500 μW cm^{-2}, beyond physiologically relevant levels.

The exact mechanism by which 1P illumination leads to the observed reduction in visual sensitivity remains to be elucidated. The photoreceptors in the retina may receive excitation light scattered by the observation chamber or by the brain tissue, increasing the response threshold to subsequent visual stimuli. Alternatively, the visually evoked neural response may be attenuated owing to direct activation of light-sensitive cells throughout the brain. In any case, our results highlight the potential problems associated with visible illumination wavelengths and argue for the use of near-infrared wavelengths when studying visually driven processes.

2P light-sheet imaging combines the advantages of near-infrared illumination with the high speed of light-sheet microscopy. We produced 3D maps of flash-responsive neurons in a single experiment by sequentially moving the recorded plane across the brain and simultaneously recorded >36,000 individual neurons at 1 Hz (**Fig. 1d**,**e**, **Supplementary Fig. 7** and **Supplementary Video 3**), without compromising signal-to-noise ratio. Brain-wide parallel recording of multiple brain regions opens the possibility of identifying extended clusters of neurons by analyzing the structure of the correlation matrix (**Supplementary Methods** and **Supplementary Fig. 8**). Cluster dynamics can then provide a low-dimensional description of the post-stimulus time sequence of brain activity (**Fig. 1f**,**g** and **Supplementary Fig. 9**).

In conclusion, we demonstrated that near-infrared 2P light-sheet imaging is suitable for 3D brain-wide functional imaging in zebrafish larvae at cellular resolution. Notably, this imaging method eliminates the photostimulation associated with 1P functional imaging. Although the latter does not abolish robust visuomotor reflexes, we showed that it compromises visual perception in the blue domain. Therefore, 2P light-sheet imaging is a suitable alternative method for whole-brain network analysis of neural processes that require fine control over the visual stimuli or that are sensitive to the photic environment.

Note: Any Supplementary Information and Source Data files are available in the online version of the paper (doi:10.1038/nmeth.3371).

ACKNOWLEDGMENTS

We thank F. Engert (Harvard University) for providing the Huc:GCaMP5G strain. The study was partly supported by Agence Nationale de la Recherche (contracts ANR-2010-JCJC-1510-01, ANR-11-EQPX-0029, ANR-10-INBS-04), Fondation Louis D. de l'Institut de France, European Union Seventh Framework Program (Marie Curie International Reintegration Grant no. 268379).

COMPETING FINANCIAL INTERESTS

The authors declare no competing financial interests.

Sébastien Wolf[1,2], Willy Supatto[3], Georges Debrégeas[1,2], Pierre Mahou[3], Sergei G Kruglik[1,2], Jean-Marc Sintes[3], Emmanuel Beaurepaire[3] & Raphaël Candelier[1,2]

[1]Sorbonne Universités, Université Pierre et Marie Curie Paris 06, Paris, France. [2]Centre National de la Recherche Scientifique (Unité Mixte de Recherche 8237), Laboratoire Jean Perrin, Paris, France. [3]Laboratoire Optique et Biosciences, Ecole Polytechnique, Centre National de la Recherche Scientifique (Unité Mixte de Recherche 7645) et Institut National de la Santé et de la Recherche Médicale (U1182), Palaiseau, France.
e-mail: georges.debregeas@upmc.fr or raphael.candelier@upmc.fr

1. Panier, T. *et al. Front. Neural Circuits* **7**, 65 (2013).
2. Ahrens, M.B., Orger, M.B., Robson, D.N., Li, J.M. & Keller, P.J. *Nat. Methods* **10**, 413–420 (2013).
3. Vladimirov, N. *et al. Nat. Methods* **11**, 883–884 (2014).
4. Risner, M.L., Lemerise, E., Vukmanic, E.V. & Moore, A. *Vision Res.* **46**, 2625–2635 (2006).
5. Fernandes, A.M. *et al. Curr. Biol.* **22**, 2042–2047 (2012).
6. Truong, T.V., Supatto, W., Koos, D.S., Choi, J.M. & Fraser, S.E. *Nat. Methods* **8**, 757–760 (2011).
7. Portugues, R. & Engert, F. *Curr. Opin. Neurobiol.* **19**, 644–647 (2009).
8. Roeser, T. & Baier, H. *J. Neurosci.* **23**, 3726–3734 (2003).

MiXCR: software for comprehensive adaptive immunity profiling

To the Editor: High-throughput sequencing is gaining importance in adaptive immunity studies, demanding efficient software solutions for immunoglobulin (IG) and T-cell receptor profiling[1]. Here we report MiXCR (available at http://mixcr.milaboratory.com/ and https://github.com/milaboratory/mixcr/), a universal framework that processes big immunome data from raw sequences to quantitated clonotypes. MiXCR efficiently handles paired- and single-end reads, considers sequence quality, corrects PCR errors and identifies germline hypermutations. The software supports both partial- and full-length profiling and employs all available RNA or DNA information, including sequences upstream of V and downstream of J gene segments (**Fig. 1**, **Supplementary Note 1** and **Supplementary Table 1**).

In contrast with previous software[2–5], MiXCR employs an advanced alignment algorithm that processes tens of millions of reads within minutes, with accurate alignment of gene segments even in a severely hypermutated context (**Supplementary Note 2** and **Supplementary Tables 2–6**). In paired-end sequencing analysis, MiXCR aligns both reads and aggregates information from both alignments to achieve high V and J gene assignment accuracy. It handles mismatches and indels and thus is suitable even for sequences with many errors and hypermutations. MiXCR employs a built-in library of reference germline V, D, J and C gene sequences for human and mouse based on corresponding loci from GenBank[6].

MiXCR further assembles identical and homologous reads into clonotypes, correcting for PCR and sequencing errors using a heuristic multilayer clustering. Additionally, it rescues low-quality reads by mapping them to previously assembled high-quality clonotypes[7] to preserve maximal quantitative information (**Supplementary Note 3**). The Illumina MiSeq platform currently allows for deep full-length IG repertoire profiling with ~20 million long paired-end reads. MiXCR captures all complementarity-determining regions (CDRs) and framework regions of immune genes and permits the assembly of full-length clonotypes. Flexibility to analyze partial-length data is also provided, allowing, for example, users to group reads into clonotypes

Chapter 4

Evoked responses

Contents

The stimulation/response paradigm is central in neuroscience. I will thus present in this chapter some results that we could obtain when we applied stimuli and recorded responses, for different sensory modalities.

Chemical stimulations

To measure how he nervous system detects, converts and process sensory information one has to finely control the animal's environment, *i.e.* the set of stimulations to which it is submitted. In pratice, with zebrafish larvae this is relatively simple for vision, feasible for audition [10], touch and thermal sensitivity, but difficult for hydrodynamical perception *via* the lateral line and chemical perception. Indeed, given the small scales it seems extremely complex – and maybe currently out of reach – to control the flow around each superficial receptor of the animal. In the case of chemical perception, another layer of difficulty is added by diffusion and flow boundary conditions which can bias considerably the concentrations (see supplementary materials in [33] for a discussion).

We have developed a microfluidic system that allows for delivering localized stimulation over durations controlled down to the millisecond scale. We have obtained unprecedented reproducibbility levels, notably for product cleaning (stimulus offset). The microfluidic chips could also deliver alternatively two different solutions and could virtually simulate plumes similar to those encountered in real turbulent flows.

This setup has been designed to be combined with simultaneous recording of behavioral activity (tail beats) and neural activity with a point-scanning 2-photon microscope; with a few minor modifications, it could be adapted to fit in a light sheet microscope.

The following article presents some results we could obtain with those chips: in the framework of a collaboration with the team of Germán Sumbre (IBENS, Paris), we induced specific responses in primary gustatory (vagal lobe) and olfactory (olfactory bulb) areas. We controlled that these responses did not reflect a purely hydromechanical stimulation. Then, by varying the duration of an aversive stimulus from 50 to 500 milliseconds we could observe that the probability of triggering an escape response increases, as well as the number of active neurons, though the average fluorescence level stays constant. This suggests that aversive gustatory information is coded at the population level.

SCIENTIFIC REPORTS

OPEN

A microfluidic device to study neuronal and motor responses to acute chemical stimuli in zebrafish

Received: 17 March 2015
Accepted: 17 June 2015
Published: 21 July 2015

Raphaël Candelier[1,2,*], Meena Sriti Murmu[3,4,5,*], Sebastián Alejo Romano[3,4,5], Adrien Jouary[3,4,5], Georges Debrégeas[1,2,†] & Germán Sumbre[3,4,5,†]

Zebrafish larva is a unique model for whole-brain functional imaging and to study sensory-motor integration in the vertebrate brain. To take full advantage of this system, one needs to design sensory environments that can mimic the complex spatiotemporal stimulus patterns experienced by the animal in natural conditions. We report on a novel open-ended microfluidic device that delivers pulses of chemical stimuli to agarose-restrained larvae with near-millisecond switching rate and unprecedented spatial and concentration accuracy and reproducibility. In combination with two-photon calcium imaging and recordings of tail movements, we found that stimuli of opposite hedonic values induced different circuit activity patterns. Moreover, by precisely controlling the duration of the stimulus (50–500 *ms*), we found that the probability of generating a gustatory-induced behavior is encoded by the number of neurons activated. This device may open new ways to dissect the neural-circuit principles underlying chemosensory perception.

One of the main goals in neuroscience is to understand how the nervous system detects, processes and converts sensory stimuli into appropriate motor patterns. To do so, it is necessary to finely control the spatiotemporal patterns of sensory stimuli while monitoring the dynamics of large neural networks in awake animal models. Among vertebrate models, zebrafish offers a unique combination of assets for such studies. The transparency and relatively small dimensions of the brain at the larval stage, and the availability of transgenic lines expressing genetically encoded calcium indicators offer the possibility to perform functional imaging at single-cell resolution of virtually the whole brain in intact behaving animals[1–4].

The ability to deliver complex stimuli yet precisely controlled and with spatio-temporal structures analogous to those encountered in natural conditions is currently met only for the visual and auditory systems. In the zebrafish larva only the visual system was extensively explored where complex sensory-motor behaviors, consistent with that observed in freely swimming organisms, can be elicited by projecting natural scenes in front of an agarose-embedded larva[1,5]. In aquatic species chemosensation is used to find food sources[6], avoid danger[7], and to swallow or reject ingested particles[8,9]. In turbulent environments, akin to rivers, chemicals are transported in the form of fine-scale plumes such that the sequence of stimulation experienced by the fish consists of brief sporadic on/off stimuli. The time sequence of these events have been suggested to carry important information regarding the presence and location of the chemical source[10].

Delivering precise sequences of sharp pulses of water-soluble chemical stimuli to a tethered larva is a non-trivial problem. Methods that rely on passive transport from a point source inevitably produce a slow and uncontroled increase of the chemical concentration in the vicinity of the fish receptors. More

[1]Sorbonne Universités, UPMC Univ. Paris 06, UMR 8237, Laboratoire Jean Perrin, F-75005 Paris, France. [2]CNRS UMR 8237, Laboratoire Jean Perrin, F-75005 Paris, France. [3]Ecole Normale Supérieure, Institut de Biologie de l'ENS, IBENS, Paris, France. [4]INSERM, U1024, 75005 Paris, France. [5]CNRS, UMR 8197, 75005 Paris, France. *These authors contributed equally to this work. †These authors jointly supervised this work. Correspondence and requests for materials should be addressed to G.S. (email: sumbre@biologie.ens.fr)

active methods expose the face of the fish to the outlet of a small tube connected to a liquid valve, allowing to sequentially deliver buffer and stimulus solutions. In this configuration, the characteristic switching time is controlled by the tube length and the flow rate. The latter being constrained by the fish dimension and the maximum flow velocity ethologically acceptable, standard macroscopic delivery systems yield switching times in the 1–10 s range (see references and discussion in Supplementary information).

Here, we designed and fabricated a microfluidic device capable of delivering multiple chemical stimuli with unprecedented spatial and temporal precision (in the 1–10 ms range) to a larva partially restrained in agarose. This stimulation microfluidic device was combined with two-photon functional imaging and high-speed video recording to simultaneously monitor the brain activity and motor behavior. We first performed a comprehensive characterization of the microfluidic device delivery dynamics and demonstrated its capability of inducing taste-specific neuronal responses in the primary gustatory center of teleost fish, the vagal lobe, without generating mechanosensory stimulation. Second, we observed that two gustatory stimuli with different hedonic values (aversive and appetitive) induced distinct activity patterns in the primary gustatory center (vagal lobe) and in higher processing areas (gustatory telencephalon, Dm). Finally, the ability to precisely control the stimulus duration allowed us to study the neuronal principles underlying gustatory-induced motor behaviors. We showed that the stimulus duration (50–500 ms) was positively correlated with the the number of activated neurons in the vagal lobe, the probability of inducing a tail flip and the number of induced tail flips.

Results

The Microfluidic device. The microfluidic devices (Fig. 1 and Supp. Fig. 1) were fabricated by micro-milling onto transparent acrylic (PMMA) slabs. The fluidic channels, 100 μm in width and 25 to 200 μm in height, were sealed by 250 μm-thick transparent PMMA sheets using chemically-assisted thermal bonding. The circuit outlets are directed towards an open pool designed such that the larva, partially embedded in agarose, has its mouth precisely positioned in front of the delivery channel (Fig. 1d,e). The microfluidic device consists of two mostly independent circuits. The first one, driven by a push-pull syringe pump, imposes a continuous buffer flow circulating around the larva's face (blue arrows in Fig. 1e). The second circuit controls the delivery of two independent stimuli (*A* and *B*) *via* two electromagnetic microvalves. In the resting state, the stimulus reservoirs are at atmospheric pressure and the solutions are continuously pumped through a V-shaped channel to an underpressurized waste container. Switching a valve (injection state) overpressurizes one reservoir, triggering the instant release of the stimulus solution through the injection channel (Fig. 1b,c). Both stimuli share the same delivery outlet, thus guaranteeing that no spatial clue is associated with switching between stimuli. The device can be positioned under a two-photon microscope for simultaneous recording of neuronal activity (Fig. 1a), while a fast camera monitors the larva's tail movements from below, taking advantage of the chip's transparency.

A crucial feature of this design is the negative pressure imposed on the waste container, which drives a co-flow of the stimulus solution and the chamber fluid in the downstream arm of the V-shaped channel. Although the flow rate is relatively low (of the order of $1 \mu L.s^{-1}$), it prevents any cross-pollution between the buffer and the stimulus solution in the resting state, while guaranteeing through constant renewal that the stimulus solution at the entrance of the injection channels (i.e. ≈ 600 μm from the targeted sensory receptors) remains at the desired concentration.

Flow kinematics of the microfluidic device. To characterize the performances of the microfluidic device we monitored the delivery of a dye-containing solution using high-speed videography. For this purpose, we switched one of the microvalves to instantly increase the pressure to p_{in} in one of the stimuli reservoirs. The time-evolution of the relative concentration, probed along a line tangential to the animal's mouth (Fig. 2a,b), exhibited a rapid transition from zero (no dye) to one (nominal dye concentration) within a few tens of milliseconds (Fig. 2c). This transition dynamics was found to be highly reproducible and showed no significant dependence on the imposed pressure p_{in} for $p_{in} \geq 300\, mbar$. For each value of p_{in}, we computed the onset and offset time-delays (noted τ_r and τ_d, respectively) defined as the delays between the valve switching and the time at which the relative concentration reached half the maximal concentration (inset of Fig. 2c). We computed the evolution of the jet width (Fig. 2d), which showed a similar dynamics towards a plateau but with a plateau value that increased quasi-linearly with p_{in}. It is worth noting that despite the jet is one order of magnitude thiner than the mouth's size, it splits in two branches close to the head surface and flows symmetrically along the exposed parts of the head. The real surface of contact is thus determined by the amount of agarose removed around the larva's mouth. Tracking the position of the dye/water interface during injection onset, we also estimated the velocity of the propagation front as a function of the distance to the mouth, for various values of p_{in} (inset of Fig. 2d).

These hydrodynamic recordings revealed several important features of the device. First, the stimulation onset and offset delays were small compared to typical gustatory stimulation times and were weakly dependent on injection overpressure. The valve switching sequence consistently drove the effective stimulus presentation sequence, albeit with a constant time delay. This device thus allows for near-millisecond precision on the stimulus presentation time, *i.e.* when the stimulus actually contacts the animal. The shortest stimulus duration that can be delivered by the device was $\approx 35\, ms$, as it corresponds to the time

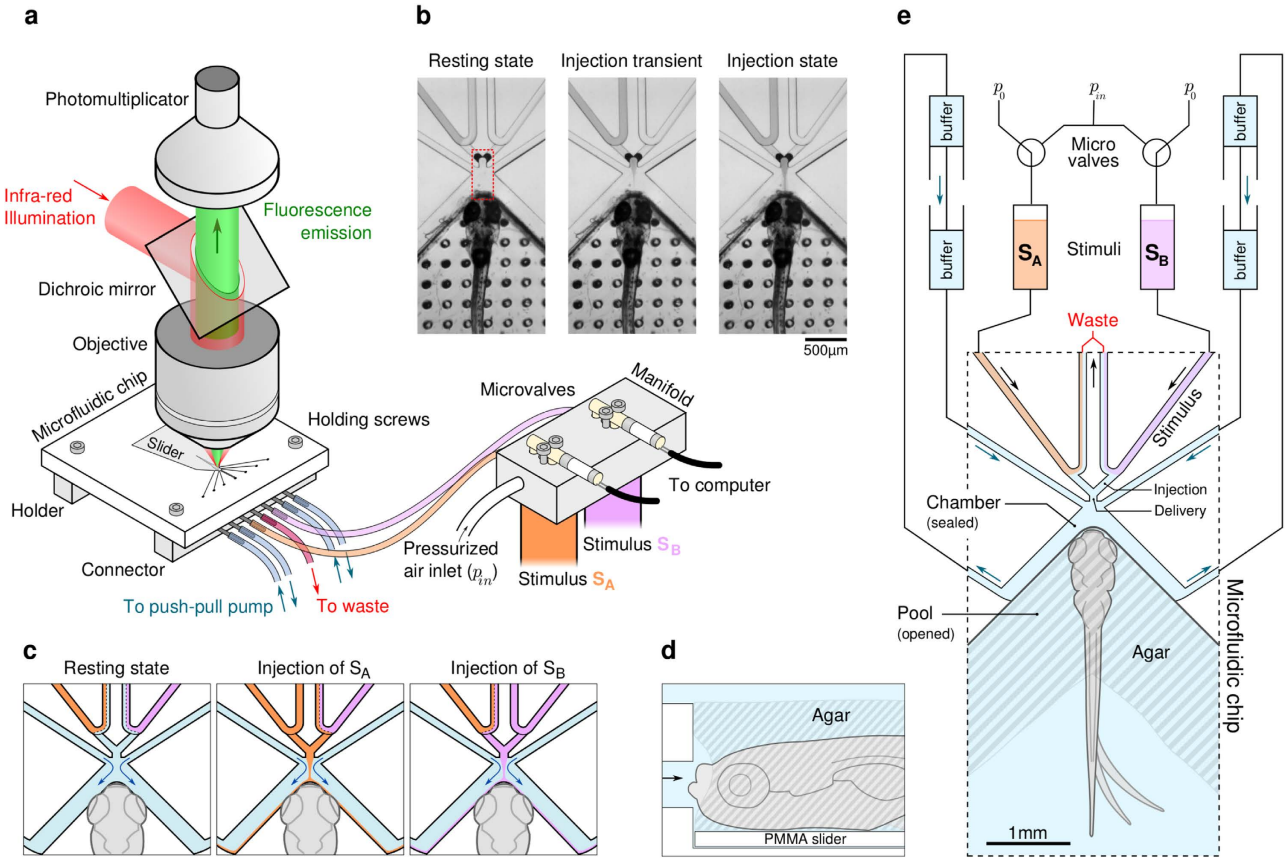

Figure 1. Microfluidic device for precise delivery of chemical stimuli. (**a**) Setup scheme: an epifluorescence two-photon microscope images neural activity while pulse-like stimuli are delivered to a zebrafish larva. An IR-sensitive camera images tail behavior from below. The microfluidic chip is connected to a computer-controlled manifold for the delivery of two different stimuli, S_A and S_B. (**b**) Infrared images of the device around the larva's face during injection of stimulus S_A (infrared dye, left channel). S_B (right channel) is buffer. The red rectangle indicates the region used in the kinematic view of Fig. 2a,b (c) Sketch of the fluid flow in the device during the three stationary states: at rest, during injection of S_A and during injection of S_B. (**d**) Side-view scheme of the larva's head resting on the movable slider. The animal's face is gently cleared before positioning. (**e**) Scheme of the microfluidic device: the larva's head embedded in agarose lying on the mobile slider is positioned in the pool in front of the delivery channel. Two electro-microvalves control pressures in stimuli reservoirs S_A and S_B and trigger injection. p_0 is the atmospheric pressure and $p_{in} > p_0$.

needed for the injection flows to reach a stationary state. We could also generate reproducible pulses of less than 10 *ms*, but in this regime the maximal concentration did not reach the nominal concentration. Second, the flow velocity on the fish face was independent of the injection pressure: it was imposed by the continuous buffer flow that pinches the stimulus jet and drags it to the animal. This process guarantees that the hydromechanical stress imposed on the larva is strictly invariant during and between stimuli presentations, with no modification at pulse onset and offset, such that no artifactual mechanosensory clues should accompany the chemical stimulation.

Gustatory neuronal responses. To test whether the gustatory-stimulus delivery could also stimulate mechanosensory receptors, we examined gustatory-evoked neuronal responses elicited by pulse-like exposure to distinct flavours. We probed in particular the specificity of the neuronal response to gustatory inputs and the absence of associated activation of mechanosensory receptors around the larva's mouth induced by change in the flow pattern. Two-photon calcium imaging was perfomed on six-to-seven day old Huc:GCaMP3 transgenic larvae[2] first restrained in low-melting agarose (see **Sample preparation** in **Methods**). Prior to positioning them within the stimulation device, we carefully removed the agarose around the larva's mouth in order to expose the lips and mouth cavity, a region rich in taste buds[11–13].

The two stimulation channels were first used to alternatively deliver series of five 300 *ms*-long pulses of sour (citric acid, 10 *mM*) or tasteless (buffer, control) stimuli. The most responsive primary gustatory centers in teleost fish are the facial (VII), glossopharyngeal (IX) and vagal (X) lobes[14]. At the developmental

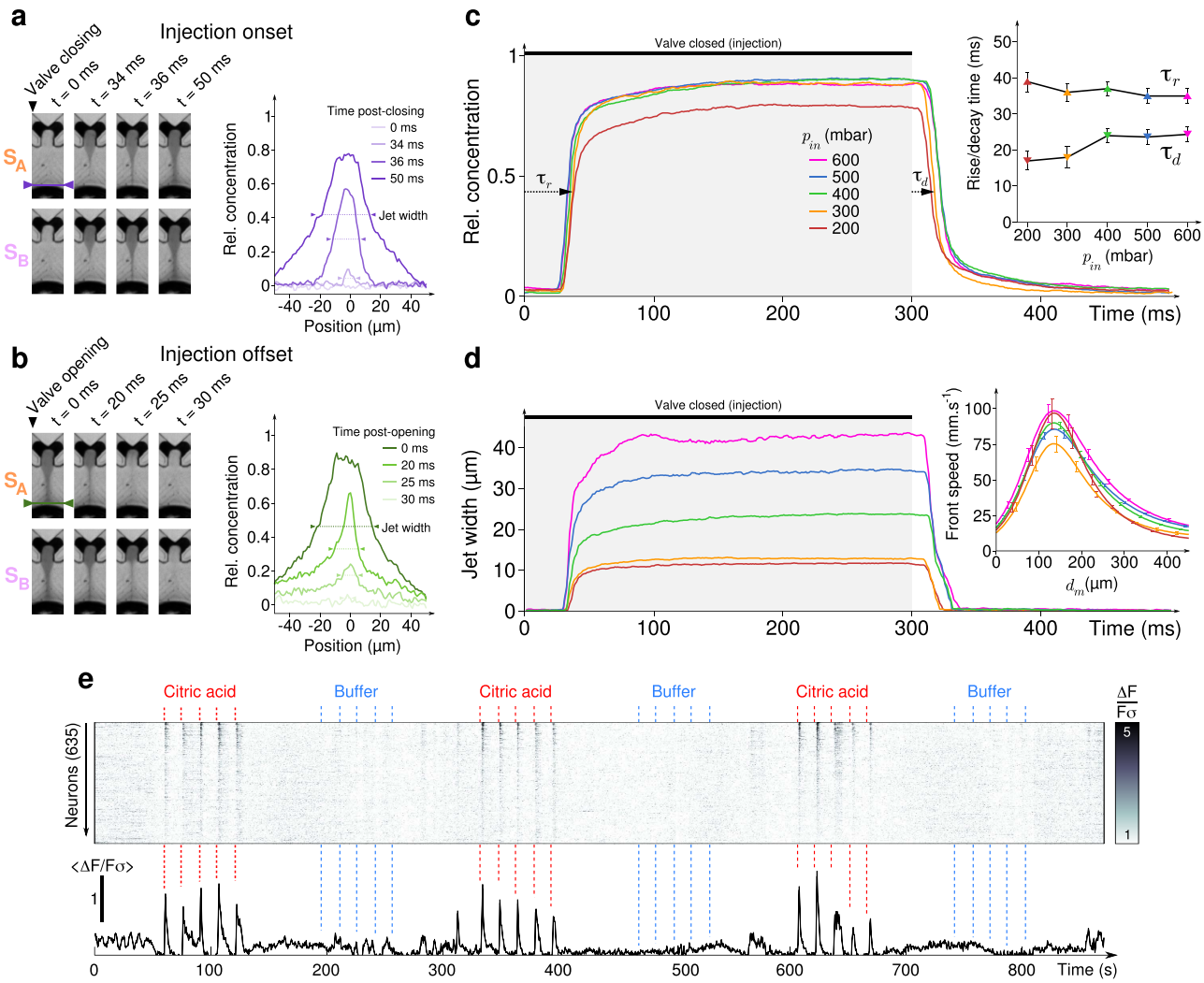

Figure 2. Flow characterization in the microfluidic device. (**a–b**) Left: kinematic view of the chamber during injection onset (**a**) and offset (**b**), for stimuli S_A and S_B, recorded with a high-speed camera. For (**a–d**), S_A and S_B are an IR-dye used to characterize the flow dynamics. The region of interest is highlighted on Fig. 1b: the outlet of the delivery channel is at the top while the larva's head tip is at the bottom of each frame. Right: Profiles of the relative concentration along a cross section of the chamber close to the larva's mouth (purple and green lines on the kinematic view) at different moments after closing (**a**) or opening (**b**) the micro-valves. Jet's width is defined as the width of the profile at half-maximum relative concentration. (**c**) Evolution of the relative concentration of the profiles shown in (a-b) for different reservoir pressures p_{in}, averaged over 5 trials. Inset: rising (▲ τ_r) and decay (▼ τ_d) times such that the system reaches half the maximal relative concentration after microvalve switch, as a function of p_{in}. (**d**) Evolution of jet width for different values of p_{in}, averaged over 5 trials. Inset: Speed of the stimulus front during injection onset as a function of the distance to the larva's mouth d_m, for different p_{in}. Same color code as in (**c**). (**e**) Raster (top) and average trace (bottom) of the normalized neuronal activity $\Delta F/F\sigma$ in the vagal lobe during alternate presentations of citric acid (CA, first stimulus S_A) and buffer (second stimulus S_B) at $p_{in} = 500\,mbar$. Neurons are ordered by decreasing responses to CA pulses. Similar responses were obtained for $n = 10$ larvae. For each channel, three trains of five 300 *ms*-pulses separated by 15 *s* were delivered. Error bars: standard deviations.

stage for which the recordings were made the glossopharyngeal lobe is not yet fully-developed and is rather difficult to identify. In large-field imaging experiments (not shown) we could observe some activity in the vagal and facial lobes with acute citric acid stimulations, which suggests that most probably the stimuli activated both external (lips) and intraoral taste buds. The strongest responses where evoked in specific neuronal populations of the vagal lobe (Fig. 2e). Importantly, the control solution elicited no measurable activity, thus indicating that the measured evoked activity in the vagal lobe is solely representative of gustatory inputs rather than other variables associated with the stimulus (e.g. hydro-mechanical cues)

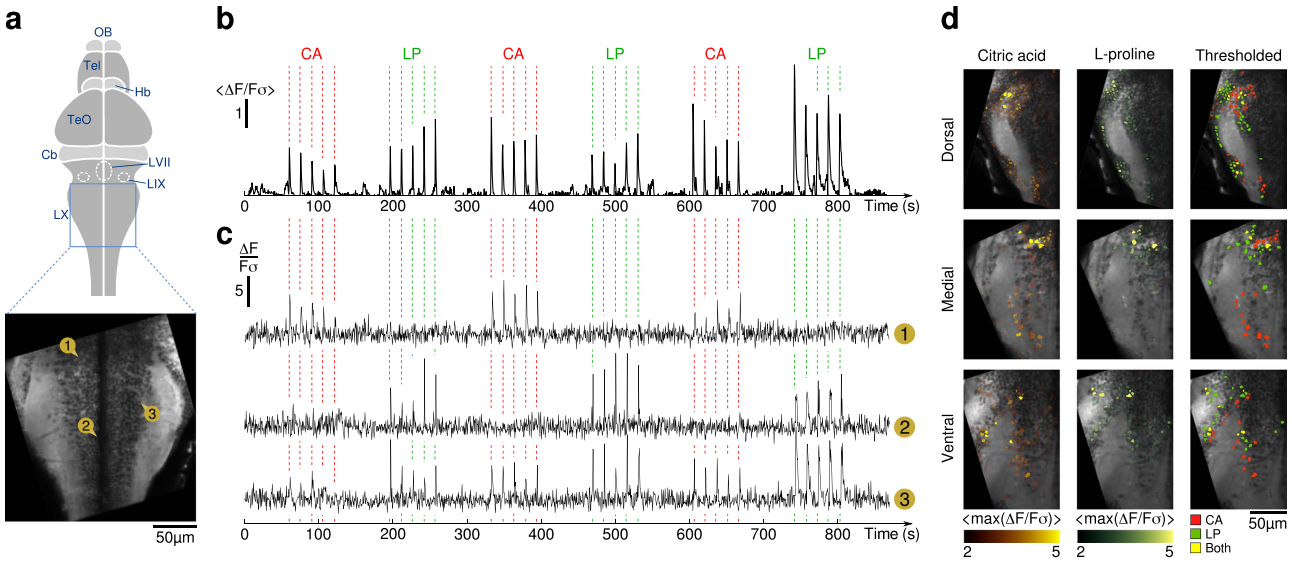

Figure 3. Neuronal responses to chemical stimulation. (**a**) Scheme of the larval brain and average fluorescence image of the vagal lobe. Neurons ① to ③, whose traces are shown in (**c**), are pinpointed. (**b**) Trace of the normalized neuronal activity averaged across all identified neurons of the vagal lobe. For each tastant, three trains of five 300 *ms* pulses separated by 15 *s* were delivered. (**c**) Normalized neuronal activity $\Delta F/F\sigma$ of three neurons of the vagal lobe during alternate presentations of CA (stimulus S_A) and LP (stimulus S_B). Neuron ① responds exclusively to CA, ② responds exclusively to LP and ③ responds to both. (**d**) (Left, Middle) Maximum of $\Delta F/F\sigma$ measured in the first 3 *s* following stimulus onset, averaged over 15 identical pulses, overlaid on the imaged plane (gray). (Right) Neurons responding to CA only (red), LP only (green) or both (yellow). $p_{in} = 500\,mbar$.

Neuronal representation of gustatory stimuli with different hedonic values. The possibility offered by the microfluidic device to rapidly alternate the presentation of two stimuli allowed us to compare between the gustatory-induced activity patterns associated with distinct gustants in a single experiment. We illustrated this capability using two stimuli of distinct hedonic values: sour aversive, citric acid (CA) and appetitive umami, L-proline (LP). We sequentially delivered series of 300 *ms*-long pulses of either compound while recording neuronal activity in the vagal lobe (Fig. 3) . The mean signal, averaged over all identified neurons of the vagal lobe, show important responses at the population level (Fig. 3b), while at the single-cell level neuronal responses to either or both tastants have been observed (Fig. 3c). Although the topology of the gustatory-induced activity patterns appeared intermingled, we observed for three different planes (dorsal, medial and ventral) that a large fraction of neurons responded exclusively to either CA or LP, while a few responded to both (see Fig. 3d).

In the zebrafish larva, ascending projections carrying taste-related signals reach diencephalon and telencephalic areas. We thus similarly monitored CA and LP-induced responses in the dorsal telencephalic area (Supp. Fig. 3), a region known to respond to gustatory stimuli[15]. Interestingly, we found that even in higher gustatory centers, both CA and LP-induced responses remained relatively segregated.

Effect of stimulus duration on gustatory-induced neuronal responses and motor behavior. In aquatic species, the gustatory system is not only responsible for the decision of swallowing or rejecting ingested objects, but it also enables the animal to detect the location of potential food sources[6] or to trigger escape from dangerous chemicals and water conditions[7]. Large amplitude tail deflections were robustly evoked by brief exposures to CA, an aversive tastant for the larva (Supp. Movie. 3 and 4). We took advantage of the unique time-precision of the microfluidic device and its suitability for simultaneous two-photon imaging and motor behavior video-monitoring to investigate the neuronal mechanisms underlying gustatory-induced motor behaviors (Fig. 4a).

We observed that acute CA stimulation induced discrete, one-sided tail flips (see Supp. Fig. 4c, Supp. Movie. 3 and Supp. Movie. 4) sometimes followed by short series of weaker oscillations, a behavior that is reminiscent of escape responses (C-turn). These responses occured with a probability that consistently increased with the stimulus duration (Fig. 4b). The average number of tail flips immediately following the stimulus presentation were also positively correlated with the stimulus duration (Fig. 4c). We found that the overall neuronal evoked response in the vagal lobe was larger when this was associated with a tail motor behavior. Thus, to probe the neural activity directly evoked by the gustatory inputs we separately analyzed the events that did not induce a tail flip.

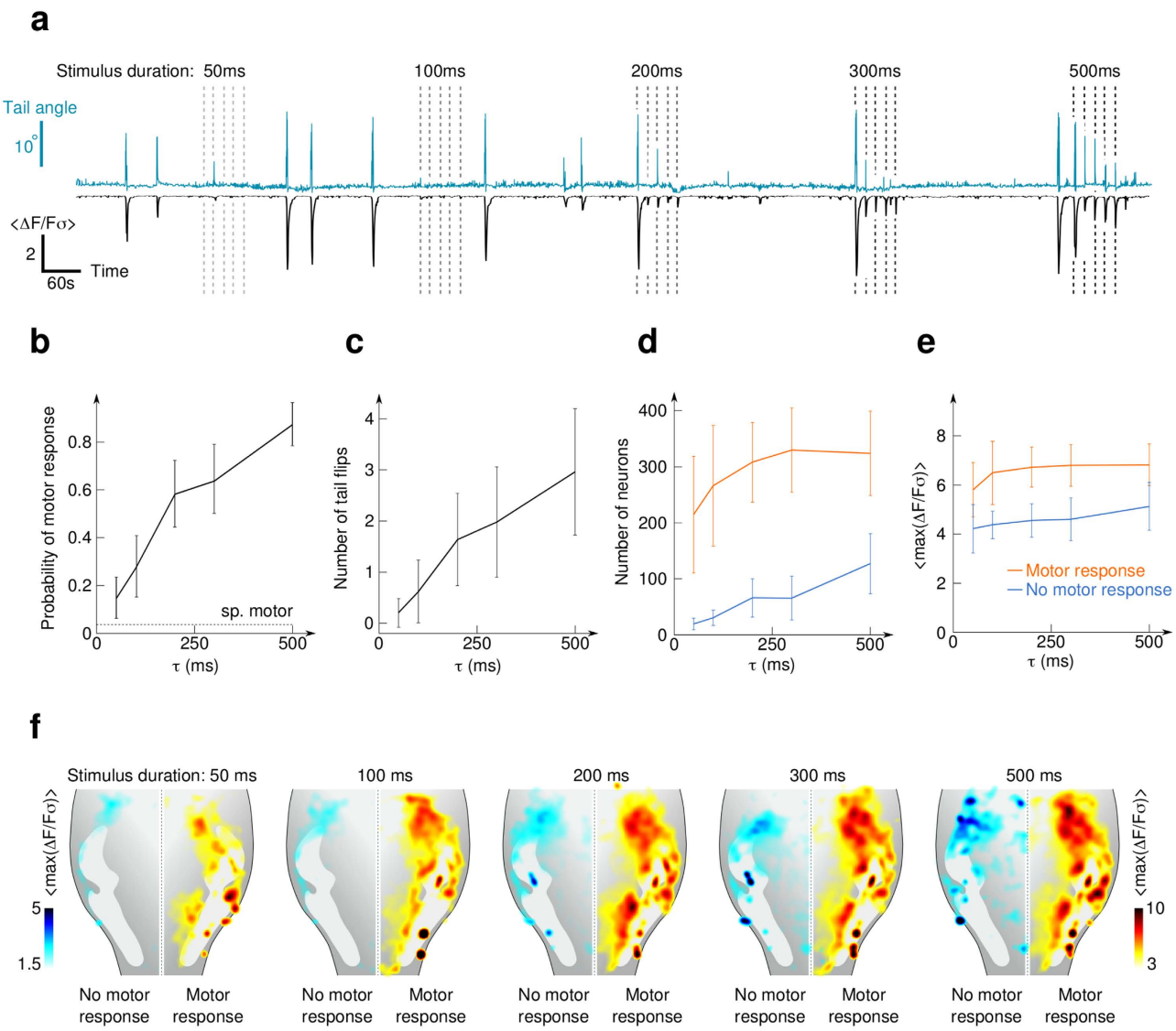

Figure 4. Effect of stimulus duration on behavioral and neuronal responses. (**a**) Time-traces of the tail angle and average normalized neuronal activity in the vagal lobe during trains of five similar stimuli of citric acid. The trains contained stimuli of increasing duration (50–500 *ms*). (**b**) Probability of observing at least one tail flip in a time interval of 3 *s* following the stimulus onset. The probability of a spontaneous tail movement in a random 3 *s* interval far from stimulation is close to zero (dashed line). (**c**) Average number of tail flips in a time interval of 3 *s* follwowing stimulus onset. (**d**) Number of neurons responding to the stimulation in trials for which no motor response (blue) or a motor response (orange) was observed. (**e**) Amplitude of the response (defined as the maximum of $\Delta F/F\sigma$ in the 3 *s* post-stimulation) averaged across the responsive neurons in trials associated (orange) or not associated (blue) with a motor response. (**f**) Topographical organization of the gustatory-evoked neuronal response patterns in the vagal lobe circuit. The color code reflects the amplitude of the response averaged across trials where no motor response was evoked (left) and trials where a motor response was observed (right) for the five different stimuli durations. For (**b**–**f**), data were pooled from 11 larvae (22 half vagal lobes) to which 25 stimuli were presented as shown in (**a**). The recorded area is the same as in Fig. 3. Error bars: standard deviations. $p_{in} = 500\,mbar$.

For trials not associated with a motor response, we observed a quasi-linear relationship between the number of activated neurons and the duration of the chemical pulses (Fig. 4d, blue). Interestingly, the Ca^{2+} transient amplitude of the responding neurons were much less affected by the stimulus duration (Fig. 4e). When the stimuli induced a tail flip, an intense and extended neuronal response was measured as shown in Fig. 4d,f. The differences in topography for gustatory-induced responses associated or not associated with motor behaviors suggest that rostro-lateral regions are associated with the sensory response while more caudo-medial ones are associated with the gustatory-induced motor response, as illustrated in Fig. 4f.

These results demonstrate that the stimulus duration is mainly encoded by the number of activated neurons in specific regions of the vagal lobe. The latter drives in a probabilistic manner a discrete transition towards a neuronal-circuit state capable of inducing a tail-flip response.

Olfactory-induced neuronal responses in the olfactory bulb. As a proof of concept, we performed experiments to validate the suitability of the microfluidic device for olfactory stimulation in zebrafish larvae. For this experiment, we presented to the larva's nostril two odor-specific aminoacids (lysine and phenylalanine, 300 *ms* pulses, 10 *mM*) while monitoring changes in calcium dynamics for three different focal planes of the olfactory bulb along the dorso-ventral axis (dorsal, medial and ventral). We observed that the two odorants induced distinct neuronal response patterns (Supp. Fig. 4) as previously reported[16].

Discussion

In recent years, advances in soft-microlithography techniques have led to the design of microfluidic chips for the manipulation of small organisms[17]. Recently, a microfluidic high-throughput system has been proposed to simultaneously immobilize and orient tens of larvae while enabling functional imaging[18]. The miniaturization allows for fast modifications of the flow pattern to which the specimen is exposed while still operating in the laminar flow regime and mitigate cross-diffusion between the different solutions. Microfluidic approaches were also used for chemical stimulation in *C. Elegans*[19,20].

Here, we designed an open-ended microfluidic chip that combines the advantage of miniaturization for precise control over fluid flow with the possibility to perform simultaneous behavioral and neuronal activity recordings on agarose-restrained zebrafish larvae. The micro-milling method enables direct micro- and macro-patterning on a single chip, such that the microfluidic channels (in the 100 μm range) could be directed onto an open pool (in the *cm* range) where the partially-restrained larva can be precisely positioned. This relatively simple fabrication method presents further advantages compared to standard soft-microlithography approaches: the circuit can sustain high pressures (in the *MPa* range), the channels dimensions can be adjusted in the 3 dimensions on 4 orders of magnitude with virtually no constraint on aspect ratio. These characteristics allow for precise adjustment of hydraulic resistances and flow pattern across the circuit. Furthermore, the chip can be rapidly replaced without changing the remote macro-scale delivery system (tubing, valves, pumps, stimuli reservoirs, etc.) through the use of custom-made connectors.

The capability of this chip to sequentially deliver multiple step-pulse-like stimuli, combined with whole-brain calcium imaging, opens new avenues to dissect the neuronal circuits underlying chemosensory processing in the vertebrate brain. First, it allows for the identification of tastants-specific neuronal networks across several trials and animals. This approach, which is routinely used in visual studies, was here implemented to identify neuronal circuits engaged in processing aversive versus appetitive information along the gustatory pathways.

The device unique capacity of delivering short square-pulse-like stimuli enabled us to study the neuronal mechanisms underlying gustatory-induced motor behaviors. We observed that the duration of the exposure to citric acid in the 50–500 *ms* range is mainly encoded by the number of recruited neurons in specific regions of the primary gustatory center, which in turn predicts both the probability of triggering an escape-like behavior and the number of induced tail movements. We thus suggest that gustatory perception in the zebrafish larva, *e.g.* the neuron-computational process leading to an adequate motor behaviour, takes place early in the gustatory pathway and is dictated by the number of neurons activated by the gustant.

The ability to rapidly switch between two distinct stimuli could be used in a straightforward way to study the neural processing involved in more complex stimulation sequences, and to analyse for instance how gustatory and olfactory stimuli interferes when presented with short time-lags.

Although we here focused on gustatory and olfactory neuronal processing *in vivo*, the same device can be directly used to probe the effect of transient exposure to drugs in *ex vivo* preparations. Given the large available library of zebrafish models of human syndromes, this technique has the potential to become a powerful tool for high-throughput vertebrate pharmaceutical screenings towards the development of new drugs.

Methods

Microfluidic chip fabrication. The chip design has been iteratively optimized to reduce the transition times (onset and offset of delivery). The angle at which the continuous circulating buffer flow is directed in the chamber has been determined with the use of a finite-element software (Comsol). For fabrication, we used a computer-controlled micromilling machine (Minitech Mini-Mill/GX) which allows for submicronic precision, and a custom set of programs to generate G-code machine instructions. A microscope (0.75× to 3× Microscope Body, Edmunds Optics) and camera where mounted on the micromilling machine to allow for precise positioning ($\approx 1\,\mu m$ in the tool axis direction) during tool change. Fabrication workflow was as follows: on a horizontal $40 \times 40 \times 4\,mm$ PMMA slab, (*i*) the seven input/output through holes (600 μm-diameter drill, KT-0236-R, PMT Microtools, USA) were drilled, (*ii*) an area of $25 \times 15\,mm$ was surfaced with a 3 *mm* smoothing tool (3 *mm*-diameter radius-end mill, MSRS 230, NS Tools, Japan) to obtain a flat reference surface (optical grade), (*iii*) channels were milled

(100 μm-diameter mill, TR-2-0040-S, PMT Microtools, USA), and finally (*iv*) the open chamber was milled (500 μm and 3 mm-diameter mills, resp. TR-2-0200-S and SR-2-1181-S, PMT microtools, USA). The cover was milled out of a $22 \times 27 \times 0.25\,mm$ thin PMMA sheet (ME303005, Goodfellow) using a 500 μm-diameter mill (TR-2-0200-S, PMT microtools, USA) to match the shape of the chamber such that the latter remains open after sealing. The chip and cover were washed three times for 5 min in 25% isopropanol and manually aligned under a microscope. Short laser pulses (45 W, Hobby 5^{th} gen., Full Spectrum Laser, USA) were used to locally melt the PMMA at distant locations from the channels in order to secure alignment during chemically-assisted thermal bonding. Some chips used in this work were sealed with a DMSO/methanol-based melting agent, following the protocol of Ref. 21, but our most recent chips were sealed with a custom protocol that provided better resistance with a less toxic melting agent: 50% acetic acid at 65°C for 15 min under a 1.7 MPa load per chip. The chips were rinsed several times with distilled water before use.

Flow control and measurements. A custom brass connector (see Supp. Fig. 1-b) was screwed onto the lower side of the chip to connect the input/output channels to the pressure control manifold, the push-pull syringe pump and the waste container. The continuous buffer flow in the chamber was generated by a push-pull syringe (Legato 270, Kd Scientific), operated at a constant volumic flow rate of $2\mu L.s^{-1}$. A custom-made duralumin manifold was used to connect the chip, the stimulus reservoirs and the microvalves. Two 3-way electro-microvalves (LHDA0533115H, The Lee Company) controlled the pressure in the stimuli reservoirs. An I/O device (Arduino UNO) was used to send TTL pulses to an amplifier connected to the microvalves and to trigger the high-speed camera. Microvalves were normaly opened on atmospheric air p_0 and closed on a pressure source p_{in}, most generally set at 500 $mbar$ overpressure. The waste reservoir surface was positioned below the chamber, which set its pressure $\approx -50\,mbar$. Flow recordings were performed with a high-speed camera (Fastcam APX-RS, Photron, Japan) operated at 1 kHz under infra-red light (850 nm, SFH4750, Osram). An infra-red dye (IR-806, Sigma) was dissolved in distilled water ($c_0 = 0.34\,mM$). Traces of precipitate were eliminated *via* filtering (0.22 μM, Millipore). To obtain concentrations from pixel intensities, we measured the molar absorptivity of the dye solution ($\varepsilon = 600\,m^2.mol^{-1}$) and applied Beer-Lambert's law: $c = log_{10}(I_0/I)/\varepsilon l$, where I_0 and I are the pixel intensities with buffer and dye and l is the thickness of the channel. Relative concentrations were computed as c/c_0. Tastant and odorant stock solutions (Sigma) were made at 100 mM in distilled water and diluted in embryo medium just before imaging to reach the concentration of 10 mM.

Zebrafish larvae. Transgenic zebrafish larva expressing a genetically encoded calcium indicator GCaMP3 under a pan-neuronal promoter, HuC (as described in Ref. 2) was used for all experiments. The HuC:GCaMP3GS5 line embryos were collected and raised at 28.5 °C in E3 embryo medium. Larvae were kept under 14/10 hours on/off light cycles and fed after 6 d.p.f. All experiments were carried out in accordance with approved guidelines and approved by *Le Comité d'Éthique pour l'Expérimentation Animale Charles Darwin* (Ce5/2009/027).

Retrograde Labeling. To label the reticulospinal and vestibulospinal neurons in the hindbrain, we performed retrograde labeling by injecting a Dextran Texas Red dye (10,000 MW, Invitrogen) in the spinal cord. One day prior to imaging, 5 days-old HuC:GCaMP3 zebrafish larvae were embedded in 2% low-gelling agarose. The larva was placed on their side in a drop of Ringer solution. A 50% solution of Dextran Texas Red in 10% Ringer solution was pressure-injected *via* a glass microelectrode (10–20 μm tip diameter) inserted into caudal spinal cord at the level of the anus using $3 \times 100\,ms$ pulses. The dye penetrated the spinal cord axons *via* the damaged axons. After injection the fish were allowed to recover and kept in fish embryo media until further use. A day later, the larva was embedded in 2% low-gelling agarose. Fluorescent-labeled reticulospinal and vestibulospinal neurons were imaged using two-photon scanning microscopy. This experiment was used as a clear landmark for the recognition of the vagal lobe $\approx$30 μm dorso-caudally to the reticulospinal and vestibulospinal neurons (see Supp. Fig. 2).

Sample preparation. Six to seven days old zebrafish larvae were embedded in a drop of low-gelling agarose (2%, Sigma) on a movable slider (see Supp. Fig. 1-d). The slider was placed into an acrylic mold whose shape exactly corresponds to the pool without the channels. The larva was plunged into liquid agar at $\approx$30°C and a drop containing the larva was placed on the slider. The position of the larva could be slightly modified during the gelification process by moving surrounding agar with surgical tools. After some practice, we could optimize the position of the larva such that the head was very close to the slider tip and the body axis in the direction of the delivery channel. The slider was designed with an array of tiny holes (100 μm in diameter) at the location of the specimen to provide a strong grip between the slider and agar. Once agar had gelified, we removed the slider and gently cleared the larva's face with a dissecting pin under a binocular to expose its upper and lower lips (gustatory) or nostrils (olfactory). For experiments in which behavior was recorded, the tail tip was also cleared. For imaging experiments in which we did not monitored behavior, the larva was paralyzed in 300 μM pancuronium bromide (Tocris) added directly to the agarose. The preparation was kept in embryo medium until the slider was transferred to the microfluidic chip. A bath of embryo medium was maintained on top of the chip throughout

the experiments. During slider insertion, it was first introduced into the bath and then positioned in the pool to avoid air bubbles. All experiments were performed in the dark.

Two-photon calcium imaging. The two-photon microscope was based on a MOM system (Sutter) with a 25× objective (NA1.05, Olympus) and a laser tuned at 920 nm (Mai Tai DeepSee Ti:Sapphire). The output power at the focal plane was less than 3 mW. The filters consisted of an objective dichroic (FF705), a short-pass (IR Blocker, AFF01-680) and a band-pass filter (FF01 520/70), all from Semrock. The PMT was a H1070 (GaAsP) from Hamamatsu. The emission signal was pre-amplified with a SR-570 (Stanford Research Systems) and acquired using ScanImage at 1.95 Hz, with 256×256 pixels resolution. Recordings were made at three different optical sections, 20 μm apart. To maintain consistency between different recordings and in different animals, each layer was identified based on several anatomical landmarks (*e.g.* cell density, neuropil shape and size).

Image Processing. Calcium imaging videos were first registered using the Turboreg plugin for ImageJ. Then, regions of interest (ROIs) corresponding to every morphologically identifiable neuron were semi-automatically defined using a custom program. In GCaMP strains, fluorescence is mainly localized in the cytosol with minimum penetration to the cellular nuclei, so we first identified individual nuclei as local intensity minima. To obtain neuronal contours we computed the Euclidean distance of each pixel to the nearest minima and performed a watershed segmentation. ROIs typically included neuronal nuclei and a thin cytosolic surrounding ring, excluding the outermost cytosolic perimeter that could potentially be subject of cross-neuron fluorescence contamination due to high neuronal density. The obtained ROIs were manually inspected and corrected when necessary. Eventually, the fluorescence traces were computed as the average intensity over each ROI. To record motor behavior, a miniature microscope connected to a fast infrared camera (120 Hz, TXG02, Baumer) was placed below the microfluidic device. We computed the raw orientation of the binarized image of the tail, and tail angle was defined as the deviation from the baseline orientation[22,23]. The tail beats after each pulse were counted by eye. All algorithms were written in Matlab.

Neuronal data analysis. A baseline fluorescence signal was estimated for each neuron by computing the 8^{th} percentile of fluorescence traces $F(t)$ in sliding windows of 15 s[24]. The resulting smooth curve $b(t)$ locally approximated the baseline level and reflected slow fluctuations unrelated to the fast calcium transients evoked by neuronal activity. The relative variation of fluorescence intensity was calculated as $\Delta F/F = (F - b)/b$. In a typical experiment, trains of stimulations separated by 15 s alternate with phases without stimulation. We defined the resting times as the set of times for which no stimulation was delivered in the previous 15 s. For each neuron, we computed the standard deviation of the relative variation of fluorescence during resting times $\sigma = std(\Delta F/F)_{rest}$ and the normalized relative variation of fluorescence intensity $\Delta F/F\sigma$. To isolate neurons responding to a stimulation pulse, we computed m the maximum of $\Delta F/F\sigma$ in the first 3 seconds post-stimulation (seven images). To determine which neurons were significantly responding, we performed a Kolmogorov-Smirnov test to determine whether each value of m could arise from the distribution of the maximum of a set of seven normally distributed random points. A maximum of $m = 3.189$ corresponds to a p-value of 0.01, and was chosen as the responding threshold. For each fish, both sides of the time-averaged image of the vagal lobe were semi-manually registered onto a virtual "average" half-vagal lobe. Average patterns of activity were then obtained by convoluting the discrete field $\sum_i m_i \delta(x_i, y_i)$ of neurons stemming from several animals (11 larvae, hence 22 half-vagal lobes) with a Gaussian kernel of width $\sigma_k = 4.2\,\mu m$ and unit height. These maps were normalized by the density map, computed as the convolution of $\sum_i \delta(x_i, y_i)$ with a Gaussian kernel of width $2\sigma_k$ and height $1/\sigma_k^2$.

References

1. Ahrens, M. B. *et al.* Brain-wide neuronal dynamics during motor adaptation in zebrafish. *Nature* **485,** 471–477 (2012). doi: 10.1038/nature11057.
2. Panier, T. *et al.* Fast functional imaging of multiple brain regions in intact zebrafish larvae using Selective Plane Illumination Microscopy. *Frontiers in Neural Circuits* **7** (2013). doi: 10.3389/fncir.2013.00065.
3. Ahrens, M. B., Orger, M. B., Robson, D. N., Li, J. M. & Keller, P. J. Whole-brain functional imaging at cellular resolution using light-sheet microscopy. *Nat Methods* **10,** 413–420 (2013).
4. Portugues, R., Feierstein, C. E., Engert, F. & Orger, M. B. Whole-Brain Activity Maps Reveal Stereotyped, Distributed Networks for Visuomotor Behavior. *Neuron* **81,** 1328–1343 (2015). doi: 10.1016/j.neuron.2014.01.019.
5. Bianco, I. H., Kampff, A. R. & Engert, F. Prey capture behavior evoked by simple visual stimuli in larval zebrafish. *Front Syst Neurosci* **5,** 101 (2011).
6. Paris, C. B. *et al.* Reef Odor: A Wake Up Call for Navigation in Reef Fish Larvae. *PLoS ONE* **8,** e72808 (2013).
7. Egan, R. J. *et al.* Understanding behavioral and physiological phenotypes of stress and anxiety in zebrafish. *Behavioural Brain Research* **205,** 38–44 (2009).
8. Finger, T. E. Feeding patterns and brain evolution in ostariophysean fishes. *Acta Physiol Scand Suppl* **638,** 59–66 (1997).
9. Finger, T. E. Sorting food from stones: the vagal taste system in Goldfish, Carassius auratus. *J. Comp. Physiol. A Neuroethol. Sens. Neural. Behav. Physiol.* **194,** 135–143 (2008).
10. Vergassola, M., Villermaux, E. & Shraiman, B. I. 'Infotaxis' as a strategy for searching without gradients. *Nature* **445,** 406–409 (2007).
11. Ishimaru, Y. *et al.* Two families of candidate taste receptors in fishes. *Mechanisms of Development* **122,** 1310–1321 (2005).

12. Aihara, Y. *et al.* Transgenic labeling of taste receptor cells in model fish under the control of the 5'-upstream region of medaka phospholipase C-beta 2 gene. *Gene Expression Patterns* **7,** 149–157 (2007).
13. Hansen, A., Reutter, K. & Zeiske, E. Taste bud development in the zebrafish, Danio rerio. *Developmental Dynamics* **223,** 483–496 (2002).
14. Evans, D. H., Claiborne, J. B. & Currie, S. The Physiology of Fishes. CRC Marine Biology Series (CRC Press, 2013), fourth edition edn.
15. Wullimann, M. F. & Mueller, T. Teleostean and mammalian forebrains contrasted: Evidence from genes to behavior. *The Journal of Comparative Neurology* **475,** 143–162 (2004).
16. Blumhagen, F. *et al.* Neuronal filtering of multiplexed odour representations. *Nature* **479,** 493–498 (2011). doi: 10.1038/nature10633.
17. Rohde, C. B., Zeng, F., Gonzalez-Rubio, R., Angel, M. & Yanik, M. F. Microfluidic system for on-chip high-throughput whole-animal sorting and screening at subcellular resolution. *Proceedings of the National Academy of Sciences* **104,** 13891–13895 (2007).
18. Lin, X. *et al.* High-throughput mapping of brain-wide activity in awake and drug-responsive vertebrates. *Lab Chip* **15,** 680–689 (2015). doi: 10.1038/nature11057.
19. Chronis, N., Zimmer, M. & Bargmann, C. Microfluidics for *in vivo* imaging of neuronal and behavioral activity in Caenorhabditis elegans. *Nature methods* **4,** 727–731 (2007).
20. Albrecht, D. R. & Bargmann, C. I. High-content behavioral analysis of Caenorhabditis elegans in precise spatiotemporal chemical environments. *Nat Meth* **8,** 599–605 (2011). doi: 10.1038/nmeth.1630.
21. Brown, L., Koerner, T., Horton, J. H. & Oleschuk, R. D. Fabrication and characterization of poly(methylmethacrylate) microfluidic devices bonded using surface modifications and solvents. *Lab Chip* **6,** 66–73 (2006).
22. McElligott, M. & O'Malley, D. Prey Tracking by Larval Zebrafish: Axial Kinematics and Visual Control. *Brain, Behavior and Evolution* **66,** 177–196 (2005).
23. Burgess, H. A. & Granato, M. Modulation of locomotor activity in larval zebrafish during light adaptation. *Journal of Experimental Biology* **210,** 2526–2539 (2007).
24. Dombeck, D. A., Khabbaz, A. N., Collman, F., Adelman, T. L. & Tank, D. W. Imaging large-scale neural activity with cellular resolution in awake, mobile mice. *Neuron* **56,** 43–57 (2007).

Acknowledgements

We thank HC Park (Kyungpook National University, Korea) for the HuC promoter, L. Looger (Howard Hughes Medical Institute, Ashburn, Virginia, USA) for GCaMP3 and K. Kawakami (National Institute of Genetics, Shizuoka, Japan) for pT2KXIGin vector. We thank N. Garroum for helpfull assistance in simulating the flows in the microfluidic device during chip design, V. Perez-Schuster for help with the data analysis of two-photon calcium imaging, T. Pietri for helpful discussions, and M. Kapsimali for assistance in neuroanatomy of the zebrafish gustatory system. The post-doc work of M.S.M. was supported by *Neuropôle de recherche francilien* (NeRF) and INSERM. One year of post-doc work of R.C. was supported by the *Fondation Pierre-Gilles de Gennes pour la recherche*. G.S. was funded by the ERC starting grant 243106. ANR-10-LABX-54 MEMO LIFE, ANR- 11-IDEX-0001-02 PSL* Research University.

Author Contributions

R.C. designed the microfluidic chip, characterized the flows, analyzed the neuronal and behavioral data and contributed to manuscript writing. M.S.M. performed functional imaging and behavioral experiments, analyzed neuronal and behavioral data and contributed to manuscript writing. S.A.R. wrote the neuron detection and signal extraction programs. A.J. wrote the tail tracking program. G.D. and G.S. designed the project and contributed to manuscript writing.

Additional Information

Supplementary information accompanies this paper at http://www.nature.com/srep

Competing financial interests: The authors declare no competing financial interests.

How to cite this article: Candelier, R. *et al.* A microfluidic device to study neuronal and motor responses to acute chemical stimuli in zebrafish. *Sci. Rep.* **5**, 12196; doi: 10.1038/srep12196 (2015).

Visual stimulation

After having developed our 2-photon light sheet microscope, we got interested in the neural circuits implied in a fundamental visually-driven behavvior: phototaxis. With Sébastien Wolf and Sophia Karpenko, we have combined results from behavioral "virtual reality" assays, 2-photon light sheet microscopy under visual stimulation, optogenetics and network modelization to study how the brain coordinates visual exploration and motion to efficiently orient the animal towards ligh sources.

This work approaches numerous fundamental aspects of neuroscience: goal-driven locomotion, active sensing, central pattern generators and motor memory. This is, to my knowledge, the first study that shows that light sheet microscopy – besides the technological challenge – can be used to reveal biologocial phenomenons otherwise unaccessible. In contrast with classical approaches in which sparse recordings in pre-defined regions where used to infer the function of large-scale networks, this work uses a new paradigm in which we started from the function itself. On the basis of behavioral results we have searched for the neurons fitting a certain set of constraints: being correlated to gaze orientation, self-oscillate even without visual saccades and finally respond to lateralized stimuli. Once this set of neurons has been well-characterized in functional imaging, we have been able to derive a functional model. This top-down approach is relatively rare in neuroscience, but I believe it has the potential to be a new reference paradigm.

Key to the "taxis" processes is a self-oscillating network which constitutes a sensorimotor hub. Like a metronome with a $\approx 10\,s$period, it coordinates the occular saccades and the orientation of successive swim bouts. It also integrates visual stimuli (and probably stimuli from other sensory modalities) in a state-dependant manner, and we have developed a minimalist dynamical model that reproduces the sensori-motor bias towards ligh sources.

This article is still under review at the time of this writing and cannot be inserted in this manuscript. Key results will be presented during the oral defense.

Chapter 5

Research projects

Contents

My scientifical projects at short and mid-term are twofold: I wish to develop an "ultimate microscope" for zebrafish neuroscience and to focus my work on the neural processes underlying chemotaxis.

The ultimate microscope

During the last four years, I haveb been able to measure the high potential of light sheet microscopy for functional imaging. However, there are still several issues to resolve before one can take full advantage of the technique.

First of all, temporal resolution is an issue. Though in constant progress, current genetically encoded calcium reporters only reveal a limited quantity of information: single spikes are indiscernible from noise and spike trains appear as slow variations of fluorescence, such that one cannot separate the spikes and have access, for instance to relevant quantities like the spike rate. A possible workaround would be to combine light sheet microscopy with electrophysiological recordings. This would allow to (*i*) precisely calibrate the fluorescence signals with respect to real spikes trains in zebrafish larvae and (*ii*) have an excellent temporal resolution on a few neurons of interest while performing brain-wide recordings.

Then, the amount of data is massive: recordings typically generate a hundred GigaBytes per ten minutes of acquisition. Each experimental project gathers data from hundreds of runs, *i.e.* several tens of TeraBytes that one has to stock, backup and analyze. Today a theoretical and practical

effort is necessary to develop fast and robust algorithms that could process the images on the fly. Ideally, this live analysis should provide a detailed description of the architecture of neural networks responding to a given stimulation. Another main asset of performing data analysis on a timescale short enough to let the sample mounted in the microscope is to be able to target neural population of interest on a functional basis. This could greatly improve the efficiency of electrophysiological recordings, photo-ablation and optogenetics experiments. In addition, this would ease the comparison and merging of recordings over different individuals, or responses to different stimuli of the same sample.

Also, optogenetical tools are particularly useful to trigger neural activity in networks that would be otherwise difficult to stimulate in a controlled manner (*e.g.* hydromechanical perception *via* the lateral line). One can excite directly the sensory cells or their primary projections and get rid of the physical constraints of real-world stimulations, like for instance what is done in [34] for chemoreception.

This approach, altogether with the SPIM / electrophysiology combination, requires to perform data analysis over the networks of interest in quasi real-time. This is why I wish to develop a modular setup gathering all the currently accessible tools: (*i*) light sheets, in both visible and 2-photon versions, (*ii*) electrophysiology, (*iii*) photo-ablation, (*iv*) optogenetics, (*v*) stimulation devices and finally (*vi*) behavioral recordings. The cement to combine these different techniques altogether will be a software layer performing live analyses.

This ultimate setup will provide multiple simultaneous information and will be a unique playground with protocols limited by our sole imagination. This will be a strong asset for the LJP, and I see this modular setup as a powerful research catalyst. I am the leading BRAINTEGRATION project, which gathers a consortium of 5 research teams in Paris; we obtained in 2016 a 168 k€ grant from the Île de France region (*DIM Cerveau et Pensée*) to by some of the equipment required by this project.

Chemotaxis

The ability to locate a chemical source, called *chemotaxis*, represents one of the most fundamental navigational task that any motile organism must execute to survive (*e.g.* finding food) or reproduce (finding mates). This goal-driven behaviour takes various forms: bacteria, such as E. Coli [35], and the nematode C. Elegans [36] are able to chemotax in concentration gradients with biased random walks, while animals with a more elaborate nervous sys-

tem (*e.g.* mosquitos [37], zebrafish [34], blue crabs [38], moths [39], dogs [40] and humans [41]) use a different class of scent-tracking strategies allowing them to successfully localize sources in environments as complex as long-range turbulent fluid flows. Today, a general model describing chemotaxis would be of great practical interest. It could inspire new strategies to fight against some infection vectors, like Anopheles mosquitos that spread malaria [42]. It would certainly be also beneficial for designing "sniffers" (*i.e.* robots / drones aimed at localizing drugs, explosives, chemical leaks or pollution sources), a domain for which biomimetic approaches have already proven to be successful [42, 43, 44].

From a more fundamental point of view, the high spatio-temporal fluctuations in turbulent flows impose severe constraints on the strategies that a searcher can adopt. In contrast with other forms of goal-driven locomotion (phototaxis, rheotaxis, etc.) where the probed field is relatively invariant, strategies relying on instantaneous spatial sampling would be here relatively inefficient. In practice, though stereo-olfaction is used by some species in mild flows [41, 45], the proximity of the two nostrils make it unpractical in noisy cases [46, 47]. *A contrario*, temporal buffering acts as a low-pass filter to efficiently reduce the salience of misleading cues and leads to a rich repertoire of strategies that can be expressed in terms of a tradeoff between phases of "exploration" (search, pseudo-random motion) and "exploitation" (decision, oriented motion) [48]. Such phasic strategies are ubiquitous in nature [37, 38, 39, 40, 41, 42, 45] and, at the neural scale, require a form of short-term memory. Overall, these peculiarities make macroscopic chemotaxis an ideal paradigm for studying the substrate of short-term memory during navigational tasks, a domain of importance as its impairments remain key puzzles in understanding the cognitive deficits in schizophrenia [49, 50] and autism [51].

This project aims at unraveling the neural mechanisms underlying navigational short-term memory in larval zebrafish. It innately possesses many assets for such a project as it searches for amino acids immediately after hatching [52], it develops complex food hunting behavior during its larval stage [53] and features habituation, sensitization, or conditioning [54] which are all representatives of non-declarative memory but also a memory similar to the declarative memory described for mammals [55].

My first goal is to model the larvae chemotactic strategy. I am developing behavioral assays to test the larvae preferences in mild flows and navigational strategies in turbulent flows. On the longer term I plan to reproduce chemotaxis on a partially-tethered animal in a lightsheet microscope, probably using a virtual reality system taking advantage of the high temporal accuracy of the microfluidic devices we have developped at the LJP.

This project would have been impossible a decade ago, as it requires the unique combination of multiple technologies in genetics, microfluidics and lightsheet functional microscopy. I believe that our group, which has gathered during the last few years a substantial experience in larval zebrafish behavior , microfluidics, virtual reality assays and lightsheet functional microscopy is uniquely suited to lead this multi-disciplinary project.

Complements

Research Curriculum Vitae

2012 - today	Research scientist (*Chargé de recherche* CNRS) at the Laboratoire Jean Perrin (CNRS 8237 - UPMC) *Functional imaging and behavior of larval zebrafish*
2011 - 2012	Post-doc *Calciulm imaging and development of microfluidic devices for larval zebrafish*, with Georges Debrégeas at the LJP (ENS Paris)
2009 - 2011	Post-doc *A biomimetic approach of tactile perception*, with Georges Debrégeas and Alexis Prevost at the LJP (ENS Paris)
2006 - 2009	Ph.D. *Dynamics and structure close to the Glass and Jamming transitions; experiments and simulations*, under the supervision of Olivier Dauchot at the SPEC (CEA Saclay), in tight collaboration with Giulio Biroli (IPhT, CEA Saclay) UPMC Ph.D. Diploma obtained November 9^{th}, 2009
2005 - 2006	Pre-doctoral internship *A Field study of the collective behavior of starlings*, in the framework of the European project STARFLAG in the group of Giorgio Parisi (La Sapienza University, Rome)
2001 - 2004	ESPCI ParisTech, major in physics Engineer cursus including : 2004 - Master of Cognitive Science of the ENS-EHESS, with a 6 months internship at the DEC (ENS - Paris) on *Subliminal sound perception in humans* 2003 - 6 months inership at the Intelligent Mechanism Laboratory (Doshisha University - Kyoto) on *The precedence effect applied to virtual sounds in humans*

Publications, conference proceedings, seminars and prizes

Publications in peer-reviewed journals

2016

1. *A sensorimotor hub driving phototaxis in zebrafish*, Sébastien Wolf, Alexis Dubreuil, Tommaso Bertoni, Urs Lucas Böhm, Volker Bormuth, Raphaël Candelier, Sophia Karpenko, Rémi Monasson & Georges Debrégeas,
Under review at Nature Communication.

2. *A 2D virtual reality system for visual goal-driven navigation in zebrafish larvae*, Adrien Jouary, Mathieu Haudrechy, Raphaël Candelier & Germán Sumbre,
Scientific Reports **6**:34015 (2016), doi:10.1038/srep34015

3. *Rheotaxis of larval zebrafish: Behavioral study of a multi-sensory process*, Raphaël Olive, Sébastien Wolf, Alexis Dubreuil, Volker Bormuth, Georges Debrégeas & Raphaël Candelier,
Frontiers in systems neuroscience **10**:14 (2016), doi:10.3389/fnsys.2016.00014

2015

4. *A microfluidic device to study neuronal and motor responses to acute chemical stimuli in zebrafish*, Raphaël Candelier, Meena Sriti Murmu, Sebastián Alejo Romano, Adrien Jouary, Georges Debrégeas & Germán Sumbre,
Scientific reports **5**:12196 (2015), doi:10.1038/srep12196

5. *Whole-brain functional imaging with two-photon light-sheet microscopy*, Sébastien Wolf, Willy Supatto, Georges Debrégeas, Pierre Mahou, Sergei G Kruglik, Jean-Marc Sintes, Emmanuel Beaurepaire & Raphaël Candelier,
Nature Methods **12**:379-380 (2015), doi:10.1038/nmeth.3371

2013

6. *Fast functional imaging of multiple brain regions in intact zebrafish larvae using Selective Plane Illumination Microscopy*, Raphaël Candelier, Thomas Panier, Sebastián Romano, Raphaël Olive, Thomas Pietri, Germán Sumbre & Georges Debrégeas,
Frontiers in Neural Circuits **7**:65 (2013), doi:10.3389/fncir.2013.00065

2011

7. *Texture-induced modulations of friction force: the fingerprint effect*, Elie Wandersman, Raphaël Candelier, Georges Debrégeas & Alexis Prevost,

Physical Review Letters **107**:16, 164301 (2011), doi:10.1103/PhysRevLett.107.164301
NB : Cet article a fait l'objet d'un « News and Views » dans la revue Nature (480, 189-190, 8 décembre 2011 – doi:10.1038/480189a)

8. *The Role of Exploratory Conditions in Biomimetic Tactile Sensing*, Raphaël Candelier, Alexis Prevost & Georges Debrégeas,
Sensors **11**:8, 7934-7953(2011), doi:10.3390/s110807934

2010

9. *Dynamical facilitation decreases when approaching the granular glass transition*, Raphaël Candelier, Olivier Dauchot & Giulio Biroli,
Europhysics Letters **92**:24003 (2010), doi:10.1209/0295-5075/92/24003

10. *Spatiotemporal Hierarchy of Relaxation Events, Dynamical Heterogeneities, and Structural Reorganization in a Supercooled Liquid*, Raphaël Candelier, Asaph Widmer-Cooper, Olivier Dauchot, Giulio Biroli, David Reichman & Peter Harrowell,
Physical Review Letters **105**:135702 (2010), doi:10.1103/PhysRevLett.105.135702

11. *Super-Diffusion around the Rigidity Transition: Levy and the Lilliputians*, Frédéric Lechenault, Raphaël Candelier, Olivier Dauchot, Jean-Philippe Bouchaud & Giulio Biroli,
Soft Matter **6**:3059-3064 (2010), doi:10.1039/C000802H
NB : This article was selected to be on the front cover of the Soft Matter issue.

12. *Journey of an intruder through the fluidization and jamming transitions of a dense granular media*, Raphaël Candelier & O. Dauchot,
Physical Review E **81**:011304 (2010), doi:10.1103/PhysRevE.81.011304

2009

13. *Creep Motion of an Intruder within a Granular Glass close to Jamming*, Raphaël Candelier & O. Dauchot,
Physical Review Letters **103**:128001 (2009), doi:10.1103/PhysRevLett.103.128001

14. *The Building Blocks of Dynamical Heterogeneities in Dense Granular Media*, Raphaël Candelier, Olivier Dauchot & Giulio Biroli,
Physical Review Letters **102**:088001 (2009), doi:10.1103/PhysRevLett.102.088001

2008

15. *Empirical investigation of starling flocks: a benchmark study in collective animal behaviour*, Michele Ballerini, Nicola Cabibbo, Raphaël Candelier, Andrea Cavagna, Evaristo Cisbani, Irene Giardina, Alberto Orlandi, Giorgio Parisi, Andrea Procaccini, Massimiliano Viale & Vladimir Zdravkovic,
Animal Behaviour **76**:201-215 (2008), doi:10.1016/j.anbehav.2008.02.004

16. *Interaction Ruling Animal Collective Behaviour Depends on Topological rather than Metric Distance: Evidence from a Field Study*, Michele Ballerini, Nicola Cabibbo, Raphaël Candelier, Andrea Cavagna, Evaristo Cisbani, Irene Giardina, Vivien Lecomte, Alberto Orlandi, Giorgio Parisi, Andrea Procaccini, Massimiliano Viale & Vladimir Zdravkovic,
Proc. Nat. Acad. Sci. **105**:4, 1232-1237 (2008), doi:10.1073/pnas.0711437105

Conference proceedings

1. *The glass and jamming transitions in dense granular matter*, Corentin Coulais, Raphaël Candelier & Olivier Dauchot,
POWDERS AND GRAINS 2013: Proceedings of the 7th International Conference on Micromechanics of Granular Media **1542**:1 25-31 (2013), doi:10.1063/1.4811862

2. *Evolution of dynamical facilitation approaching the glass transition*, Raphael Candelier, Asaph Widmer-Cooper, David Reichman, Giulio Biroli & Olivier Dauchot,
APS Meeting **1**:30011 (2013), 2013APS..MARU30011C

Invited talks at conferences

Single Plane Illumination Microscopy for imaging neuronal activity, First day Lyon Bio-Image, 22 novembre 2013

Seminars and communications

2016
— *Zebrafish and Chips*, IPGG Microfluidics Seminar
— *The functional circuit driving positive phototaxis*, Probing neural networks with light: imaging structure and function in the living brain, Cold Spring Harbor Asia, Suzhou, China
— *SYMiBio Workshop*, Institut Pierre-Gilles de Gennes, Paris, France
2015
— *Single Plane Illumination Microscopy SPIM for imaging neuronal activity*, Theoretical Neuroscience Group, École Normale Supérieure, Paris, France
— *Wholebrain Functional Imaging with Twophoton Lightsheet Microscopy*, 9^{th} European Zebrafish Meeting, Oslo, Norway
— *Wholebrain Functional Imaging with Twophoton Lightsheet Microscopy*, 2^{nd} Light Sheet Fluorescence Microscopy International conference & 7^{th} International LSFM workshop, Genoa, Italy

2013

— *A microfluidics toolkit to deliver precise chemical stimuli to zebrafish larvae*, 8th European Zebrafish Meeting, Barcelona, Spain
— *A microfluidics toolkit to deliver precise chemical stimuli to zebrafish larvae*, Engert lab, Harvard University, USA
— *A taste of zebrafish: preliminary results and ongoing projects*, Laboratoire Jean Perrin, UPMC, France
— *Evolution of dynamical facilitation approaching the glass transition*, APS March Meeting, Baltimore, USA

Non-scientifical prizes

1. First-rank winner fo the Matlab contest 2012, an international collaborative programming contest with more than 3000 participants worldwide.

2. Winner of the Mappy challenge 2010, a programming contest on geolocalisation implying 28 French teams (10k€prize).

Reviews for scientifical journals

I reviewed articles for Physical Review Letters (7 articles) and Nature Communications (1 article).

Technological transfert and valorization

I participate as a scientifical and technical consultant to the *Superdyne* project held by Jérémie Laurent, a graduate student doing his thesis at University Paris VII. This project aims at design injection systems to improve the cell viability during injection protocols by reducing the shear stress in the flows at the level of the syringe tip. The first prototypes have shown some increase in the survival rate of the injected cells from approximately 15% with classical synringes up to 95% with the *Superdyne* system, and also reducing the variability. Jérémie is in the process of improving the design and envisions to publish an article soon and to start a small company in the mid-term.

Teaching and student supervision

Teaching

The Laboratoire Jean Perrin has set up a pilot experiment at the UPMC with the ABER contracts: the idea is to pair a *Maître de conférence* with a *Chargé de recherche* of the same laboratory, the latter making from 20 to 32 teaching hours. I participated to this by taking in charge 32 hours of the teaching load of Elie Wandersman in 2013-2014 and 2014-2015 (UE : MP121, level M1, Phytem course). In 2015-2016, I have led a "research workshop" of 32 hours at the FabLab of Sorbonne Université.

I also taught during my Ph.D. in the framework of the *monitorat* system at the UPMC (64 hours/year). For the first year I had tutorial classes in mathematics for the first year of licence. The following years I was in charge of practical work classes in Physics for the first year of licence. I also did mini-tutorials classes (1 hour with 3 students) for 3 hours a week at the *Institut Supérieur d'Électronique de Paris* from 2003 to 2008.

Student supervision

I have co-supervised the Ph.D. of Raphaël Olive and I am currently co-supervising the Ph.D. of Sébastien Wolf. I have also supervised many interns in Licence and Master courses since 2007:

2013-2017	Co-supervision of Sébastien Wolf's Ph.D.
2017	Milena Corcos, Licence 3
2016	Cuong Pham, Master 1
2012-2015	Co-supervision of Raphaël Olive's Ph.D.
2013	Sarah Hazgui, Licence 3
2013	Mathilde Allio, Licence 3
2012-2013	Sébastien Wolf, Master 2
2011-2012	Raphaël Olive, Master 2
2008-2009	Corentin Coulais, Master 2
2008-2009	Beaudouin Saint-Yves, Master 2
2007-2008	François Paradis, Master 2
2007-2008	Ahmed Khelladi, Master 2

Bibliography

[1] Raphaël Candelier. *Dynamics and structure close to the glass and Jamming transitions : experiments and simulations*. PhD thesis, 2009. Thèse de doctorat dirigée par Dauchot, Olivier Physique Paris 6 2009.

[2] Ahrens Misha B, Orger Michael B, Robson Drew N, Li Jennifer M, and Keller Philipp J. Whole-brain functional imaging at cellular resolution using light-sheet microscopy. *Nat Meth*, 10(5):413–420, may 2013.

[3] K. Hinsch and G.K.H. Zupanc. Generation and long-term persistence of new neurons in the adult zebrafish brain: A quantitative analysis. *Neuroscience*, 146(2):679–696, 2007.

[4] Sabine L. Renninger and Michael B. Orger. Two-photon imaging of neural population activity in zebrafish. *Methods*, 62(3):255–267, 2013. Zebrafish Methods.

[5] Christine Grienberger and Arthur Konnerth. Imaging Calcium in Neurons. *Neuron*, 73(5):862–885, 2012.

[6] Ahrens Misha B., Li Jennifer M., Orger Michael B., Robson Drew N., Schier Alexander F., Engert Florian, and Portugues Ruben. Brain-wide neuronal dynamics during motor adaptation in zebrafish. *Nature*, 485(7399):471–477, may 2012. 10.1038/nature11057.

[7] Julia L Semmelhack, Joseph C Donovan, Tod R Thiele, Enrico Kuehn, Eva Laurell, and Herwig Baier. A dedicated visual pathway for prey detection in larval zebrafish. *eLife*, 3:e04878, dec 2014.

[8] Fumi Kubo, Bastian Hablitzel, Marco Dal Maschio, Wolfgang Driever, Herwig Baier, and Aristides B. Arrenberg. Functional Architecture of an Optic Flow-Responsive Area that Drives Horizontal Eye Movements in Zebrafish. *Neuron*, 81(6):1344–1359, 2014.

[9] Thomas Panier, Sebastian Romano, Raphaël Olive, Thomas Pietri, German Sumbre, Raphaël Candelier, and Georges Debrégeas. Fast functional imaging of multiple brain regions in intact zebrafish larvae using Selective Plane Illumination Microscopy. *Frontiers in Neural Circuits*, 7:65, 2013.

[10] Raphaël Olive. *Perception des écoulements et des vibrations chez la larve de poisson-zèbre : étude comportementale et imagerie*. PhD thesis, 2015. Thèse de doctorat dirigée par Candelier, Raphaël et Debrégeas, Georges Physique Paris 6 2015.

[11] Alexandre Pouget, Jeffrey M Beck, Wei Ji Ma, and Peter E Latham. Probabilistic brains: knowns and unknowns. *Nature neuroscience*, 16(9):1170–1178, 2013.

[12] Shimon Edelman. The minority report: some common assumptions to reconsider in the modelling of the brain and behaviour. *Journal of Experimental & Theoretical Artificial Intelligence*, 28(4):751–776, 2016.

[13] Ofstad Tyler A., Zuker Charles S., and Reiser Michael B. Visual place learning in Drosophila melanogaster. *Nature*, 474(7350):204–207, jun 2011. 10.1038/nature10131.

[14] Mischiati Matteo, Lin Huai-Ti, Herold Paul, Imler Elliot, Olberg Robert, and Leonardo Anthony. Internal models direct dragonfly interception steering. *Nature*, 517(7534):333–338, jan 2015.

[15] Adrien Jouary. *Comportement moteur induit visuellement et spontané chez la larve du poisson zèbre*. PhD thesis, 2015. Thèse de doctorat dirigée par Sumbre, German Neurosciences Paris 6 2015.

[16] Chintan Trivedi and Johann Bollmann. Visually driven chaining of elementary swim patterns into a goal-directed motor sequence: a virtual reality study of zebrafish prey capture. *Frontiers in Neural Circuits*, 7:86, 2013.

[17] Raphaël Olive, Sébastien Wolf, Alexis Dubreuil, Volker Bormuth, Georges Debrégeas, and Raphaël Candelier. Rheotaxis of Larval Zebrafish: Behavioral Study of a Multi-Sensory Process. *Frontiers in Systems Neuroscience*, 10:14, 2016.

[18] Werner Göbel and Fritjof Helmchen. In Vivo Calcium Imaging of Neural Network Function. *Physiology*, 22(6):358–365, 2007.

[19] Benjamin F Grewe, Dominik Langer, Hansjörg Kasper, Björn M Kampa, and Fritjof Helmchen. High-speed in vivo calcium imaging reveals neuronal network activity with near-millisecond precision. *Nature methods*, 7(5):399–405, 2010.

[20] Junichi Nakai, Masamichi Ohkura, and Keiji Imoto. A high signal-to-noise Ca2+ probe composed of a single green fluorescent protein. *Nature biotechnology*, 19(2):137–141, 2001.

[21] Jasper Akerboom, Nicole Carreras Calderón, Lin Tian, Sebastian Wabnig, Matthias Prigge, Johan Tolö, Andrew Gordus, Michael B Orger, Kristen E Severi, John J Macklin, et al. Genetically encoded calcium indicators for multi-color neural activity imaging and combination with optogenetics. *Frontiers in molecular neuroscience*, 6:2, 2013.

[22] José-Angel Conchello and Jeff W Lichtman. Optical sectioning microscopy. *Nature methods*, 2(12):920–931, 2005.

[23] Winfried Denk, James H Strickler, Watt W Webb, et al. Two-photon laser scanning fluorescence microscopy. *Science*, 248(4951):73–76, 1990.

[24] Jason ND Kerr and Winfried Denk. Imaging in vivo: watching the brain in action. *Nature Reviews Neuroscience*, 9(3):195–205, 2008.

[25] Jörg Bewersdorf, Rainer Pick, and Stefan W Hell. Multifocal multiphoton microscopy. *Optics letters*, 23(9):655–657, 1998.

[26] R Salome, Y Kremer, S Dieudonne, J-F Léger, O Krichevsky, C Wyart, D Chatenay, and L Bourdieu. Ultrafast random-access scanning in two-photon microscopy using acousto-optic deflectors. *Journal of neuroscience methods*, 154(1):161–174, 2006.

[27] Jan Huisken, Jim Swoger, Filippo Del Bene, Joachim Wittbrodt, and Ernst HK Stelzer. Optical sectioning deep inside live embryos by selective plane illumination microscopy. *Science*, 305(5686):1007–1009, 2004.

[28] Philipp J Keller, Annette D Schmidt, Joachim Wittbrodt, and Ernst HK Stelzer. Reconstruction of zebrafish early embryonic development by scanned light sheet microscopy. *science*, 322(5904):1065–1069, 2008.

[29] Terrence F Holekamp, Diwakar Turaga, and Timothy E Holy. Fast three-dimensional fluorescence imaging of activity in neural populations by objective-coupled planar illumination microscopy. *Neuron*, 57(5):661–672, 2008.

[30] Michael L. Risner, Elizabeth Lemerise, Eric V. Vukmanic, and Ashley Moore. Behavioral spectral sensitivity of the zebrafish (Danio rerio). *Vision Research*, 46(17):2625–2635, 2006.

[31] Fernandes António M, Fero Kandice, Driever Wolfgang, and Burgess Harold A. Enlightening the brain: Linking deep brain photoreception with behavior and physiology. *BioEssays : news and reviews in molecular, cellular and developmental biology*, 35(9):775–779, may 2013.

[32] Nikita Vladimirov, Yu Mu, Takashi Kawashima, Davis V Bennett, Chao-Tsung Yang, Loren L Looger, Philipp J Keller, Jeremy Freeman, and Misha B Ahrens. Light-sheet functional imaging in fictively behaving zebrafish. *Nature methods*, 2014.

[33] Raphaël Candelier, Meena Sriti Murmu, Sebastián Alejo Romano, Adrien Jouary, Georges Debrégeas, and Germán Sumbre. A microfluidic device to study neuronal and motor responses to acute chemical stimuli in zebrafish. *Scientific reports*, 5, 2015.

[34] Tetsuya Koide, Nobuhiko Miyasaka, Kozo Morimoto, Kazuhide Asakawa, Akihiro Urasaki, Koichi Kawakami, and Yoshihiro Yoshihara. Olfactory neural circuitry for attraction to amino acids revealed by transposon-mediated gene trap approach in zebrafish. *Proceedings of the National Academy of Sciences*, 106(24):9884–9889, 2009.

[35] Howard C. Berg. Motile Behavior of Bacteria. *Physics Today*, 53(1), 2000.

[36] Jonathan T Pierce-Shimomura, Thomas M Morse, and Shawn R Lockery. The fundamental role of pirouettes in Caenorhabditis elegans chemotaxis. *The journal of neuroscience*, 19(21):9557–9569, 1999.

[37] Moment-to-moment flight manoeuvres of the female yellow fever mosquito (Aedes aegypti L.) in response to plumes of carbon dioxide and human skin odour.

[38] Marc J Weissburg and David B Dusenbery. Behavioral observations and computer simulations of blue crab movement to a chemical source in a controlled turbulent flow. *Journal of Experimental Biology*, 205(21):3387–3398, 2002.

[39] Agenor Mafra-Neto, Ring T Cardé, et al. Fine-scale structure of pheromone plumes modulates upwind orientation of flying moths. *Nature*, 369(6476):142–144, 1994.

[40] Aud Thesen, Johan B Steen, and KB Doving. Behaviour of dogs during olfactory tracking. *Journal of Experimental Biology*, 180(1):247–251, 1993.

[41] Jess Porter, Brent Craven, Rehan M Khan, Shao-Ju Chang, Irene Kang, Benjamin Judkewitz, Jason Volpe, Gary Settles, and Noam Sobel. Mechanisms of scent-tracking in humans. *Nature neuroscience*, 10(1):27–29, 2007.

[42] Bree Cummins, Ricardo Cortez, Ivo M Foppa, Justin Walbeck, and James M Hyman. A spatial model of mosquito host-seeking behavior. *PLoS Comput Biol*, 8(5):e1002500, 2012.

[43] Tim Pearce, Kwok Chong, Paul Verschure, Sergi Bermudez i Badia, Eric Chanie, Mikael Carlsson, and Bill Hansson. Chemotactic search in complex environments. In *Electronic noses & sensors for the detection of explosives*, pages 181–207. Springer, 2004.

[44] DR Webster, KY Volyanskyy, and MJ Weissburg. Bioinspired algorithm for autonomous sensor-driven guidance in turbulent chemical plumes. *Bioinspiration & biomimetics*, 7(3):036023, 2012.

[45] Raghav Rajan, James P Clement, and Upinder S Bhalla. Rats smell in stereo. *Science*, 311(5761):666–670, 2006.

[46] David G Moulton. Olfaction in mammals. *American zoologist*, 7(3):421–429, 1967.

[47] Alex Gomez-Marin, Greg J Stephens, and Matthieu Louis. Active sampling and decision making in Drosophila chemotaxis. *Nature communications*, 2:441, 2011.

[48] Massimo Vergassola, Emmanuel Villermaux, and Boris I Shraiman. 'Infotaxis' as a strategy for searching without gradients. *Nature*, 445(7126):406–409, 2007.

[49] Jared X Van Snellenberg, Ragy R Girgis, Guillermo Horga, Elsmarieke van de Giessen, Mark Slifstein, Najate Ojeil, Jodi J Weinstein, Holly Moore, Jeffrey A Lieberman, Daphna Shohamy, et al. Mechanisms of Working Memory Impairment in Schizophrenia. *Biological psychiatry*, 2016.

[50] Jakob Siemerkus, Eva Irle, Carsten Schmidt-Samoa, Peter Dechent, and Godehard Weniger. Egocentric spatial learning in schizophrenia investigated with functional magnetic resonance imaging. *NeuroImage: Clinical*, 1(1):153–163, 2012.

[51] Sophie E Lind, David M Williams, Jacob Raber, Anna Peel, and Dermot M Bowler. Spatial navigation impairments among intellectually high-functioning adults with autism spectrum disorder: exploring relations with theory of mind, episodic memory, and episodic future thinking. *Journal of abnormal psychology*, 122(4):1189, 2013.

[52] Sara M Lindsay and Richard G Vogt. Behavioral responses of newly hatched zebrafish (Danio rerio) to amino acid chemostimulants. *Chemical senses*, 29(2):93–100, 2004.

[53] Isaac Henry Bianco, Adam R Kampff, and Florian Engert. Prey capture behavior evoked by simple visual stimuli in larval zebrafish. *Frontiers in systems neuroscience*, 5:101, 2011.

[54] Adam C Roberts, Brent R Bill, and David L Glanzman. Learning and memory in zebrafish larvae. 2013.

[55] Madelene Åberg Andersson, Fredrik Ek, and Roger Olsson. Using visual lateralization to model learning and memory in zebrafish larvae. *Scientific reports*, 5, 2015.